A Numerical Study of the Limiting Cases of Cylinder-Induced Shock Wave/Boundary Layer Interactions

A Thesis Presented for the

Master of Science

Degree

The University of Tennessee, Knoxville

Stefen Albert Lindorfer

May 2017

Copyright © 2017 by Stefen Albert Lindorfer
All rights reserved.

ACKNOWLEDGEMENTS

First and foremost, I would like to express my gratitude towards Dr. John D. Schmisseur, my advisor and mentor, for guiding me in my professional development, for being so understanding, and for allowing me to become his first graduate. Thank you to my parents, Dr. med. Hans W. Lindörfer and Maria D. Dellaplain, as well as my step-father, James L. Guy, for supporting me throughout this endeavor. Their continued support allowed me to push on and focus on my research while they accommodated many hassles in my life. A thank you to Dr. James G. Coder, Dr. Kivanc Ekici, and Dr. Ryan S. Glasby for serving on my committee. I would like to acknowledge Dr. Ryan B. Bond and Dr. Ryan S. Glasby whose CFD knowledge has been very valuable to me. I would like to thank Dr. Christopher S. Combs, Dr. Phillip A. Kreth, and E. Lara Lash for their assistance on this project. Furthermore, Dr. Phillip A. Kreth has provided a great sense of both technical and moral support, and I want to thank him for helping me avoid tunnel vision.

ABSTRACT

One of the limiting factors in the design of supersonic and hypersonic vehicles remains the prediction and control of the high aerodynamic, thermodynamic, acoustic, and structural loads generated by a shock wave/boundary layer interaction (SWBLI or SBLI). In conjunction with an experimental campaign produced within the research group, a numerical study was performed using a semi-infinite cylinder to generate a SWBLI at Mach 1.88 with both laminar and turbulent boundary layers. The goals were not only to better understand the complex flow surrounding the cylinder-induced turbulent interaction, but also to establish the interaction bounds of the limiting cases of a transitional interaction.

Steady-state Reynolds-averaged Navier-Stokes (RANS) simulations were performed to predict the shock structures, separation and attachment points, and pressure profiles in the upstream region and on the cylinder leading edge. A variety of turbulence models were tested, namely the cubic k-epsilon (CKE), Menter's shear-stress transport (SST), and Spalart-Allmaras (SA) with quadratic constitutive relations (QCR). Both the CKE and SA-QCR turbulence models showed good agreement with in-house experimental data and literature, and are thus recommended for future use in these types of flow fields. Correlations between the vortex structures and peak and trough pressures were found, thus allowing for a steady-state flow characterization. The effect of varying the incoming boundary layer height was studied, when all other values were kept constant, and it was determined that an increased boundary layer height decreased both the interaction scale and the peak pressure.

TABLE OF CONTENTS

Chapter 1 Introduction 1
1.1 Motivation 1
1.2 Objectives of Current Work 3
Chapter 2 Literature Review 4
2.1 Cylinder-Induced Interaction Structure 4
2.2 Turbulent Cylinder-Induced Interaction 7
2.3 Laminar Cylinder-Induced Interaction 11
2.4 Transitional Cylinder-Induced Interaction Bounds 13
Chapter 3 Methodology 14
3.1 Flow Modeling Assumptions 14
3.2 Numerical Formulation 15
3.2.1 Governing Equations 15
3.2.2 Turbulence Model Set-Up 16
3.2.2.1 SST 16
3.2.2.2 SA-QCR 16
3.2.2.3 CKE 17
3.2.3 Time Integration Set-Up 17
3.2.4 Spatial Discretization Set-Up 17
3.2.5 Riemann Solver Set-Up 18
3.3 UTSI Experiments 18
3.4 Domain Definition and Mesh Generation 20
3.4.1 Flat Plate Flow 22
3.4.1.1 Initial Domain Size Reduction 22
3.4.1.2 Final Domain Size Reduction 23
3.4.1.3 2-D and 3-D Comparison 26
3.4.1.4 Inlet Profiles 28
3.4.2 Turbulent Interaction 29
3.4.3 Laminar Interaction 31
Chapter 4 Steady-State Results & Analysis 34

4.1 Turbulent Interaction 34
4.1.1 Cylinder with Height y/d = 4 35
4.1.1.1 Grid Independence Study 35
4.1.1.2 Turbulence Model Comparison 35
4.1.1.3 Surface Pressure Analysis 41
4.1.1.4 Effect of Incoming Boundary Layer Height 44
4.1.2 Cylinder with Height y/d = 10 51
4.1.2.1 Grid Independence Study 51
4.1.2.2 Turbulence Model Comparison 51
4.1.2.3 Surface Pressure Analysis 57
4.1.2.4 Effect of Incoming Boundary Layer Height 63
4.1.3 SWTBLI Topology Characterization with RANS 71
4.2 Laminar Interactions 72
4.2.1 Grid Independence Study 73
4.2.2 Comparison to Empirical Values 73
4.2.3 Surface Pressure Analysis 82
4.2.4 SWLBLI Topology Characterization with RANS 85
Chapter 5 Conclusions 88
List of References 91
Vita 97

LIST OF TABLES

Table 3.1. Flow conditions captured by experiments from Lash et al. [6] and Combs et al. [7] for wind tunnel and Combs et al. [7] for flat plate. 20

Table 3.2. Comparison between flat plate freestream conditions from CFD and PIV by Combs et al. [7] at $x/d = -19.5$, along with CFD data from $x/d = -5$. 29

Table 3.3. Characteristics of the turbulent interaction grid independence study with cylinders of height $y/d = 4$ and $y/d = 10$. 31

Table 3.4. Characteristics of the laminar interaction grid independence study. 33

Table 4.1. Comparison of parameters of interest between empirical values [11] and medium mesh results for all turbulence models with cylinder of height $y/d = 4$. 39

Table 4.2. Comparison of parameters of interest between empirical values [11] and fine mesh results for all turbulence models with cylinder of height $y/d = 10$. 56

Table 4.3. Comparison of parameters of interest between empirical values [11, 24] and extra fine mesh results for laminar interaction. 79

LIST OF FIGURES

Figure 2.1. Cylinder on a flat plate, indicating views of interest. Green plane in *x*-*y*, golden plane in *x*-*z*. 4

Figure 2.2. Front view schematic of a cylinder-induced shock wave/boundary layer interaction. 5

Figure 2.3. Top view schematic of a cylinder-induced shock wave/boundary layer interaction, indicating the surface interaction. 6

Figure 2.4. Sample a) Schlieren imaging and b) oil flow visualization for a turbulent interaction. Figure from Lash et al. [6]. 7

Figure 2.5. In-house experimental results indicating probability density function of separation length. Figure from Lash et al. [6]. 8

Figure 2.6. a) Blunt fin pressure ratio comparing computational results from Hung and Buning [16] with experimental results from Dolling and Bogdonoff [19] at M_∞ = 2.95, b) Streamlines of the computational results on the upstream centerline. Figures from Hung and Buning [16]. 10

Figure 2.7. Schematic of streamlines indicating vortex structure for a laminar interaction. Figure from Itoh and Mizoguchi [25]. 12

Figure 2.8. Kerosene lampblack flow visualization from top view of shock wave/ a) laminar, b) transitional, c) turbulent boundary layer interactions at M_∞ = 5. Flow from top to bottom. Figure from Murphree et al. [29]..... 13

Figure 3.1. Schematic of the cylinder located on the flat plate..... 19

Figure 3.2. 3-D domain of the first simulation using full width and height of the test section. This was used to test for sidewall influence and identify possible domain size reduction. 21

Figure 3.3. Medium 2-D flat plate domain with added forward section, reduced upper and lower flat plate surface extent, and reduced height..... 22

Figure 3.4. Medium 2-D flat plate mesh in *x*-*y*. Mesh domain zones are shown in grey, and shock-alignment is shown in green. 24

Figure 3.5. Close-up of leading edge section of the medium 2-D flat plate mesh. Mesh domain zones are shown in grey and shock-alignment is shown in green. 24

Figure 3.6. Smaller 2-D flat plate domain with reduced upper flat plate surface extent, and reduced height. 25
Figure 3.7. 3-D flat plate domain with cylinder, used to measure the extent of the interaction. 27
Figure 3.8. Base mesh of cylinder-interaction in *x*-*z*. Grey lines indicate domain zones, black lines show actual cells. 27
Figure 3.9. Base mesh for turbulent interactions in *x*-*z*. Grey lines indicate domain zones. 30
Figure 3.10. Base mesh for laminar interactions in *x*-*z*. Grey lines indicate domain zones. 32
Figure 4.1. a) Mach number and b) numerical Schlieren contours of medium mesh result with cylinder of height y/d = 4 with CKE turbulence model at z/d = 0. Black line in a) is sonic line. 36
Figure 4.2. Medium mesh results for cylinder of height y/d = 4. a) - c) Mach number contours for CKE, SST, and SA-QCR turbulence models, respectively, where pink line represents sonic line, black lines represent empirical values for B and h_{tp}. d) - f) Numerical Schlieren contours for CKE, SST, and SA-QCR turbulence models, respectively, where orange line represents sonic line, pink lines represent empirical values for B and h_{tp}. 37
Figure 4.3. Streamlines on medium mesh results for cylinder of height y/d = 4. a) - c) With and d) - f) without Mach number contours, for CKE, SST, and SA-QCR turbulence models, respectively. 40
Figure 4.4. Streamlines on zoomed-in corner region of medium mesh results for cylinder of height y/d = 4. a) - c) Mach number contours for CKE, SST, and SA-QCR turbulence models, respectively. 42
Figure 4.5. Medium mesh results with indicated turbulence models, showing normalized pressure on the flat plate surface, upstream of the cylinder with height y/d = 4. 43
Figure 4.6. Medium mesh results with varied incoming boundary layer height δ/d for cylinder with height y/d = 4. a) - j) δ/d = 0.25 to δ/d = 2.50 with constant increment of 0.25. Orange line represents sonic line. 46

Figure 4.7. Comparison of parameters of interest between empirical values [11] and medium mesh results for varied δ/d with cylinder of height y/d = 4. a) λ/d, b) B/d, c) h_{tp}/d. 47
Figure 4.8. Medium mesh results with varied δ/d, showing normalized pressure on the flat plate surface, upstream of the cylinder with height y/d = 4. 49
Figure 4.9. Medium mesh results with varied δ/d, showing normalized pressure on the cylinder leading edge of the cylinder with height y/d = 4..... 50
Figure 4.10. Grid independence study comparing the parameters of interest for various turbulence models with cylinder of height y/d = 10. a) λ/d, b) B/d, c) h_{tp}/d. 52
Figure 4.11. a) Mach number and b) numerical Schlieren contours of fine mesh result with cylinder of height y/d = 10 with SA-QCR turbulence model at z/d = 0. Black line in a) is sonic line. 54
Figure 4.12. Fine mesh results for cylinder of height y/d = 10. a) - c) Mach number contours for CKE, SST, and SA-QCR turbulence models, respectively, where pink line represents sonic line, black lines represent empirical values for B and h_{tp}. d) - f) Numerical Schlieren contours for CKE, SST, and SA-QCR turbulence models, respectively, where orange line represents sonic line, pink lines represent empirical values for B and h_{tp}..... 55
Figure 4.13. Streamlines on fine mesh results for cylinder of height y/d = 10. a) - c) With d) - f) and without Mach number contours, for CKE, SST, and SA-QCR turbulence models, respectively..... 58
Figure 4.14. Streamlines on zoomed-in corner region of fine mesh results for cylinder of height y/d = 10. a) - c) Mach number contours for CKE, SST, and SA-QCR turbulence models, respectively..... 59
Figure 4.15. Fine mesh results with indicated turbulence models, showing normalized pressure on the flat plate surface, upstream of the cylinder with height y/d = 10. ... 60
Figure 4.16. Fine mesh results with indicated turbulence models, showing normalized pressure on the leading edge of the cylinder with height y/d = 10. 62

Figure 4.17. a) Skin friction coefficient × 10^3 and b) normalized surface pressure ratio lines and contours at y/d = 0 with SA-QCR turbulence model for cylinder of height y/d = 10. Flow from bottom to top. 64
Figure 4.18. Fine mesh results with varied incoming boundary layer height δ/d for cylinder with height y/d = 10. a) - j) δ/d = 0.25 to δ/d = 2.50 with constant increment of 0.25. Orange line represents sonic line. 66
Figure 4.19. Comparison of parameters of interest between empirical values [11] and fine mesh results for varied δ/d with cylinder of height y/d = 10. a) λ/d, b) B/d, c) h_{tp}/d. 67
Figure 4.20. Fine mesh results with varied δ/d, showing normalized pressure on the flat plate surface, upstream of the cylinder with height y/d = 10. 69
Figure 4.21. Fine mesh results with varied δ/d, showing normalized pressure on the cylinder leading edge of the cylinder with height y/d = 10..... 70
Figure 4.22. Topological model of SWTBLI using streamlines at z/d = 0 for SA-QCR turbulence model with fine mesh and cylinder of height y/d = 10. 72
Figure 4.23. Grid independence study comparing the parameters of interest for laminar interaction. a) λ/d, b) B/d, c) h_{tp}/d. 74
Figure 4.24. a) Mach number and b) numerical Schlieren contours of extra fine mesh result at z/d = 0. Black line in a) is sonic line. 75
Figure 4.25. a) - b) Mach number contours where pink line represents sonic line, black lines represent empirical values for B and h_{tp}. c) - d) numerical Schlieren contours where orange line is sonic line and pink lines represent empirical values for B and h_{tp}. Reduced contour levels for b) and c). 77
Figure 4.26. Turbulent-to-laminar viscosity for laminar interaction. Orange solid line is a ratio of unity..... 78
Figure 4.27. Streamlines for laminar interaction, a) with and b) without Mach number contours..... 80
Figure 4.28. Streamlines on zoomed-in corner region for laminar interaction, a) with and b) without Mach number contour. 81
Figure 4.29. Normalized pressure ratio on the flat plate surface for laminar interaction. 83

Figure 4.30. Normalized pressure on the leading edge of the cylinder for laminar interaction 84
Figure 4.31. a) Skin friction coefficient × 10^3 and b) normalized surface pressure ratio lines and contours at $y/d = 0$ for laminar interaction. Flow from bottom to top. 86
Figure 4.32. Topological model of SWLBLI using streamlines at $z/d = 0$ for SA-QCR turbulence model with laminar inputs..... 87

NOMENCLATURE

Uppercase Letters

AL	-	attachment line
B	-	bow shock stand-off distance
C_f	-	skin friction coefficient
C_P	-	coefficient of pressure
C_μ	-	k-ε model constant
E	-	total energy
F	-	focus point
G	-	viscous flux vector
GR	-	growth rate
H	-	inviscid flux vector
M	-	Mach number
N	-	node
P	-	pressure
Pr	-	Prandtl number
Q	-	dependent variable vector
Re	-	Reynolds number
S	-	saddle
S'	-	half-saddle
$\dot{S}$	-	source term vector
SL	-	separation line
St	-	Strouhal number
T	-	temperature

Lowercase Letters

d	-	cylinder diameter
e	-	specific energy
f	-	frequency
h	-	cylinder height

h_{tp} - triple point height

k - turbulence kinetic energy

$\dot{q}$ - heat flux vector

r - radial coordinate

r^+ - non-dimensional wall distance in radial direction

Δr - constant non-dimensional wall spacing in radial direction

u - streamwise velocity

v - transverse velocity

w - spanwise velocity

x - streamwise coordinate

y - transverse coordinate

y^+ - non-dimensional wall distance in transverse direction

Δy - constant non-dimensional wall spacing in transverse direction

z - spanwise coordinate

Greek Letters

α - angle of attack

γ - ratio of specific heats

δ - boundary layer height, 99^{th} percentile of freestream velocity

ε - turbulent dissipation

θ - azimuthal coordinate

$\Delta\theta$ - constant non-dimensional wall spacing in azimuthal direction

κ - thermal conductivity

λ - separation length

μ - dynamic viscosity

$\tilde{\nu}$ - kinematic eddy viscosity parameter

ρ - density

σ - standard deviation

τ - stress tensor

φ - forward shock angle

ω - specific dissipation rate

Subscripts

∞	-	freestream conditions
0	-	stagnation conditions
1	-	conditions upstream of shock
2	-	conditions downstream of shock
n	-	normal shock conditions
WT	-	wind tunnel conditions
m	-	per unit length in meters
x	-	at position *x*
max	-	maximum
t	-	turbulent
th	-	thermal

CHAPTER 1
INTRODUCTION

1.1 Motivation

One of the limiting factors in the design of supersonic and hypersonic vehicles remains the prediction and control of shock wave/boundary layer interactions (SWBLIs or SBLIs) [1, 2]. These interactions generate high aerodynamic, thermal, acoustic, and structural loads and occur frequently on high-speed systems. Externally, they exist on control surfaces, where the interactions can significantly reduce the effectiveness of control surfaces and impair stability and control. Internally, they exist within engine inlets, where the interactions can lead to flow degradation and even unstart [1 - 3]. In order to design high-speed systems that are not prone to the impaired effectiveness or potential vehicle failure induced by SWBLIs, a fundamental understanding of the behavior and characteristics of these interactions is necessary.

As a result, much research has been conducted on SWBLIs since the 1950s [3, 4]. Such interactions are defined by two characteristic components: the state of the incoming boundary layer (laminar, transitional, or turbulent), and the geometry acting as the shock generator. In regards to the state of the incoming boundary layer, shock wave/*laminar* boundary layer interactions (SWLBLIs) are fairly accurately predicted [5]. Their interactions are captured well with both experimental and computational methods. However, shock wave/*turbulent* boundary layer interactions (SWTBLIs or STBLIs) are inherently unsteady, and after over 65 years of research, the cause of this unsteadiness is still not fully understood [4]. Due to this lack of understanding and their common occurrence on high-speed systems, turbulent interactions remain the subject of the vast majority of SWBLI research. Lastly, shock wave/*transitional* boundary layer interactions (XSWBLIs), which are also inherently unsteady, have received comparatively little attention. There is increased emphasis on increasing surface area of laminar flow to reduce heat transfer in high-speed systems, and a growing interest towards natural laminar flow (NLF). As a result, boundary layer transition is pushed further aft on high-speed systems to the point where a transitional interaction may now occur on control surfaces. Since

reentry capsules also undergo boundary layer transition, a transitional interaction has the potential to occur on all high-speed systems. To explore the fundamental dynamic behavior of transitional interactions, recent research conducted at the University of Tennessee Space Institute (UTSI) has aimed to experimentally characterize these [6, 7]. Since the extent of a transitional interaction is bounded by those of a laminar and turbulent interaction [8], a useful step in characterizing this behavior is to understand the scales of the limiting cases. Prior efforts have strongly recommended that numerical studies are performed in collaboration with experimental studies [4, 9], and since the in-house work has been conducted for transitional and turbulent interactions thus far [6, 7], the current numerical work is focused on the turbulent regime, but explores a laminar interaction as well.

In regards to the geometry acting as the shock-generator, the classifications of interactions include 2-D or 3-D, and open or closed interactions [10]. Examples of fundamental 2-D interactions are impinging shock waves or compression ramps, while examples of fundamental 3-D interactions are standing cylinders or swept compression ramps. 2-D interactions are inherently closed in the sense that the flow recirculates in an upstream region, while 3-D interactions can take on either an open or closed definition. Examples of open interactions are swept compression ramps and sharp fins, since the flow does not recirculate in an upstream region, but instead is continuously swept downstream. The standing cylinder and blunt fin are special cases in which a closed, 3-D interaction exists. For the recent work at UTSI, the geometry of interest was a standing cylinder.

Many effective experimental and computational capabilities that are used to resolve the unsteady interactions, such as particle image velocimetry (PIV) and large eddy simulation (LES), have only recently become available in the measurement and prediction of turbulent interactions [4]. In terms of computational resources, LES remains too expensive for many applications and because of this, Reynolds-averaged Navier-Stokes (RANS) simulations remain the dominant simulation technique for high-Reynolds number flows. However, obtaining accurate RANS simulations for inherently unsteady flows, such as those involving turbulent or transitional interactions, can be difficult or even impossible. The limit to the effectiveness of steady-state RANS simulations should thus be kept in mind.

1.2 Objectives of Current Work

The primary goal of the current study is to provide a better understanding of a cylinder-induced SWTBLI. The secondary and underlying goal is to establish the boundaries from a laminar and turbulent interaction in order to define the limiting cases for a transitional interaction, and help guide experiments at UTSI. Computational methods are employed in order to characterize the flow. The following objectives are set in the current work:

1. *To determine the effectiveness of performing steady-state RANS simulations for the turbulent interaction, which is an inherently unsteady problem.*

   With a drive to generate computationally inexpensive results for an otherwise expensive simulation, this study will compare RANS simulations with in-house experiments, experiments found in literature, and steady-state and time-accurate simulations found in literature. The findings determine the need for time-accurate simulations for this problem, and if a characterization can be made using only RANS simulations.

2. *To characterize the laminar interaction using RANS simulations.*

   The results of a laminar and turbulent interaction characterization will provide the limiting cases for future studies involving a transitional interaction. The characterization of both types of interactions will consist of shock structure alignment with experimental values, analysis of pressure distribution and flow structure, and assessment of the peak pressure value and location. As before, these data will be compared to experiments reported in literature.

3. *To analyze the effect of incoming boundary layer height on the strength of the interaction.*

   Although the Reynolds number has a larger effect on the interaction than the boundary layer height does [11, 12], it is important to analyze how the interaction changes when the Reynolds number is kept constant and the boundary layer height is changed. As this is a simple change to the boundary conditions of the simulation, computational methods excel at addressing parametric questions regarding the boundary layer dimension. This is in contrast to experimental work, which is constrained to a boundary layer of fluid scales.

CHAPTER 2
LITERATURE REVIEW

As mentioned in Chapter 1, the two classifications of SWBLIs are determined by the state of the incoming boundary layer and the geometry acting as the shock generator. An overview of prior work is presented for SWBLIs using either a cylinder or blunt fin, as these two geometries generate the same upstream interaction and can thus be considered equivalent and will be used interchangeably throughout [12, 13]. First, a general overview of the cylinder-induced interaction structure is presented. This structure varies in scale across the different boundary layer interactions, but not in its shape. Then, the details and special features of a turbulent and laminar interaction, respectively, are discussed.

2.1 Cylinder-Induced Interaction Structure

Experimental work in the past has primarily focused on the upstream region of a cylinder-induced interaction [14]. In particular, non-intrusive flow diagnostics, such as Schlieren and PIV, have typically been performed along the upstream centerline of the streamwise-transverse plane, as indicated by the green plane in Figure 2.1. Additionally, intrusive flow visualization techniques, such as oil flow visualization and pressure-sensitive paint (PSP), have typically been performed in the streamwise-spanwise plane, on the surface that generates the boundary layer, as shown by the golden plane in Figure 2.1.

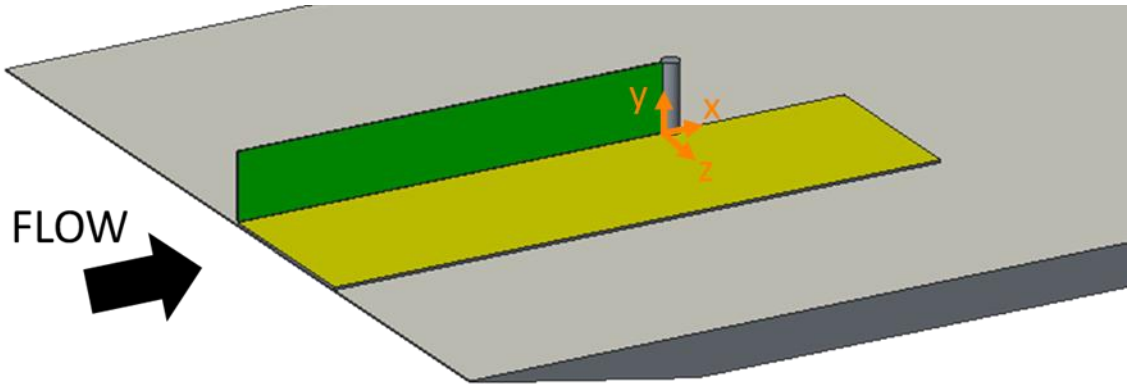


Figure 2.1. Cylinder on a flat plate, indicating views of interest. Green plane in *x*-*y*, golden plane in *x*-*z*.

In the *x-y* plane, for so-called "semi-infinite" cylinder- and blunt-fin-induced interactions, a lambda shock structure exists in the upstream region on the horizontal centerline, as indicated by the schematic in Figure 2.2. The diameter of the cylinder, *d*, is one of the dominant factors of the interaction scale, and all other parameters are thus normalized by *d*. The height of the cylinder, *h*, is also of particular importance because it dictates whether the interaction is considered semi-infinite or a function of *h/d* [11, 12] and *δ/d* [12], where *δ* is the incoming boundary layer height. Dolling and Bogdonoff [12] identified this semi-infinite requirement as h/h_{tp} > 2-3, where h_{tp} denotes the triple point height, and also estimated a guide of *h/d* > 2.4. Özcan and Yüceil [14] reported that this should be at *h/d* > 2.5, but used larger increments in their tests. Once the semi-infinite height is met, increasing *h* no longer changes the interaction structure. The interactions considered in this work are semi-infinite. In Figure 2.2, flow separation occurs at the separation length, *λ*, and generates an oblique shock, known as the forward shock, with

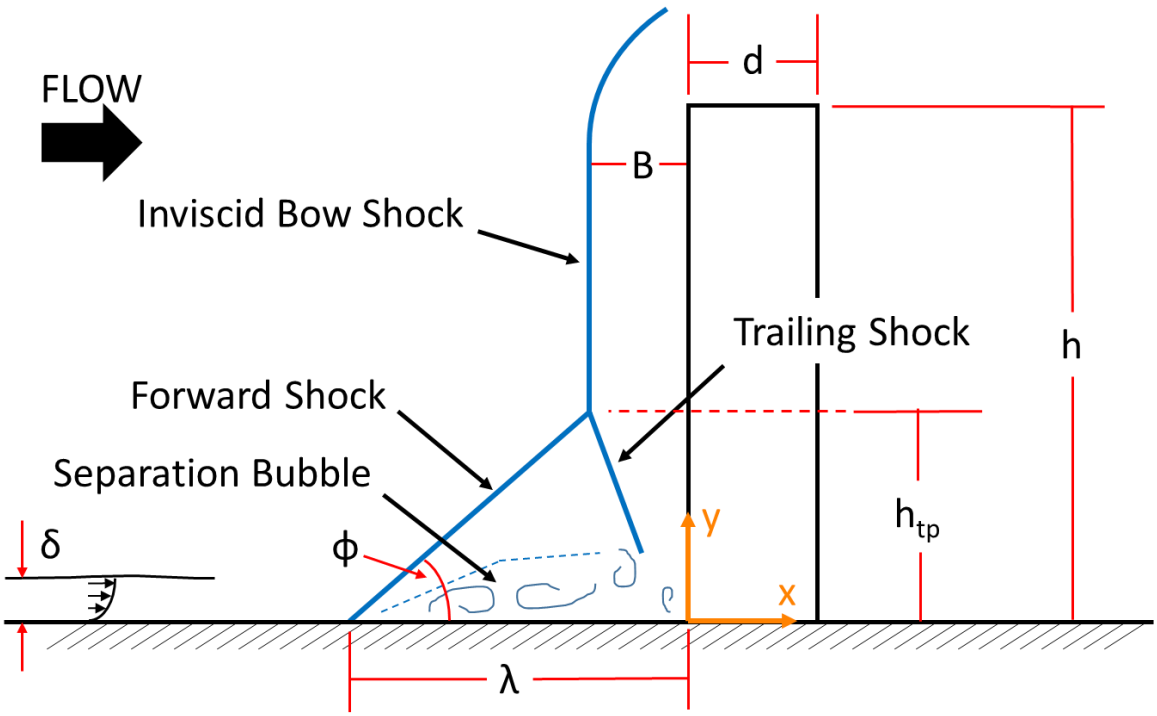


Figure 2.2. Front view schematic of a cylinder-induced shock wave/boundary layer interaction.

forward shock angle φ. This forward shock impinges upon the inviscid bow shock, which has stand-off distance B, at the triple point, where a bifurcation leads to the development of the trailing shock. Underneath the lambda shock, a separation bubble is formed, which consists of several vortices. The vortex structure varies depending on the state of the incoming boundary layer, and is discussed below for turbulent and laminar interactions. The trailing shock does not come into contact with the floor, but instead ends where it intersects with the separation bubble.

In the x-z plane, the separation shock is seen to curve outboard, as shown in Figure 2.3. Note that this view only refers to the floor surface and does not include the trailing shock, as this ends at the separation bubble. The largest extent of the separation shock is on the centerline with length λ, and as horseshoe vortices wash outboard, the distance between the cylinder and separation shock line is reduced. Vortex shedding also occurs just downstream of the cylinder, but this is symmetric in a statistical sense.

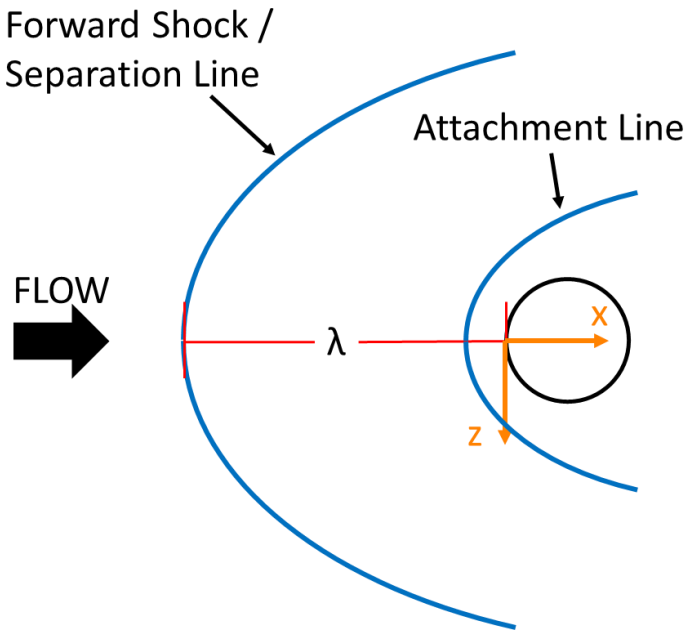


Figure 2.3. Top view schematic of a cylinder-induced shock wave/boundary layer interaction, indicating the surface interaction.

Sample Schlieren imaging and oil flow visualization from Lash et al. [6] for a turbulent interaction are shown in Figure 2.4a and b, respectively, and allow for a qualitative comparison to the schematics in Figure 2.2 and Figure 2.3, respectively. Note that all of the blue lines in the schematics are visible in the sample experimental results.

2.2 Turbulent Cylinder-Induced Interaction

As the turbulent interaction has the most practical applications, it is discussed first. The separation length is one of the key parameters of interest; Westkaemper [11] identified that λ/d remains constant at approximately $\lambda/d = 2.65$ for an interaction where $h/d > 1.13$ over $M_\infty = 2.0\text{-}21$, where M_∞ represents the freestream Mach number. This was also observed by Dolling and Bogdonoff [12] and Brusniak and Dolling [13]. However, experimental work by Lash et al. [6] and Combs et al. [7], and computational work by Yamamoto and Takasu [15], have all reported values closer to $\lambda/d = 2.0\text{-}2.4$. A distribution of separation lengths from the in-house work of Lash et al. [6] is shown in Figure 2.5, which indicated a

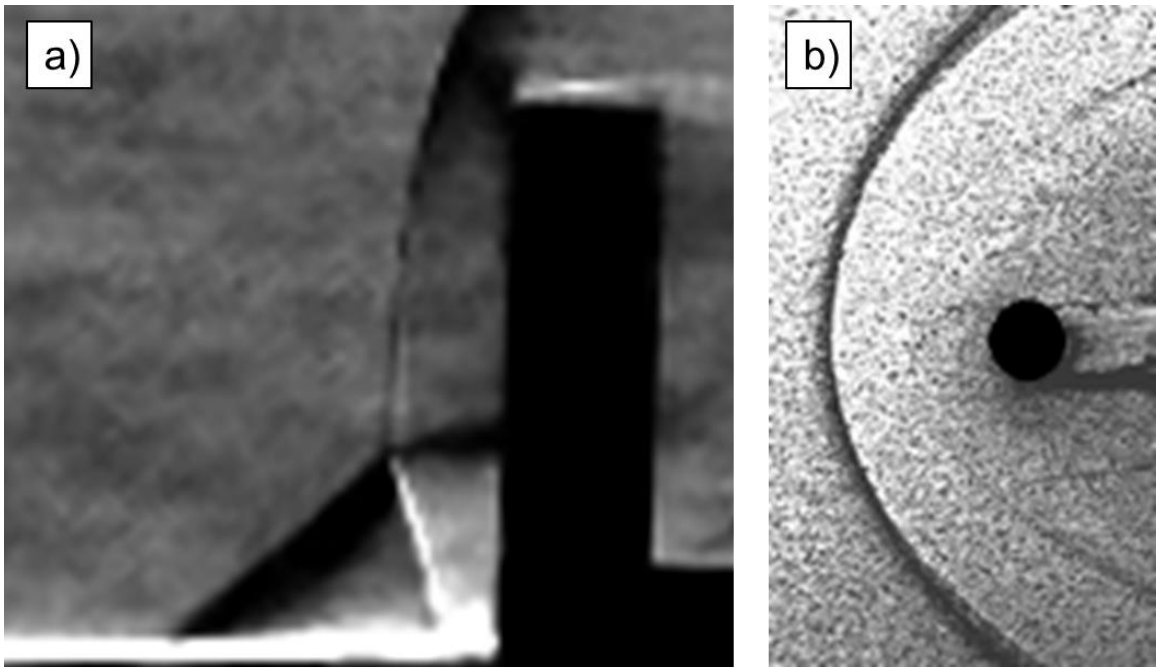


Figure 2.4. Sample a) Schlieren imaging and b) oil flow visualization for a turbulent interaction. Figure from Lash et al. [6].

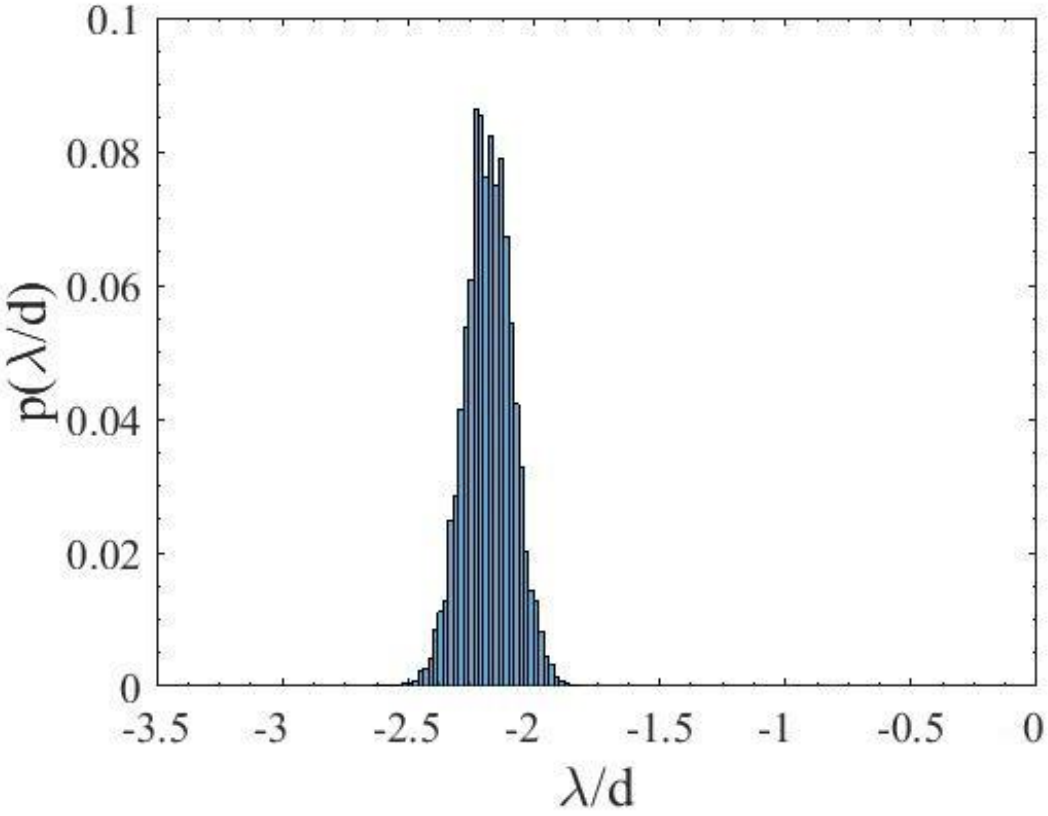


Figure 2.5. In-house experimental results indicating probability density function of separation length. Figure from Lash et al. [6].

mean value of around λ/d = 2.15. These discrepancies may have arisen due to differences in Reynolds number, *Re*, or δ, which both affect the scale of the interaction [12, 13, 16]. The effect of δ/d at a constant *Re* will be investigated more closely in this study.

Westkaemper [11] also generated empirical equations for the remaining parameters of interest that are shown in Figure 2.2. The forward shock angle φ was determined by first finding the pressure coefficient, C_P, through Equation (2-1) [17], where 5.61 is an empirical constant, M_∞ is the freestream Mach number, Re_x is the local freestream Reynolds number at location x, γ is the ratio of specific heats, and P is the static pressure, and then applying oblique shock relations via the pressure ratio [18]. This is used in conjunction with B, which is found via the empirical Equation (2-2) [11], in order to determine a geometric formula for h_{tp}, which is shown in Equation (2-3) [11].

$$C_P = \frac{5.61}{\sqrt[5]{M_\infty Re_x}} = \frac{2}{\gamma M_1^2}\left(\frac{P_2}{P_1} - 1\right) \quad (2\text{-}1)$$

$$B/d = 0.19 + \frac{1.2}{M_\infty^2 - 1} + \frac{0.7}{(M_\infty^2 - 1)^2} \quad (2\text{-}2)$$

$$h_{tp}/d = (\lambda/d - B/d)\tan(\varphi) \quad (2\text{-}3)$$

The separation length is directly linked to a pressure rise in the upstream region. Pressure ratios comparing the computational data from Hung and Buning [16] with experimental data from Dolling and Bogdonoff [19] for a blunt fin interaction at $M_\infty = 2.95$, shown in Figure 2.6a, indicated an initial pressure rise near $x/d = -3$. However, Hung and Buning [16] calculated separation to occur around $\lambda/d = 1.7$ in 1985, as indicated by the streamlines in Figure 2.6b, at a point where the pressure ratio had already risen near its initial plateau. This pressure plateau was followed by a trough that retained $P/P_\infty > 1$, where P_∞ is the freestream pressure, which was then followed by the peak pressure just upstream of the blunt body. Computational results, which are able to resolve this near-wall region at a much greater ease than experiments, predicted the peak pressure location around $x/d = -0.1$ [15, 16]. There was a pressure decrease just downstream of the peak pressure that reached yet another trough around $x/d = -0.05$, followed by a small pressure increase [15, 16]. This study will attempt to identify the reason for the peak pressure location, which would allow for mitigation of this critical parameter.

Streamlines, such as those shown in Figure 2.6b, provide a more in-depth understanding of the vortex structure and underlying flow physics, and will be used to characterize the flow. Note that there is a discrepancy between the steady-state computational result from Hung and Buning [16] and the time-accurate computational result from Yamamoto and Takasu [15]. The steady-state result [16] indicated a single, large, primary vortex, as shown in Figure 2.6b, but the time-accurate result [15] indicated a set of smaller, counter-rotating, primary vortices; this set varied between one and three vortices over time. The variation in the number of primary vortices was also observed by Sedney and Kitchens [20], and this variation for the steady-state result is likely attributed

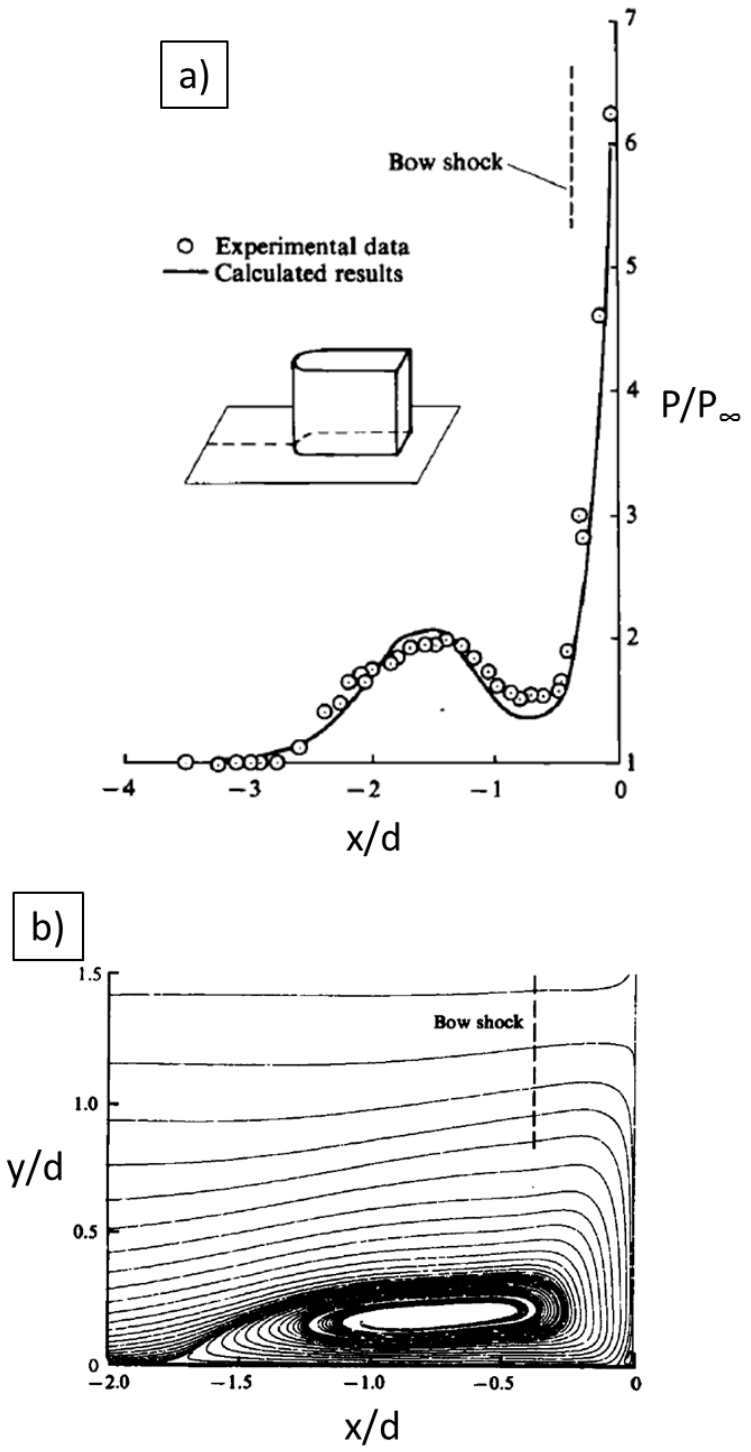


Figure 2.6. a) Blunt fin pressure ratio comparing computational results from Hung and Buning [16] with experimental results from Dolling and Bogdonoff [19] at M_∞ = 2.95, b) Streamlines of the computational results on the upstream centerline. Figures from Hung and Buning [16].

to the differences in the modeling approach. However, there may also be a factor due to the unsteadiness in the interaction, such as the combined low- and high-frequency oscillations within the lambda shock structure. Lash et al. [6], Clemens and Narayanaswamy [10], Brusniak and Dolling [13], and Dolling and Brusniak [21] have all investigated this behavior and concluded that the forward shock undergoes low-frequency oscillations (f < 1 kHz), whereas the separation bubble, and hence the trailing shock, undergoes high-frequency oscillations ($f \geq 1$ kHz). As the present study focuses on steady-state interactions, a characterization of the frequencies will not be made; however, it is important to remember that the flow is inherently unsteady, and that this affects the vortical structure, among other things, for a steady-state result.

2.3 Laminar Cylinder-Induced Interaction

As laminar boundary layers are generally more susceptible to flow separation than turbulent boundary layers [22, 23], the scales of the interactions are inherently greater. While the initial pressure rise and flow separation for a turbulent interaction occur near $x/d = -3$ and $\lambda/d = 2.65$, respectively, these values are approximately $x/d = (-9)$-(-6) for a laminar interaction [8]. Leidy et al. [24] found separation to occur closer to λ/d = 5.5-6 at $M_\infty = 6$. Itoh and Mizoguchi [25] and Mortazavi and Knight [26] note that similar unsteady behavior exists for a laminar interaction as for a turbulent interaction, and have estimated Strouhal numbers from St = 0.032-0.113 through experiments [25] to St = 0.697 through computation [26], in contrast to St = 0.023-0.035 [27] for a turbulent interaction. A schematic of the vortex structures for a laminar interaction is shown in Figure 2.7, where *N, F, S,* and *S'* represent nodes, foci, saddles, and half-saddles, respectively. Furthermore, *AL* represents an attachment line and *SL* represents a separation line.

Present computational capabilities lend themselves well towards solving laminar interactions. Knight and Degrez [5] and Holden [28] state that aerodynamic and thermal loads are accurately predicted using RANS simulations given that the mesh is adequately resolved. Holden [28] notes that gridding and numerical issues, in particular, have taken a long time to address and overcome, but have now fully matured. Dolling [4] states that grid-adaptation is an essential tool in solving laminar interactions.

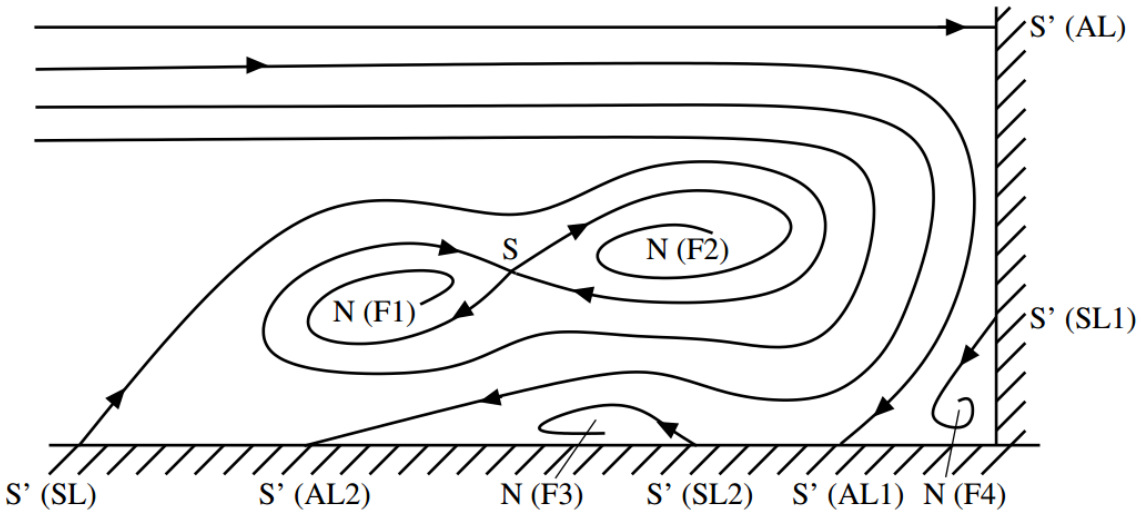


Figure 2.7. Schematic of streamlines indicating vortex structure for a laminar interaction. Figure from Itoh and Mizoguchi [25].

The empirical equations for a laminar interaction are very similar to those for a turbulent interaction. Since the bow shock is inviscid, Equation (2-2) does not depend on the state of the incoming boundary layer, and thus remains valid. Furthermore, Equation (2-3) is a geometric formula and is thus also valid. The difference occurs in φ, which was calculated through C_P in Equation (2-1). Truitt [17] proposed an alternate version, shown in Equation (2-4), which was valid for a laminar boundary layer. Note that the constant of 17 differs from that of a turbulent interaction and was found through an iterative process until the pressure ratio matched a guessed value. The constant was not proposed by Truitt [17] and not verified under other flow conditions, and may not hold valid in a different interaction.

$$C_P = \frac{17M_\infty}{\sqrt{Re_x}} = \frac{2}{\gamma M_1^2}\left(\frac{P_2}{P_1} - 1\right) \tag{2-4}$$

2.4 Transitional Cylinder-Induced Interaction Bounds

Addressing the scales of separation length and triple point height for the limiting cases of laminar and turbulent interactions paves the way for further research into transitional interactions. Kaufman et al. [8] have stated that the parameters of interest for a transitional interaction are confined to the values obtained by laminar and turbulent interactions. This is visible in Figure 2.8, which shows the separation length for each type of boundary layer using kerosene lampblack flow visualization at M_∞ = 5, with flow from top to bottom. Moreover, Kaufman et al. [8], Lash et al. [27], and Murphree et al. [29] have shown that a transitional interaction exhibits traits closer to those of a laminar interaction near the centerline, and closer to those of a turbulent interaction near the outboard extents.

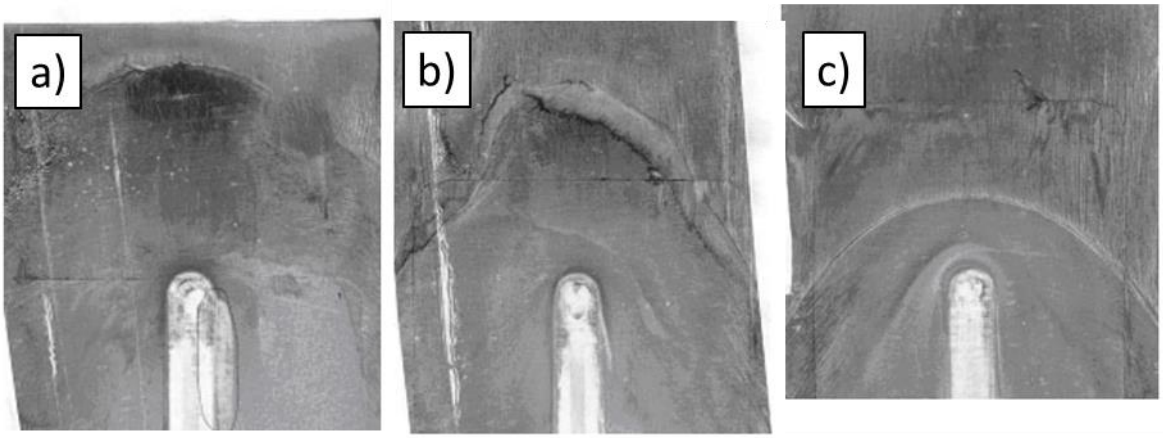


Figure 2.8. Kerosene lampblack flow visualization from top view of shock wave/ a) laminar, b) transitional, c) turbulent boundary layer interactions at M_∞ = 5. Flow from top to bottom. Figure from Murphree et al. [29].

CHAPTER 3
METHODOLOGY

The simulations were run on two high-performance desktops that used the operating system Ubuntu 16.04 (64-bit) and contained 64 cores of the type AMD Opteron™ Processor 6376 at 2300 MHz each, along with 256 GB RAM. Furthermore, a cluster was available that ran the operating system Red Hat® Enterprise Linux® Server 7.2 and contained 11 nodes at 32 cores each (352 total) of the type Intel® Xeon® E5-2630 v3 at 2400 MHz each, along with 64 GB RAM per node. This computing power was sufficient for the simulations performed. Mesh generation was performed using Pointwise, Inc., V17.3R4, and post-processing was conducted using Tecplot, Inc., 360 EX 2015 R2.

3.1 Flow Modeling Assumptions

This study assumed a continuum model for the supersonic flow. As such, the fluid could be modeled using scalars for density, ρ, temperature, T, and the velocity components u, v, and w. Air was the fluid of interest and was treated as a compressible, viscous, Newtonian fluid, and moreover as an ideal (or perfect) gas. The dynamic viscosity, μ, was determined via Sutherland's law [30, 31]. Stagnation conditions were assumed to be constant; and since RANS provides a statistical mean flow, this flow was considered to be steady-state.

Further physical assumptions that were made in this study include the use of smooth, adiabatic, no-slip walls on the boundaries of the wind tunnel walls, flat plate surface and strut, and on the cylinder. The cylinder was initially modeled at the same height in the experiment, but this was ultimately increased to ensure a semi-infinite behavior for an analysis concerning the height of the incoming boundary layer, which directly affects h_{tp} and thus h/h_{tp}. The flat plate leading edge, which was machined to be considered sharp, was modeled with a blunt leading edge of radius 127 μm (0.005 in) [32], which was representative of the machining tolerance. Lastly, the wind tunnel was assumed to provide flow with a freestream turbulence intensity of 3% and a turbulent-to-laminar viscosity ratio of 5.

3.2 Numerical Formulation

3.2.1 Governing Equations

Reynolds-averaged Navier-Stokes simulations were performed using Metacomp Technologies, Inc., (Metacomp) CFD++ v16.1 [33]. The compressible, perfect gas Navier-Stokes equations were solved in dimensional, Cartesian coordinates, and are listed in Equation (3-1), where Q is the dependent variable vector, H is an inviscid flux vector, and G is a viscous flux vector, as respectively described by Equations (3-2), (3-3), and (3-4). In Equation (3-1), $\dot{S}$ is the source term vector, and is zero except near physics source terms. The only source terms used in this study were at the far-field and are described later. Additional transport equations are solved when a turbulence model is active, and alter the terms μ and κ, the thermal conductivity, to be $\mu+\mu_t$ and $\kappa+\kappa_t$, respectively. These transport equations contribute to their own source term vectors. In Equation (3-3), E represents total energy. In Equation (3-4), $\dot{q}$ represents the heat flux vector and τ represents the stress tensor.

$$\frac{\partial Q}{\partial t} + \frac{\partial (H_i + G_i)}{\partial x_i} = \dot{S} \tag{3-1}$$

$$Q = \begin{bmatrix} E \\ \rho \\ \rho u \\ \rho v \\ \rho w \end{bmatrix} \tag{3-2}$$

$$H_i = \begin{bmatrix} (E+P)u_i \\ \rho u_i \\ \rho u u_i + P\hat{n}_x \\ \rho v u_i + P\hat{n}_y \\ \rho w u_i + P\hat{n}_z \end{bmatrix} \tag{3-3}$$

$$G_i = \begin{bmatrix} \dot{q}_i - u_j \tau_{jk} \\ 0 \\ -\tau_{ix} \\ -\tau_{iy} \\ -\tau_{iz} \end{bmatrix} \tag{3-4}$$

3.2.2 Turbulence Model Set-Up

The turbulence models used in this study were Menter's 2-equation shear-stress transport (SST) [34], the 1-equation Spalart-Allmaras (SA) [35] with quadratic constitutive relation (QCR) [36], simply referred to as SA-QCR here, and the 2-equation cubic k-ε (CKE) [37]. All turbulence models were turned on at the 11^{th} global time step, allowing for initial start-up transients to settle. The SST and CKE turbulence models used a turbulence under-relaxation parameter of 1, whereas the SA-QCR turbulence model used 0.75. The minimum level of turbulence quantities was 10^{-12} for all models, and the maximum ratio of turbulent-to-laminar viscosity was 10^{10} for all models. The Prandtl number was not directly specified, but maintained a laminar-to-turbulent Prandtl ratio of 0.8 and a turbulent Schmidt number of 0.7 for all models. Wall-functions were not implemented here. None of the turbulence models included baroclinic effects on production. The initial values for each turbulence model were computed with Metacomp's turbulence initialization tool. [33]

3.2.2.1 SST

The SST model solves for the turbulence kinetic energy, k, and specific dissipation rate, ω [38]. A wall-distance file was computed which was used to measure the distance from every cell to its closest wall [33]. Turbulence terms in the near-wall region were determined using Metacomp's ε/ω boundary condition formulation v15.1 [33], but were also affected by the source terms, which depend on the wall-distance. Metacomp's compressibility correction was implemented in combination with a wall-bounded flow type [33].

3.2.2.2 SA-QCR

The SA model solves for the kinematic eddy viscosity parameter, $\tilde{\nu}$ [38]. Similar to the SST model, a wall-distance file was computed. The compressibility correction was implemented again for wall-bounded flows. The curvature correction was implemented to account for rotation and curvature effects [33], as these were strong factors in the interaction. These effects modified the calculation of $\tilde{\nu}$ [33]. Also, the QRC option was enabled, which enhances stress predictions and improves performance in boundary layers. This option modified the Reynolds stress term [33].

3.2.2.3 CKE

The CKE model solves for k and turbulent dissipation, ε [38]. Metacomp's compressibility correction for wall-bounded flows was active again. The dimensionless constant C_μ was formulated using the Goldberg formula [33], which is recommended for flows with impinging or stagnating regions. The realizability criterion used Bradshaw's constant [33], which is recommended for high-speed flow and for impinging or stagnating flow. The CKE model was not only used for the cylinder-interaction, but also to determine the flow conditions downstream of the flat plate leading edge shock and the growth of the boundary layer. As such, a leading-edge transition model [39] was implemented for this non-cylinder-interaction flow, which creates laminar flow near the leading edge until laminar separation is detected, after which the standard CKE model is applied [33].

3.2.3 Time Integration Set-Up

The steady-state solver was set to integrate the governing equations point-implicitly through the backward (or upwind) Euler method [38]. Simulations were run for 5000 global iterations to ensure that all residuals were flat-lined and no longer varied. The Courant-Friedrichs-Lewy (CFL) number was ramped linearly from 1 to 10 over the course of the first 100 iterations. When a divergence is detected in the solver, an automatic CFL number adjustment procedure (ACAP) takes place, which cuts the current CFL number in half and implements a new ramping schedule with a maximum of 0.95 times the CFL number when divergence was detected. A multi-grid W-cycle was implemented with 4 cycles and 20 levels. Non-strong agglomerations were allowed that were re-computed every 5 steps until the agglomeration had 1 group in its level. Time-step temporal smoothing was activated with a factor of 0.5. Time-step spatial smoothing was also turned on with 4 smoothing passes and a maximum time-step growth factor of 1.5.

3.2.4 Spatial Discretization Set-Up

The spatial discretization was 2^{nd} order. A continuous total variation diminishing (TVD) flux limiter was applied with nodal base polynomial types and out-of-face viscous terms. A 1^{st} to 2^{nd} order blending function for the backward Euler scheme was applied between 1000 and 1100 global time-steps. This ensured that transients in the solution

settled with a 1st order scheme before switching the solver to a 2nd order scheme. Typically, the residuals of the 1st order solution had dropped 4-5 orders of magnitude by the time the blend from 1st to 2nd order occurred.

3.2.5 Riemann Solver Set-Up

The Harten-Lax-van Leer-Contact (HLLC) scheme was used for the upwind discretization of the inviscid fluxes in CFD++ [33]. This approximate scheme, along with the TVD flux limiter, avoided oscillations [33]. A supersonic pressure switch was active which detected strong pressure gradients, i.e. shocks, and added dissipation in this region. Lastly, the carbuncle control was activated, which was used to reduce the dissipation error ahead of the bow shock in the nose region of the cylinder. This error arises when the solver switched from a hyperbolic to an elliptic method. The carbuncle control adjusted the maximum pressure factor to be 0.25.

3.3 UTSI Experiments

Experimental runs for a turbulent interaction were conducted by Lash et al. [6] and Combs et al. [7] at UTSI in a planar, low-enthalpy, blowdown wind tunnel with a test section size of 203.2 mm × 203.2 mm. High-speed Schlieren imaging [6] and 2-component PIV [7] were the two techniques employed for data collection. A 3.175 mm diameter, 12.7 mm tall brass cylinder was used to generate the interaction, resulting in an $h/d = 4$. The triple point was measured around $h_{tp}/d = 1.4$ [6], resulting in an $h/h_{tp} = 2.85$, which can be considered semi-infinite according to Dolling and Bogdonoff [12]. The cylinder was mounted on a flat plate of 304.8 mm length × 203.2 mm width at a distance of 25d downstream of the leading edge of the flat plate, as indicated by the schematic in Figure 3.1. This location has been verified to generate a fully turbulent interaction [6, 7].

The flat plate was angled downward at $\alpha = -2.9°$ in the experiment in an attempt to generate a zero pressure gradient on the upper surface. This angle was also applied to the CFD model by applying trigonometric identities to the u and v-velocity components. The coordinate system thus remained as initially indicated by Figure 2.2 and Figure 2.3. This configuration simplifies mesh generation and post-processing.

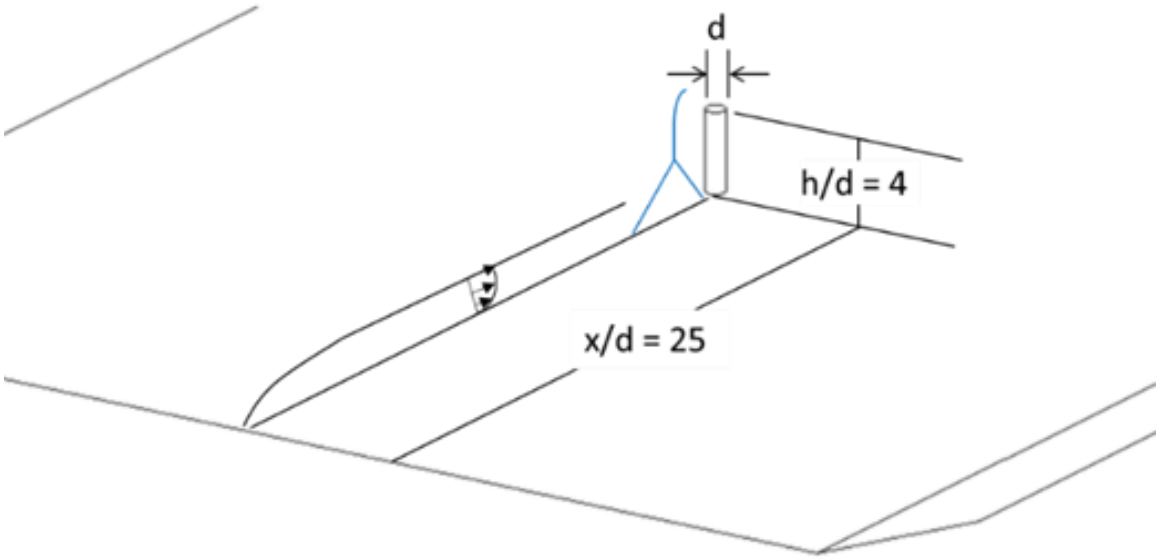


Figure 3.1. Schematic of the cylinder located on the flat plate.

The experiments have reported wind tunnel stagnation conditions, freestream velocity, and Mach number [6, 7], and have captured velocity and Mach number over the upper surface of the flat plate around $x/d = -19.5$ [7]. The wind tunnel stagnation conditions were used to calculate wind tunnel freestream conditions via isentropic relations [30], and oblique shock relations [18] were employed to determine the flow properties on the flat plate upper surface. The summary of these conditions, both reported and calculated, is provided in Table 3.1. As the coordinate system was angled, the wind tunnel freestream velocity of 507 m s^{-1} was decomposed such that $u_{\infty,WT} = 506.8$ m s^{-1} and $v_{\infty,WT} = -25.67$ m s^{-1}. This was not necessary for the flat plate upper surface, as the flow became tangential.

The primary comparisons made between in-house experiments and the current numerical work were against the Schlieren work of Lash et al. [6], as the Schlieren data were more statistically robust than the PIV data from Combs et al. [7]. The parameters of interest, namely λ and h_{tp}, from Lash et al. [6] were directly used for comparison. Recall from Figure 2.5 that a mean value of around $\lambda/d = 2.15$ was determined. Using B/d from Equation (2-2) along with the conditions in Table 3.1 and $\varphi = 41°$, obtained from Schlieren imaging [6], Equation (2-3) results in $h_{tp}/d = 1.24$, which was within 10% of the observed value of $h_{tp}/d = 1.35$ from Lash et al. [6].

Table 3.1. Flow conditions captured by experiments from Lash et al. [6] and Combs et al. [7] for wind tunnel and Combs et al. [7] for flat plate.

	Wind Tunnel Conditions	**Flat Plate Conditions at $x/d = -19.5$**
P_0 **[kPa]**	210.0	209.9
P_∞ **[kPa]**	26.425	31.1
T_0 **[K]**	286.8	286.8
T_∞ **[K]**	158.6	166.2
Re_m **[m^{-1}]**	2.72×10^7	2.84×10^7
M_∞ **[-]**	2.01	1.905
$\vec{v}_\infty$ **[m s^{-1}]**	507	493

3.4 Domain Definition and Mesh Generation

Described below is the process with which the final computational domain was determined, and the specific details of that domain. The first simulation that was performed included not only the cylinder, but also the entire flat plate and strut, as well as the full width and height of the wind tunnel test section, as shown in Figure 3.2. A structured, hexahedral mesh was used with non-dimensional wall distance $y^+ = 30$ and growth rate $GR = 1.2$; therefore, wall functions were implemented to model the flow between the buffer layer and the surfaces. Note that this was the only simulation performed that used wall functions. The objective here was to determine whether or not the wind tunnel walls influenced the interaction, and the conclusion was that the walls were far enough away from the cylinder-interaction to allow for domain reductions.

Next, the problem was split up into 2 domains: one that solved for the flow over the flat plate upper surface, and one that solved for the cylinder-interaction, as based on a method employed by Chaudhry et al. [40]. The flow over the 2-D flat plate without the cylinder was solved first in order to accurately capture the boundary layer growth on the centerline. Then, slices of the flow perpendicular to the flat plate surface were taken and

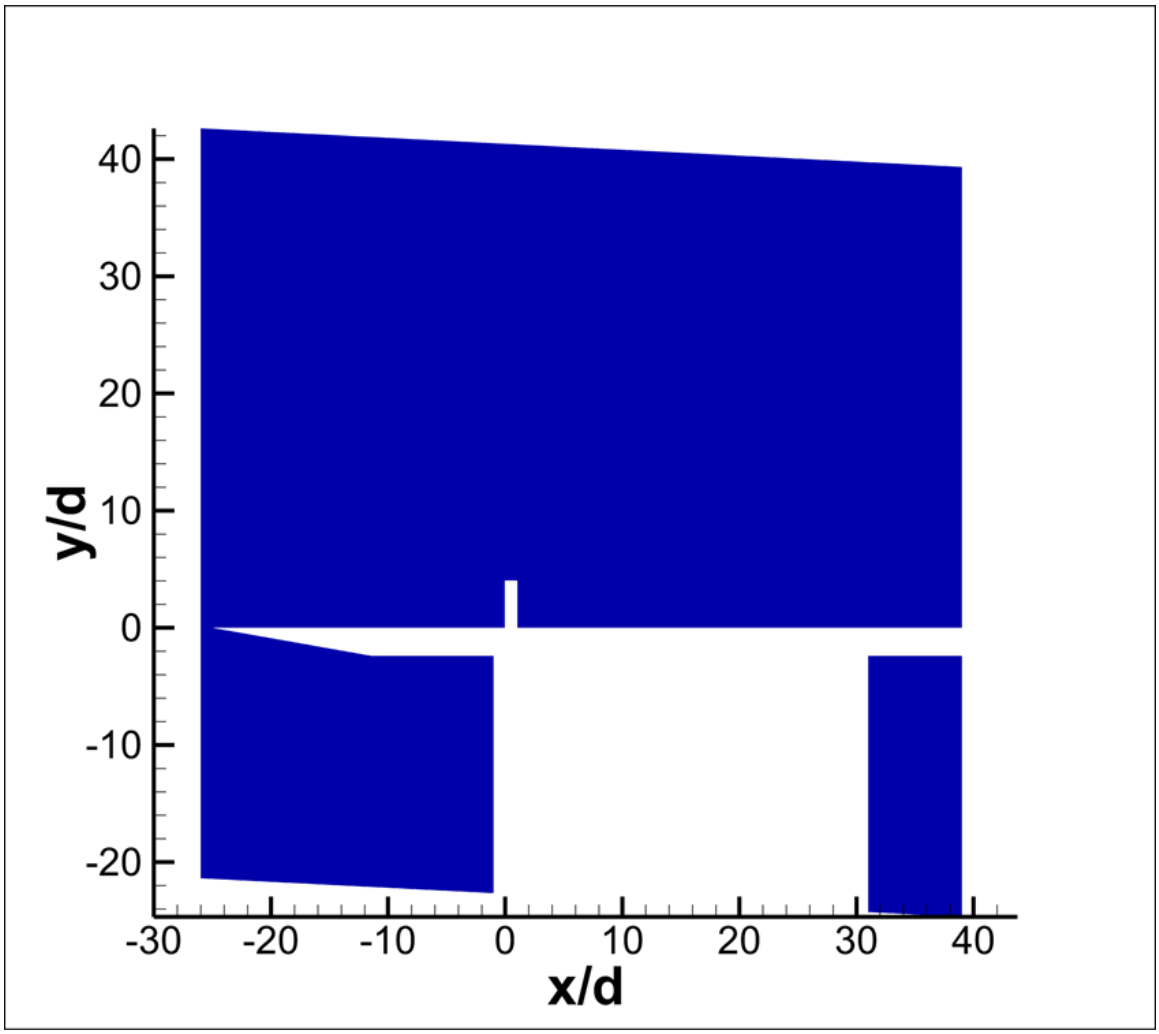


Figure 3.2. 3-D domain of the first simulation using full width and height of the test section. This was used to test for sidewall influence and identify possible domain size reduction.

used as an inlet profile to the cylinder-interaction, whose domain was then represented by a 3-D box. The advantages to using this method were two-fold: first, the domain for the cylinder-interaction was smaller, therefore allowing for a finer mesh and thus better resolution; second, the domain for the cylinder-interaction was no longer bounded by the flat plate in the sense that various δ/d could be tested. Also, this method allows for the cylinder to be tested at various locations downstream of the leading edge of the flat plate without re-meshing, which may be beneficial in the future.

3.4.1 Flat Plate Flow

3.4.1.1 Initial Domain Size Reduction

As mentioned above, the full-test-section solution of the domain in Figure 3.2 indicated that a domain size reduction was possible, as there was no interference by the wind tunnel walls. Based on the freestream flow of the full-test-section solution, it was determined that the domain shown in Figure 3.3 would capture all of the flow physics, while also allowing for greater mesh refinement. The inlet boundary was extended to $x/d = -30$, or $5d$ (15.875 mm) upstream of the flat plate leading edge, in order to ensure there were no disturbances from the leading edge bow shock. The boundary condition applied to the inlet was a Musker

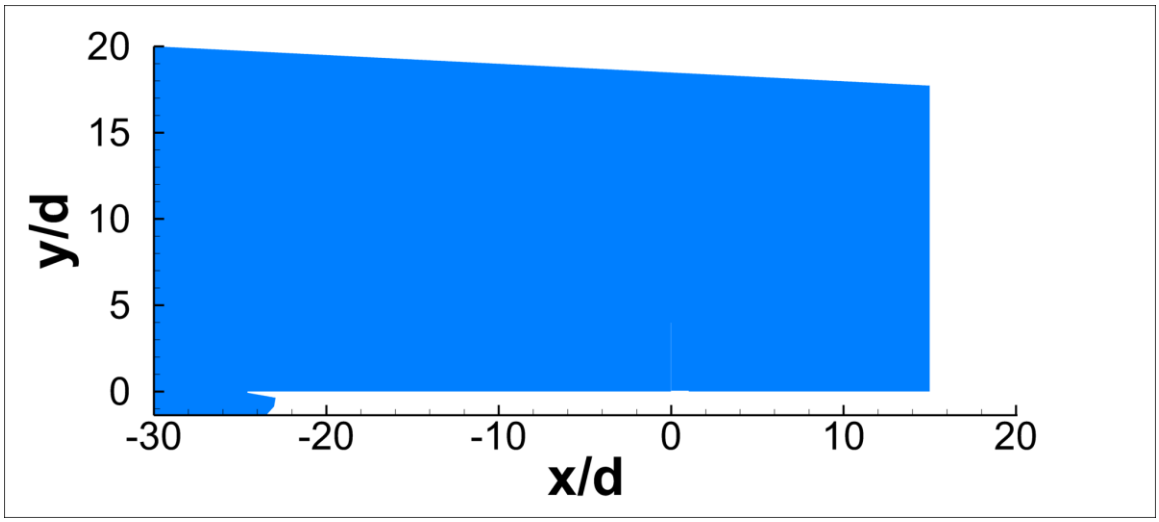


Figure 3.3. Medium 2-D flat plate domain with added forward section, reduced upper and lower flat plate surface extent, and reduced height.

turbulent boundary layer profile [41], which used the wind tunnel freestream conditions from Table 3.1 along with a specified boundary layer height of 12.7 mm on the wind tunnel walls in order to develop a turbulent inlet profile that extended across the entire boundary. The streamwise extent was shortened to x/d = 15, and a zero-gradient outflow was applied as the downstream boundary condition. The domain extent beneath the flat plate lower surface was significantly reduced, as this minimally factored into the flow over the upper surface. Nevertheless, a small domain section at the lower surface was maintained to allow for the bow shock to develop on both sides of the flat plate, and thus rule out any blockage. As before, the outlet boundary condition at the lower surface was a zero-gradient outflow. A comparison with the full-test-section solution indicated that there was no change to the flow on the upper surface, and so this reduction at the lower surface was deemed feasible. The upper height of the domain was reduced to y/d = 20 at the inlet and approximately y/d = 18 near the outlet. The far-field boundary conditions were set to a characteristics-based inflow/outflow, which is Metacomp's far-field-type boundary condition.

The final mesh for the domain of Figure 3.3 is shown in Figure 3.4. A first-pass was conducted with a structured, hexahedral mesh in order to more accurately determine the shock locations. Based on this, the final mesh was reconfigured for shock-alignment, as indicated by the green lines. A close-up of the flat plate leading edge, indicating the bow shock and two Mach waves emanating from the surface near the leading edge, is shown in Figure 3.5. This mesh consisted of hexahedral cells as well, but with the exception of a few unstructured, tetrahedral domains that can be identified in Figure 3.5 by the triangular domain zones. A total of 7 unstructured, tetrahedral domain zones (out of 83 total) were necessary to match the angled, shock-aligned domain zones with the surface. The walls were created with y^+ = 1 and GR = 1.1, such that the entire mesh consisted of 1.2 million cells.

3.4.1.2 Final Domain Size Reduction

An attempt was made to further reduce the boundary height, since the freestream conditions downstream of the flat plate leading edge shock were relatively constant. Simply coarsening the mesh in this region was found to be inappropriate, as it under-resolved the

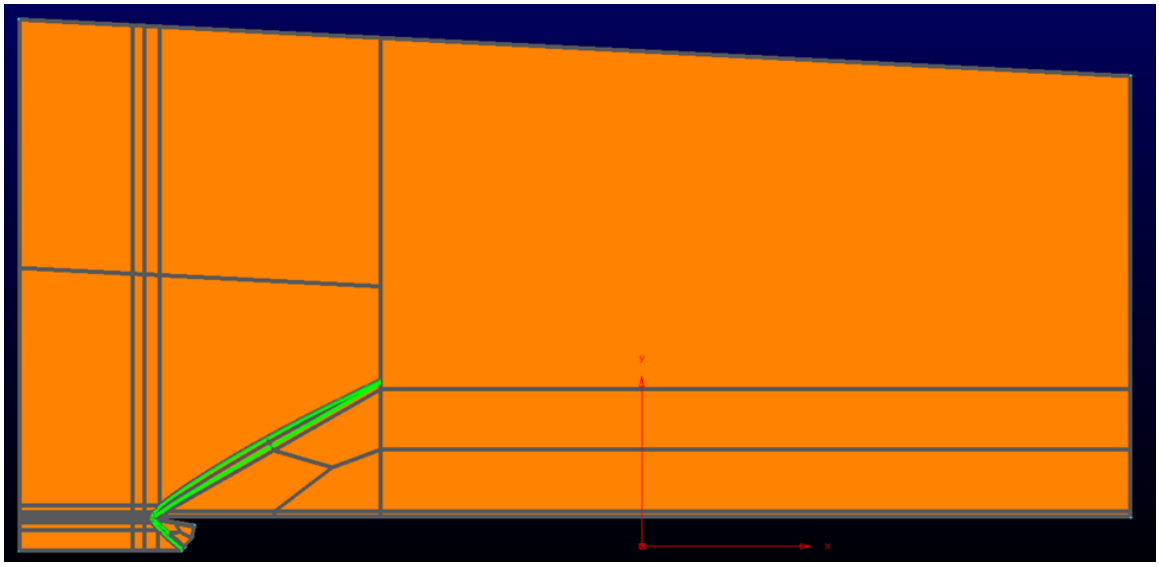


Figure 3.4. Medium 2-D flat plate mesh in *x*-*y*. Mesh domain zones are shown in grey, and shock-alignment is shown in green.

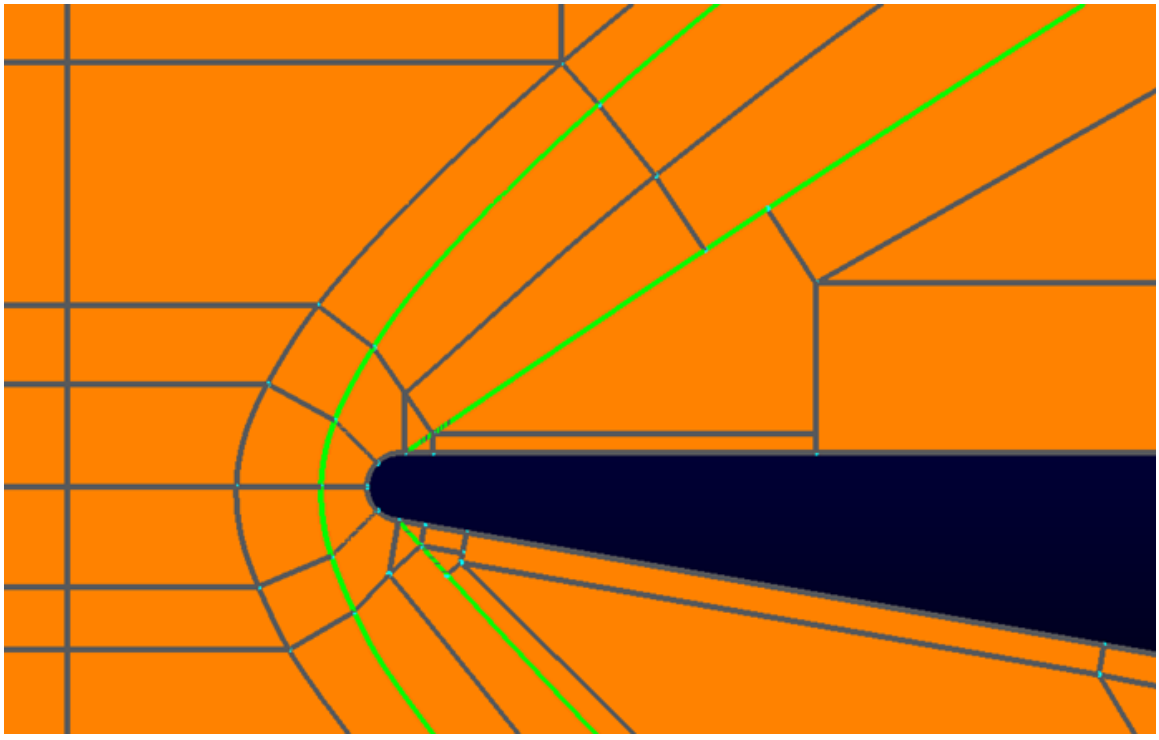


Figure 3.5. Close-up of leading edge section of the medium 2-D flat plate mesh. Mesh domain zones are shown in grey and shock-alignment is shown in green.

shocks and smeared them over several cells. Therefore, the height of the upper domain was reduced to y/d = 10 at the inlet and approximately y/d = 8.7 at the outlet, with the goal that the cell count could be reduced while increasing the accuracy of the solution. This height-shortened domain is shown in Figure 3.6.

Since the flow above the upper surface becomes tangential to the surface, the upper boundary above the flat plate may follow suit. From the flow solution for the domain of Figure 3.3 it was determined that despite the far-field condition being implemented, the flat plate leading edge shock had not dissipated out by the time it reached the upper boundary, and was reflecting back into the domain. This reflection impinged onto the flat plate boundary layer. In order to mitigate this issue, far-field absorbing layers were applied to the upper boundary. These posed the only contribution (other than the turbulence model) to the source term vector, $\dot{S}$, in the RHS of Equation (3-1). Physically, the absorbing layers acted as a sponge boundary, where the flow was damped to user-specified freestream values over the course of several layers. The shock dissipated within these damping layers and did not reflect back into the domain, thus allowing for the implementation of the domain in Figure 3.6. The walls here were created with y^+ = 0.1 and GR = 1.1; the fineness was required to properly resolve the small boundary layer in the vicinity of the leading

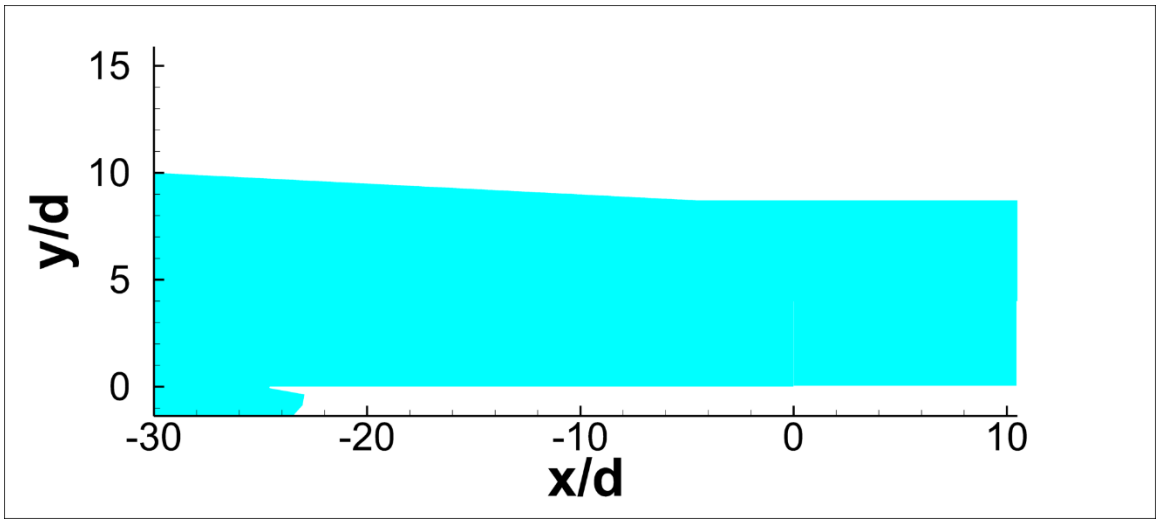


Figure 3.6. Smaller 2-D flat plate domain with reduced upper flat plate surface extent, and reduced height.

edge. A comparison between the solutions generated by the domains of Figure 3.3 and Figure 3.6 yielded no significant difference in the freestream or on the boundary layer.

3.4.1.3 2-D and 3-D Comparison

In order to assess the extent of the turbulent cylinder-interaction, and to provide a comparison between the 2-D and 3-D flows over the flat plate, a 3-D version of the domain in Figure 3.6 was generated. The domain for this 3-D version is shown in Figure 3.7 and used the same dimensions as those in Figure 3.6. The mesh for the domain in Figure 3.7 was created in two directions: the flat plate flow remained in the *x*-*y* plane and the mesh from Figure 3.4 was extruded to $z/d = 5$. The cylinder-interaction section was created in a similar manner, where a base mesh in *x*-*z* was generated, as shown in Figure 3.8, and extruded first to match the height of the cylinder at $y/d = 4$. Then, the top of the cylinder was closed off and the mesh was extruded again to match the local domain height of approximately $y/d = 8.7$. The extrusion matched the cell spacing for each respective case. For the cylinder-interaction mesh in Figure 3.8, the same $y^+ = 1$ and $GR = 1.1$ was applied. Furthermore, the radial section extended $r/d = 3$ outboard and had non-dimensional wall-distance of $r^+ = 1$ with $GR = 1.2$ in the radial direction, and constant azimuthal spacing $\Delta\theta = 30$, as normalized by y^+. The total extent for the cylinder-interaction base mesh was from $x/d = -5$ to $x/d = 10.5$ and from $z/d = 0$ to $z/d = 5$, and the base domain contained a total of around 270 thousand cells. The full 3-D mesh with both the flat plate domain extruded along *z* and the cylinder-interaction domain extruded along *y* totaled approximately 19.8 million cells. At the interface between the two meshes, a zonal interface was generated to connect the cell faces with one another. This was implemented as a zonal boundary condition in CFD++. Additionally, the use of a symmetry plane is visible in Figure 3.8, which cut the cell count in half. The use of the symmetry plane was tested by only running the cylinder-interaction mesh both with and without symmetry, and it was verified that the symmetry plane was a valid assumption.

Simulations were performed with the CKE turbulence model. The reasons for this were two-fold: first, the CKE turbulence model contains a leading-edge transition model [33] that allows for a laminar section near the flat plate leading edge, thus providing a more

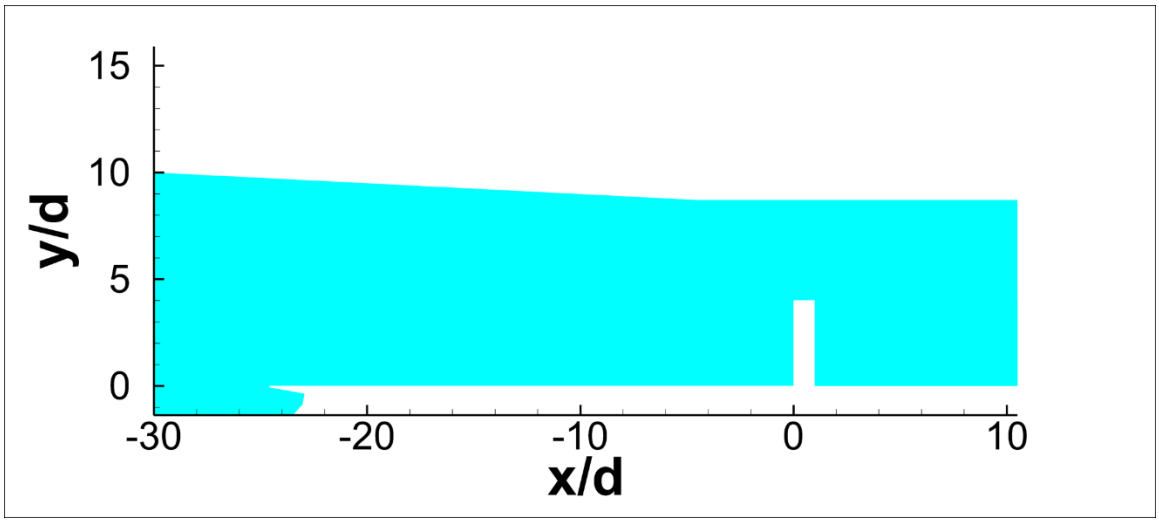


Figure 3.7. 3-D flat plate domain with cylinder, used to measure the extent of the interaction.

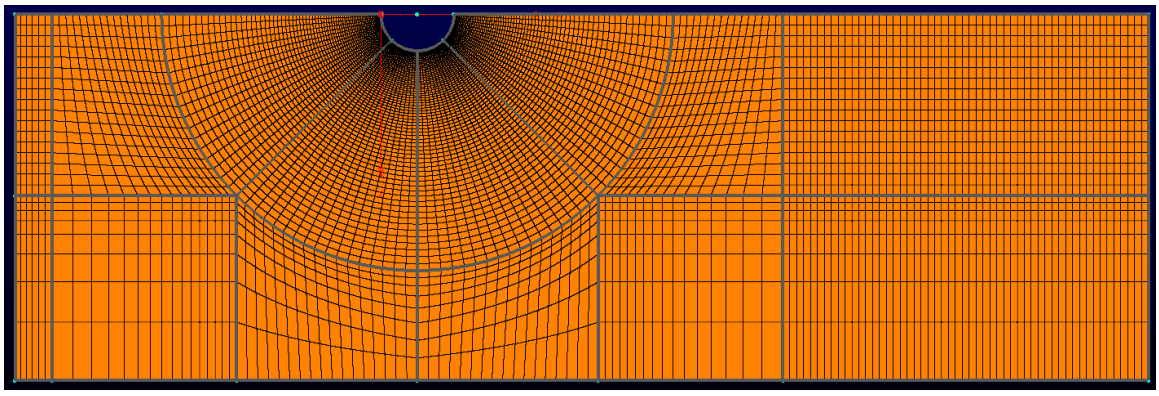


Figure 3.8. Base mesh of cylinder-interaction in *x*-*z*. Grey lines indicate domain zones, black lines show actual cells.

accurate representation of the boundary layer development; second, the Musker turbulent boundary layer profile requires turbulence inputs of k and ε [33, 41], and rather than converting turbulence values, it was convenient to directly implement these values from the CKE model solution. As for the initial conditions, a two-box method was implemented. The first box encompassed the entire domain space and used the primitive values from Table 3.1; the second box was formed in the wake of the cylinder and used the same primitive variables, except that $u_\infty = 1$ m s^{-1} in order to allow for the wake to develop by itself. A comparison between the 2-D and 3-D flat plate solutions yielded no significant differences along the centerline. The extent of the cylinder-interaction was measured, and initial upstream disturbances occurred around $x/d = -3$. As such, the radial extent of the base mesh in Figure 3.8 was deemed reasonable, as it fully encompassed the pressure onset of the interaction. This will be shown in a later section.

3.4.1.4 Inlet Profiles

A final comparison was done between freestream results from the PIV experiment of Combs et al. [7] and the 3-D flat plate with cylinder CFD result at $x/d = -19.5$, as summarized in Table 3.2. There was excellent agreement among all primitive variables, as they were within 1% of the experiment. Due to this agreement, the slice profiles at $x/d = -19.5$ and $x/d = -5$ were used as inlet profiles for the laminar and turbulent interactions, respectively. Note that PIV data from Combs et al. [7] does not exist at $x/d = -5$, so a direct comparison could not be made. Also note that the boundary layer height was not captured by PIV data, but was estimated in collaboration with Schlieren images by Lash et al. [6] around $\delta = 0.32$-0.48 mm ($0.1d$-$0.15d$). This is in good agreement with flat plate boundary layer theory by Schlichting [31]. As the numerical values fall within this range, the absolute value of the relative difference is assumed to be 0%. Since the PIV data considered the mean flow field, the CFD slices also averaged the freestream values from $y/d = 1$ to $y/d = 2$. Due to a non-zero pressure gradient being present on the flat plate, the primitive values still changed slightly, and this averaging was necessary; additionally, this explains the variation at the further downstream location of $x/d = -5$.

Table 3.2. Comparison between flat plate freestream conditions from CFD and PIV by Combs et al. [7] at $x/d = -19.5$, along with CFD data from $x/d = -5$.

	$x/d = -19.5$ **Experiment**	$x/d = -19.5$ **CFD**	**|Relative Difference|**	$x/d = -5$ **CFD**
P_∞ **[kPa]**	31.1	31.409	0.99%	31.837
T_∞ **[K]**	166.2	167.2	0.60%	168.0
u_∞ **[m s^{-1}]**	493	490.2	0.57%	488.5
M_∞ **[-]**	1.905	1.891	0.73%	1.880
δ **[mm]**	(0.32-0.48)	0.407	(0.00%)	1.15

3.4.2 Turbulent Interaction

Similar to the flat plate domain, the domain for the turbulent interaction was also progressively reduced. The first iteration used the same domain as the base mesh shown in Figure 3.8, where a box was considered with extents $x/d = -5$ to $x/d = 10.5$, $y/d = 0$ to $y/d = 10$, and $z/d = 0$ to $z/d = 10$. The second iteration decreased the height to $y/d = 5$ in order to reduce the cell count, and no significant differences were encountered in any of the parameters of interest. The third iteration decreased the height to $y/d = 4$, such that the upper boundary of the domain ended at the height of the cylinder. This method was also employed by Yamamoto and Takasu [15] and Hung and Buning [16], as it simplifies mesh generation. However, the scale of the interaction was decreased, as λ, and thus h_{tp}, were both smaller for this iteration, and so this iteration was invalid. The fourth iteration decreased the downstream extent to $x/d = 8$; again, no significant differences were encountered in any of the parameters of interest. It was ensured that the entirety of the subsonic region generated by the wake of the cylinder remained upstream of this outlet, and was found to extend downstream to about $x/d = 6$. A large set of results was gathered with the fourth iteration, where $x/d = -5$ to $x/d = 8$, $y/d = 0$ to $y/d = 5$, and $z/d = 0$ to $z/d = 5$, and is presented in Chapter 4. As will be discussed later, the semi-infinite consideration for these results was questionable for large δ/d, which led to a fifth domain being generated, where a cylinder of height $y/d = 10$ was simulated, and the upper boundary extended to the

height of the cylinder. Both the fourth and fifth iterations used the base mesh, as shown in Figure 3.9, and extruded this to their respective boundary heights. Similar to the mesh shown in Figure 3.8, this mesh contained only structured, hexahedral cells. The actual cells are not shown here because a grid independence study altered these for each iteration. The values used to generate each mesh iteration in the grid independence study are presented in Table 3.3. The values of Δy and Δr were held constant once the boundary layer growth reached the intended maximum value of Δy_{max} or Δr_{max}. This ensured that the grid did not become too coarse away from the wall. Other boundary conditions for this domain were similar to those for the flat plate domain. A Musker turbulent boundary layer profile [41] was implemented at the inlet with the freestream conditions from Table 3.2, including δ = 1.15 mm (0.3622d). A zero-gradient outflow was present at the outlet. The far-field for both the fourth and fifth iterations was once again a characteristics-based inflow/outflow, using the same freestream conditions as in Table 3.2, but only the fourth iteration used the far-field absorbing layers. Initial conditions were similar to the 3-D flat plate flow, where the same near-zero velocity box was established in the cylinder wake. Note that the cell count is lower for the cylinder with height y/d = 10, despite containing a larger domain. This is because a y^+ = 30 with GR = 1.2 was applied to the top of the cylinder with height y/d = 4, and thus required a higher cell count.

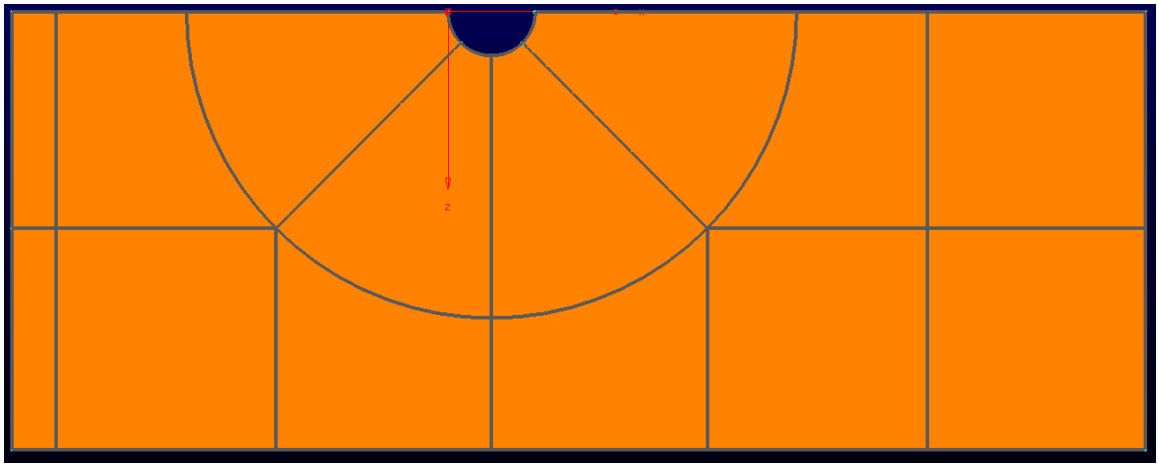


Figure 3.9. Base mesh for turbulent interactions in x-z. Grey lines indicate domain zones.

Table 3.3. Characteristics of the turbulent interaction grid independence study with cylinders of height $y/d = 4$ and $y/d = 10$.

	y^+	Δy_{max}	r^+	Δr_{max}	$\Delta\theta$	**Approximate Cell Count for height $y/d = 4$**	**Approximate Cell Count for height $y/d = 10$**
Coarse	2	800	2	800	200	190,000	160,000
Medium	1	400	1	400	100	910,000	700,000
Fine	0.5	200	0.5	200	50	5,670,000	3,790,000
Extra Fine	0.25	100	0.25	100	25	-	23,780,000

3.4.3 Laminar Interaction

As the extent of the laminar interaction is much larger, a domain similar to that of the turbulent interaction was used, but with additions. The extent of this domain was from $x/d = -19.5$ to $x/d = 15.5$, $y/d = 0$ to $y/d = 10$, and $z/d = 0$ to $z/d = 10$. Note that the cylinder of height $y/d = 10$ was used here as well, such that the upper boundary ended with the top of the cylinder. Furthermore, note that the cylinder was still located at $25d$ downstream of the flat plate leading edge. At $x/d = -19.5$, Lash et al. [6] and Combs et al. [7] reported a transitional boundary layer, as the boundary layer was tripped immediately downstream of the flat plate leading edge, and a laminar boundary layer did not develop. In order to simulate a laminar interaction here, a non-physical assumption had to be made: the freestream pressure was reduced to $P_\infty = 3110$ Pa, or one-tenth of the physical freestream pressure, in order establish a more traditionally laminar unit Reynolds number of approximately $Re_m = 2.83 \times 10^6$ m^{-1}, while all other primitive variables were maintained as the experimental values described in Table 3.2. Due to convergence issues with a fully laminar solution, the SA-QCR turbulence model was used to simulate the flow. In order to maintain as much laminar domain as possible, an inactive source-term region was implemented from $x/d = -19.5$ to $x/d = -13$. This disabled any modification to $\tilde{\nu}$ within that

region. It was verified that at stations downstream of this region, a laminar boundary layer still existed. Since CFD++ does not have an option for a laminar boundary layer inlet, a Blasius laminar boundary layer profile [42] was developed in MATLAB® R2015b with Prandtl number Pr = 0.744. This resulted in a velocity profile of height δ = 0.649 mm (0.2045d), and a temperature profile of height δ_{th} = 0.717 mm (0.2257d). Together with the remaining primitive variables, which were treated as constants, this Blasius profile was set at the inlet using a pressure-velocity-temperature-based 1-D inflow profile boundary condition. Note that a constant $\tilde{\nu} = \mu\ (8\rho)^{-1}$ was also set in the Blasius profile in order to establish a small, non-zero turbulence value that would maintain laminar conditions. Similar to the other simulations performed, a zero-gradient outflow was set at the outlet, and a characteristics-based inflow/outflow was defined at the far-field boundaries. As with the fifth iteration of the turbulent interaction, the far-field absorbing layers were not activated. Initial conditions were the same as before, where a two-box method was employed that initialized the cylinder wake to a near-zero velocity. A mesh indicating the extended domain zones is shown in Figure 3.10. A grid independence study similar to that performed for the turbulent interaction was also conducted, and its characteristics are outlined in Table 3.4. Note that the characteristics imposed on the laminar interaction meshes were the same as those for the turbulent interaction, and the only variation exists in the total cell count, thus enabling a direct comparison.

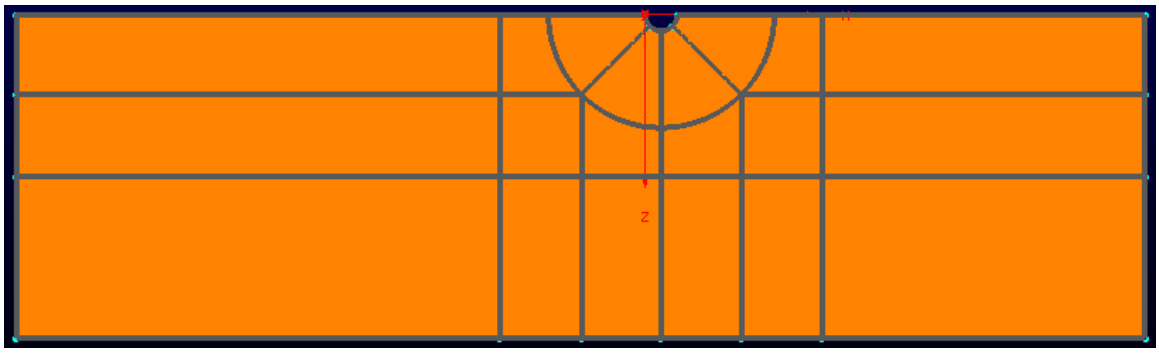


Figure 3.10. Base mesh for laminar interactions in x-z. Grey lines indicate domain zones.

Table 3.4. Characteristics of the laminar interaction grid independence study.

	y^+	Δy_{max}	r^+	Δr_{max}	$\Delta\theta$	***Approximate Cell Count***
Coarse	2	800	2	800	200	360,000
Medium	1	400	1	400	100	1,800,000
Fine	0.5	200	0.5	200	50	10,040,000
Extra Fine	0.25	100	0.25	100	25	64,140,000

CHAPTER 4
STEADY-STATE RESULTS & ANALYSIS

The results presented here were taken at the centerline plane of $z/d = 0$ and along the flat plate surface at $y/d = 0$. An initial convergence criterion of 10^{-5} for normalized residuals was set; however, due to the y-momentum term being consistently above this, the convergence criterion was relaxed to 10^{-4}. With this criterion in place, all laminar and turbulent interactions with a cylinder height of $y/d = 10$ converged, as did the coarse and medium mesh results for the turbulent interactions with a cylinder height of $y/d = 4$. The fine mesh result for the interaction with a cylinder height of $y/d = 4$ did not converge, and residuals failed to drop below 10^{-3} while continuously oscillating. The fine mesh solution indicated that the lambda shock structure moved upstream and downstream unpredictably over several iterations. As such, the fine mesh results were not reported. These oscillations were not encountered in the results with the cylinder of height $y/d = 10$, because time-step spatial smoothing had been activated for those runs, and this alleviated the problem.

4.1 Turbulent Interaction

The results for the turbulent cylinder-interaction with differing heights (and domains) are discussed separately below. A comparison between the 3 turbulence models was made first alongside a grid independence study. Specific parameters of interest were then used to determine whether or not a mesh was well-converged, and if the turbulence model provided an accurate representation of the flow. The empirical/theoretical target parameters for a turbulent interaction were used, and a comparison to experimental results from Lash et al. [6] was described. Recall that for a turbulent interaction, the separation length is approximately $\lambda/d = 2.65$ [11]. The separation length was determined numerically by analyzing the first cell off the flat plate surface and determining when reversed flow was present, i.e. $u < 0$ m s^{-1}. Using Equation (2-2), an empirical bow shock stand-off distance of $B/d = 0.77$ was calculated, which was determined in the post-processor by analyzing the streamwise extent of the sonic line in the bow shock region. Using Equation (2-1), a wave angle of $\varphi = 41.7°$ was calculated, and combined with λ/d and B/d, resulted in a triple point height $h_{tp}/d = 1.68$ using Equation (2-3).

4.1.1 Cylinder with Height y/d = 4

4.1.1.1 Grid Independence Study

As mentioned above, a grid independent solution was not achieved for the cylinder with height y/d = 4. Therefore, only the medium mesh results for this interaction are discussed, as they were representative of the geometry. Note that results for the cylinder of height y/d = 10 did converge, and were qualitatively similar to the results reported for the cylinder of height y/d = 4.

4.1.1.2 Turbulence Model Comparison

A result on the centerline plane with the CKE turbulence model is shown in Figure 4.1a and b, where Figure 4.1a shows the Mach number contours, including the black sonic line, and Figure 4.1b shows numerical Schlieren contours as the magnitude of the first derivative of density in the x-direction, representing an equivalent vertical knife edge. Note that the upper boundary of the domain appears unphysical; this is due to the far-field absorbing layer boundary conditions, where the inviscid bow shock and the expansion waves generated by the top of the cylinder were damped out in the last 3 cells to the freestream values. The subsonic portion of the cylinder wake, as seen in Figure 4.1a, was longest at the centerline, and this subsonic extent was captured in all simulations.

A comparison between the three turbulence models is shown in Figure 4.2a-f, where Figure 4.2a-c shows Mach number contours and Figure 4.2d-f shows numerical Schlieren contours of the CKE, SST, and SA-QCR turbulence models, respectively. Note that Figure 4.2a- c uses the same contour levels as those in Figure 4.1a, and Figure 4.2d-f uses the same contour levels as those in Figure 4.1b. The sonic line is shown as the pink solid line within the Mach number contours, and as the orange solid line within the numerical Schlieren contours. The empirical values for B and h_{tp} were superimposed in black and pink dashed lines between the Mach number and numerical Schlieren contours, respectively. Qualitatively, all structures of the lambda shock are visible. Flow separation induces bifurcation of the inviscid shock into the forward and trailing shock. There is good qualitative agreement between the CKE and SA-QCR turbulence model results and the empirical values of B/d and h_{tp}/d, as well as the separation length. For the SST turbulence

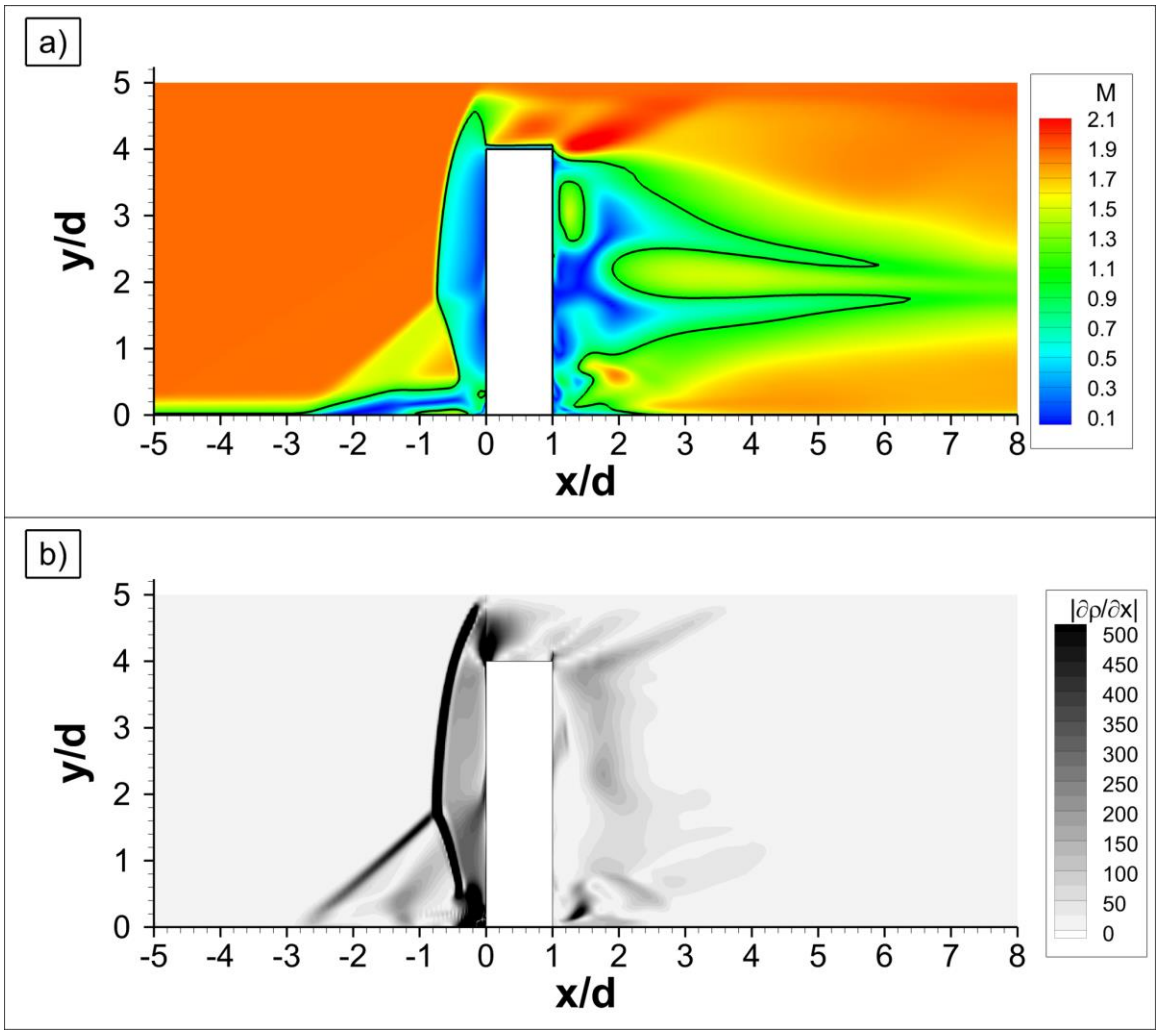


Figure 4.1. a) Mach number and b) numerical Schlieren contours of medium mesh result with cylinder of height y/d = 4 with CKE turbulence model at z/d = 0. Black line in a) is sonic line.

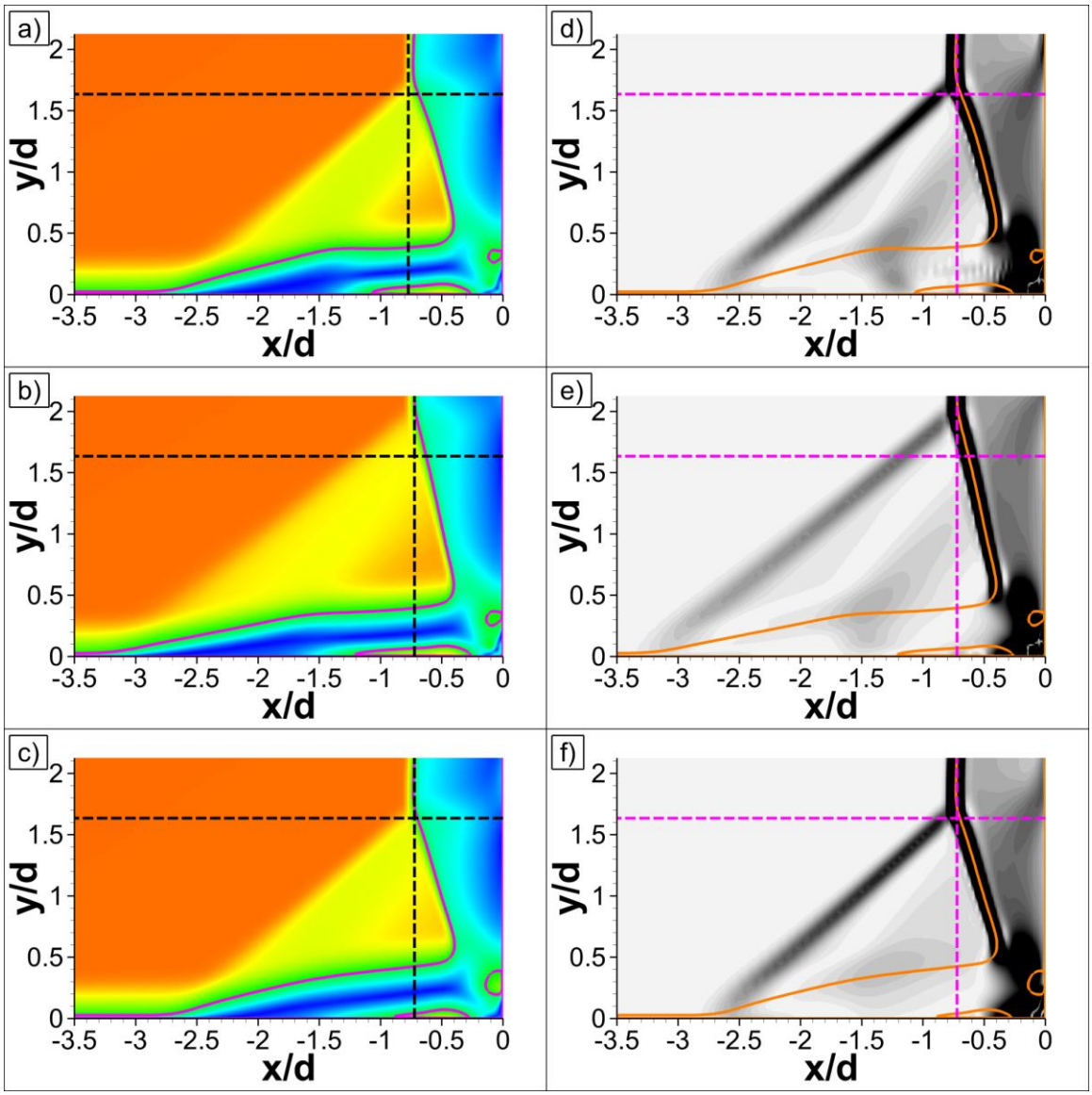


Figure 4.2. Medium mesh results for cylinder of height y/d = 4. a) - c) Mach number contours for CKE, SST, and SA-QCR turbulence models, respectively, where pink line represents sonic line, black lines represent empirical values for B and h_{tp}. d) - f) Numerical Schlieren contours for CKE, SST, and SA-QCR turbulence models, respectively, where orange line represents sonic line, pink lines represent empirical values for B and h_{tp}.

model result, the bow shock stand-off distance appears to have been calculated accurately. However, flow separation occurred too far upstream, and thus induced a higher triple point. Note that a supersonic jet downstream of the triple point, as described by many in literature [13, 15, 16, 19, 21, 23, 29], was not present for any turbulence model result. There was, however, a supersonic region located on the cylinder wall at around y/d = 0.3, directly downstream of the trailing shock foot for all turbulence model results. The size of this varied with the choice of turbulence model, but did not appear to impact the size of the supersonic region in the separation bubble. The SA-QCR turbulence model generated the largest supersonic region at the cylinder wall and also the smallest supersonic region in the separation bubble; however, the results from the SST turbulence model seem to invalidate a correlation. The results with the SST turbulence model indicated a smaller supersonic region at the cylinder wall than those for the SA-QCR turbulence model, but also the largest supersonic region in the separation bubble. Both the CKE and SST turbulence model results reached a plateau for the height of the separation bubble, where an expansion fan was induced. This expansion fan impinged upon the trailing shock and added curvature to the shape of the shock. This fan was not visible in the SA-QCR turbulence model result. It can also be seen that the separation bubble for all turbulence model results intersected with the trailing shock; it appears that the trailing shock foot is located at this intersection.

A quantitative analysis of the results is presented in Table 4.1, where the parameters of interest were directly compared to the empirical values [11]. Note that the spatial accuracy of the CFD values was ±1.7% for λ/d, ±2.4% for B/d, and ±1.6% for h_{tp}/d, assuming that the finite volume solution can be determined accurately across half a cell size. From this comparison, it can be seen that the CKE and SA-QCR turbulence models were in good agreement with empirical values, since the absolute values of their relative differences were within 10%. The results from the SST turbulence model, however, indicated a large difference in both separation length and triple point height, exceeding 15% in both instances. The SST turbulence model is known to predict early boundary layer separation, despite being a recommended turbulence model for SWBLIs [43-45]. However, based on the information gathered, the SST turbulence model does not appear suitable for this type of flow.

Table 4.1. Comparison of parameters of interest between empirical values [11] and medium mesh results for all turbulence models with cylinder of height y/d = 4.

		CKE		**SST**		**SA-QCR**	
	Empirical Value	**CFD Value**	**|Relative Difference|**	**CFD Value**	**|Relative Difference|**	**CFD Value**	**|Relative Difference|**
$\boldsymbol{\lambda/d}$	2.65	2.64	0.4%	3.06	15.5%	2.55	3.8%
$\boldsymbol{B/d}$	0.77	0.74	3.9%	0.72	6.5%	0.73	5.2%
$\boldsymbol{h_{tp}/d}$	1.68	1.72	2.4%	1.99	18.5%	1.63	3.0%

A comparison with the CKE turbulence model results and in-house experimental work of Lash et al. [6] and Combs et al. [7] indicated further discrepancy than the empirical values [11]. The mean location of the separation length from Schlieren data from Figure 2.5 was λ/d = 2.15 [6], and from PIV data was λ/d = 2.79 [7]. Taking these values and comparing them with the empirical value of λ/d = 2.65 [11] yields an absolute relative difference of 23.3% for Schlieren results and 5.3% for PIV results. Note that the Schlieren results had a lower standard deviation of σ/d = 0.1 [6], as opposed to the higher standard deviation of σ/d = 1.68 obtained from the PIV data [7]. As it stands, the SA-QCR turbulence model generated results closer to the experimental data, but the results with the CKE turbulence model were better aligned with the empirical values. However, the experimental data are still consistent with results from literature [23, 46].

Further qualitative and quantitative analyses were performed by analyzing the streamlines in the centerline plane using only u and v. These are shown for all of the turbulence models in Figure 4.3a-f. Note that the Mach number contour levels are again the same as in Figure 4.1a. A single, large, primary vortex was visible in the separation bubble for all results, with characteristics similar to those reported by Hung and Buning [16]. These results differ, however, from those obtained by Yamamoto and Takasu [15], where the separation bubble contained two co-rotating vortices. The choice of scheme may factor in here, as Hung and Buning [16], similar to this study, generated a steady-state solution, and Yamamoto and Takasu [15] generated a time-accurate solution.

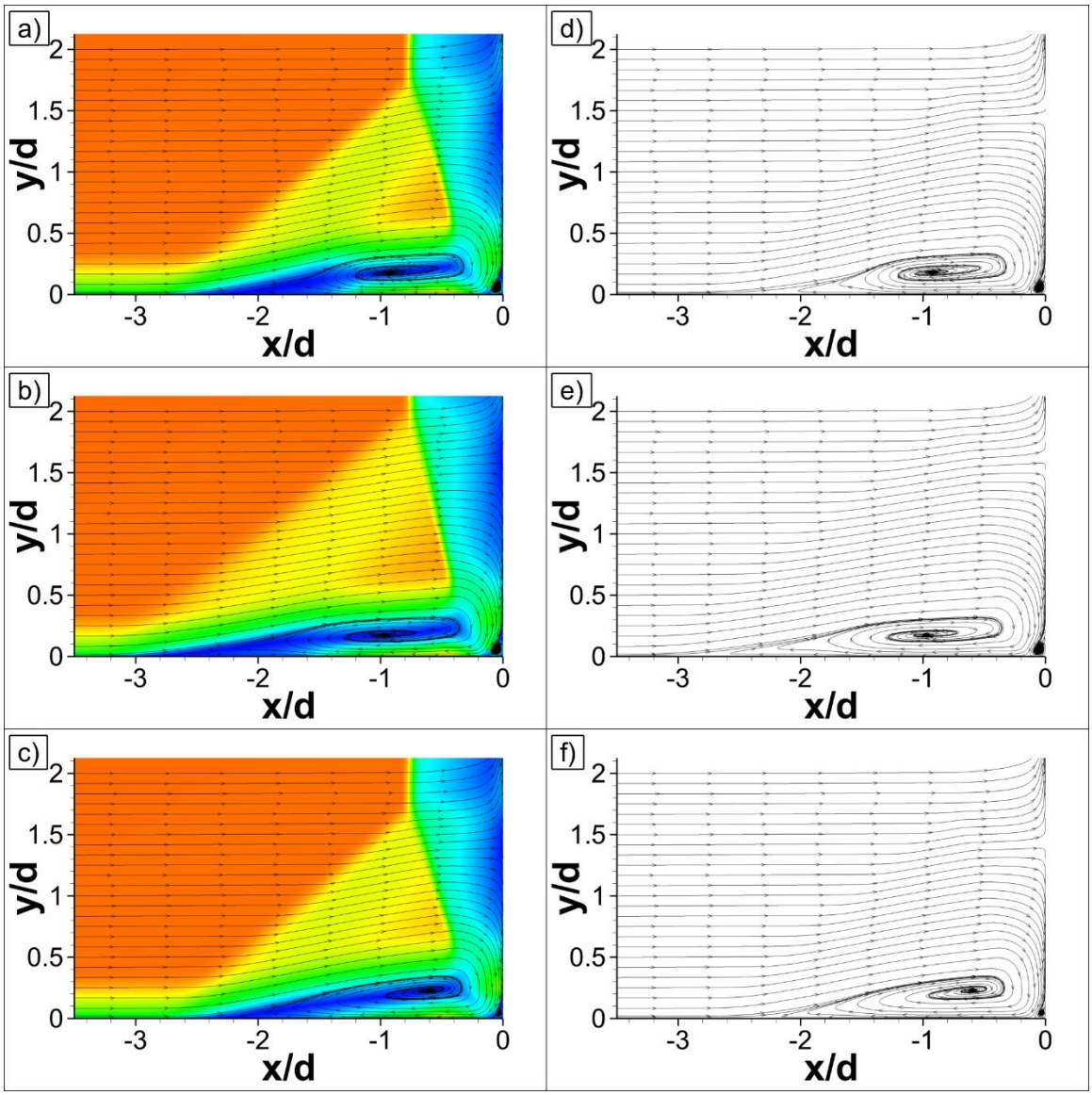


Figure 4.3. Streamlines on medium mesh results for cylinder of height *y/d* = 4. a) - c) With and d) - f) without Mach number contours, for CKE, SST, and SA-QCR turbulence models, respectively.

An initial study that was performed, which is not presented here, used hybrid RANS/LES to model the problem using the fine mesh [47]. In the hybrid RANS/LES results, a number of co-rotating primary vortices, varying between 3 and 6, were observed in the separation bubble. Therefore, the occurrence of only a single large vortex may be an artifact of Reynolds-averaging, and the presence of multiple co-rotating vortices may be more physical, but this requires future investigation.

A closer look at the streamlines near the corner region around $x/d = 0$ and $y/d = 0$ is shown in Figure 4.4a-c. The Mach number contours have been altered here to view the subsonic portion of the flow. Despite the red contour level in Figure 4.4b, the flow remained entirely subsonic. A secondary and tertiary vortex are visible here. For the CKE and SST turbulence model results, a quaternary vortex, which was contained within $0.002d$ in both the streamwise and transverse directions, was present directly at the corner. For the SA-QCR turbulence model, this quaternary vortex was not present. Due to its extremely small size, on the order of μm, this quaternary vortex is not further discussed. The secondary vortex was formed in a similar manner as shown in Figure 2.7, where *SL1* corresponds to the half-saddle, and *F4* corresponds to the node. At the flat plate surface, the primary and secondary vortex diverged, at what corresponds to the half-saddle *AL1* in Figure 2.7. This impingement upon the flat plate surface induced a stagnation point, which is likely a source of high pressure.

4.1.1.3 Surface Pressure Analysis

Two important characteristics of the flow field are the pressure rise just upstream of separation and the pressure on the flat plate surface directly underneath the separation bubble. The flat plate surface pressure ratio is shown in Figure 4.5. The interaction exhibited the classical shape of an initial rise, plateau, drop, and final rise characteristic of other interactions reported in the literature [12-16]. Differences in the location of the initial pressure rise were directly proportional to the flow separation length: the further upstream the initial pressure rise occurred, the further upstream the separation point was. This was evident in the fact that the result with the SST turbulence model, which over-predicted separation compared to both the empirical values and the results of the other turbulence

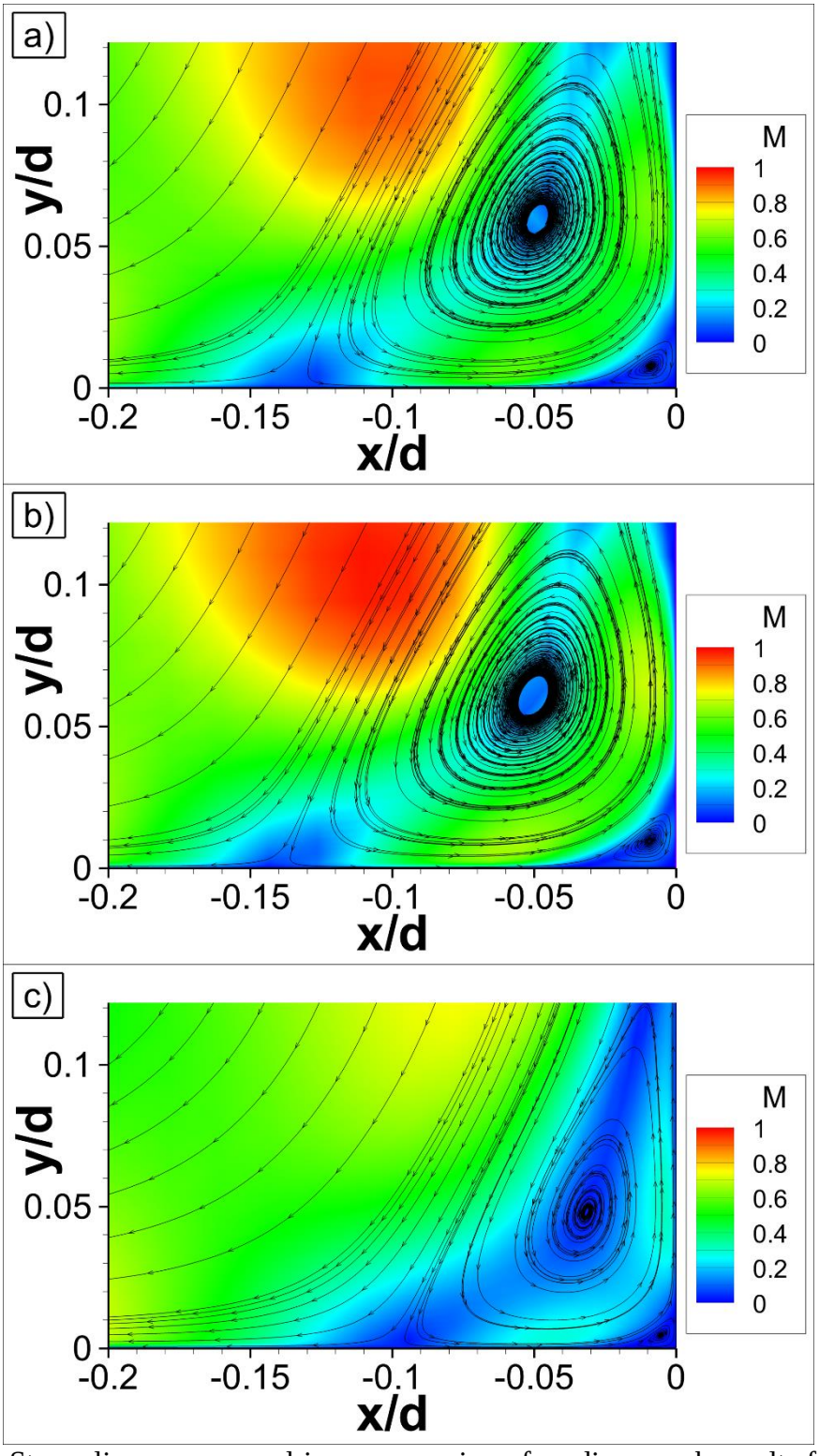


Figure 4.4. Streamlines on zoomed-in corner region of medium mesh results for cylinder of height y/d = 4. a) - c) Mach number contours for CKE, SST, and SA-QCR turbulence models, respectively.

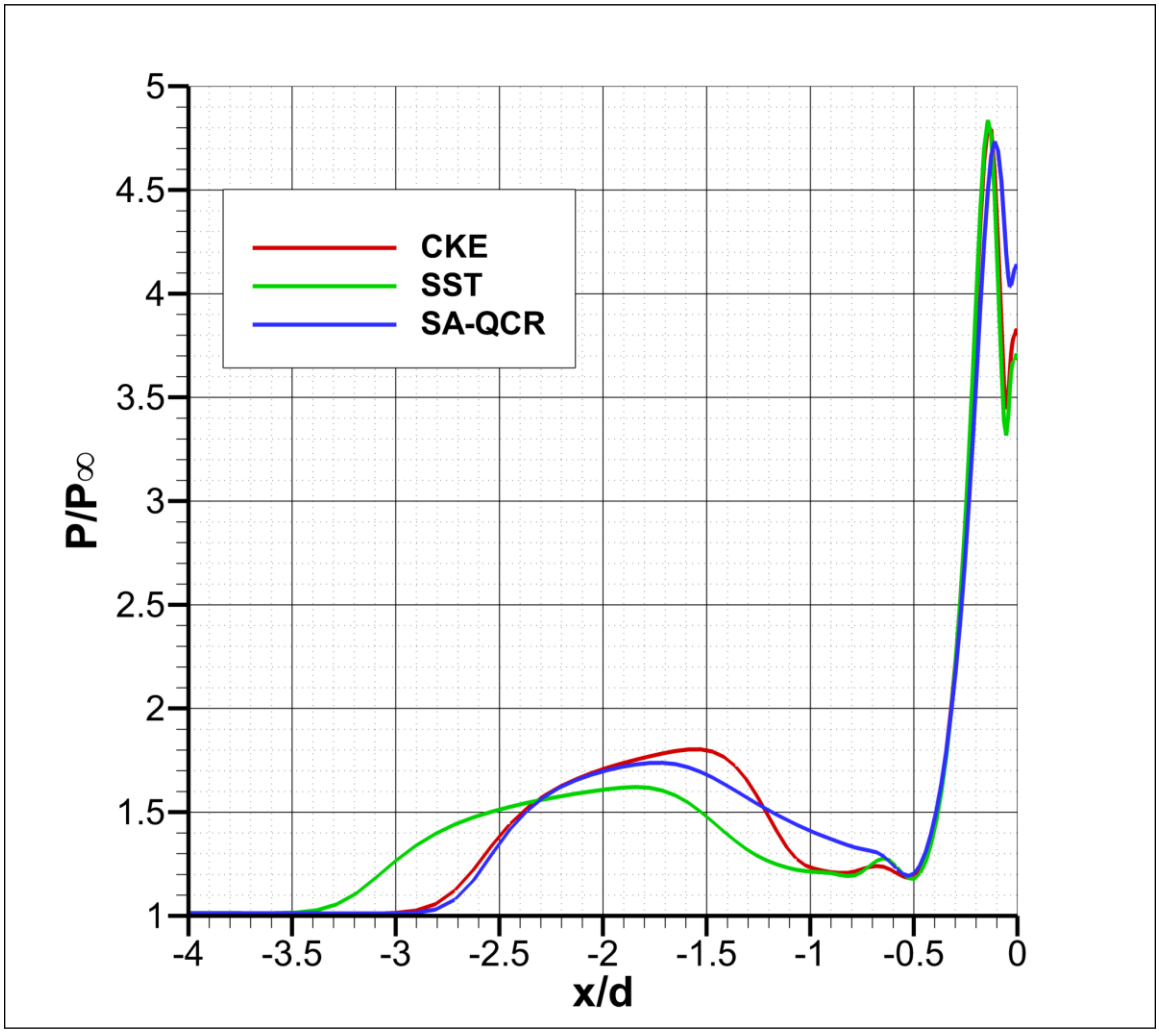


Figure 4.5. Medium mesh results with indicated turbulence models, showing normalized pressure on the flat plate surface, upstream of the cylinder with height *y/d* = 4.

models, had an initial pressure rise well upstream of the results with the other turbulence models. This early separation with the SST turbulence model result also affected the pressure plateau, which was lower than that for the other turbulence model results. Comparing the CKE and SA-QCR turbulence model results, they were relatively consistent for the initial pressure rise and plateau. However, in the region directly underneath the node of the primary vortex, the CKE turbulence model result experienced a sharp drop, whereas this drop was more gradual with the SA-QCR turbulence model result. Around $x/d = -0.5$, a trough with $P/P_\infty > 1$ was experienced for all turbulence model results, followed by the final rise in pressure that led to the peak pressure. This was then followed by a small drop in pressure directly at the cylinder leading edge. Determining the peak pressure magnitude and location on the flat plate surface is a key factor in the design of high-speed systems, as it drives the structural requirements. While experimental work is unable to resolve the near-cylinder-wall region in the way that a computation could, both experimental and computational work in literature has agreed upon the pressure peak being located near the cylinder leading edge [12-14, 15, 16, 19], and this is further visible in the blunt-fin-interaction results of both Hung and Buning [16] and Dolling and Bogdonoff [19] in Figure 2.6a. A peak pressure of $P/P_\infty \approx 4.8$ was calculated for all turbulence model results. Hung and Buning [16] reported a peak pressure of $P/P_\infty \approx 6$ at $M_\infty = 2.95$, and Yamamoto and Takasu [15] reported a peak pressure of $P/P_\infty \approx 19$ at $M_\infty = 3.92$. The plateau and peak pressure values were lower than other computational [15, 16] and experimental [12, 14, 19] results in literature, but that may simply be due to the lower freestream Mach number. Additionally, Dolling and Bogdonoff [12] described a weak dependence on δ/d on the scale of the interaction, which may further factor into the lower pressure ratio.

4.1.1.4 Effect of Incoming Boundary Layer Height

As a result of this dependence, a study was performed where the incoming boundary layer height δ/d was varied, but all other constraints were maintained constant. As such, the only variation was in the formulation of the Musker turbulent boundary layer profile [41] as an inlet condition, where a different boundary layer height was input. The variation was from $\delta/d = 0.25$ to $\delta/d = 2.50$ in increments of 0.25. Only the CKE turbulence model was used here since it provided the most accurate results compared to empirical values.

The results from above with δ/d = 0.3622 were not included in the discussion below in order to provide an assessment using a constant incremental value. Numerical Schlieren contours with contour levels similar to those in Figure 4.2d-f are shown in Figure 4.6a-j, where Figure 4.6a represents δ/d = 0.25, each successive letter represents an increment by 0.25 from the previous letter, and the final value of δ/d = 2.50 is shown in Figure 4.6j. From a qualitative perspective, as δ was increased, so was the scale of the lambda shock structure. The forward shock shifted further upstream as δ/d was increased, and as a result, h_{tp} shifted upwards. Note that for the case of δ/d = 1.25, $h/h_{tp} < 2$, and so the semi-infinite height consideration [12], where $h/h_{tp} >$ 2-3, was no longer valid. Results with the cylinder of height y/d = 10 ensured that this issue was mitigated. The strength of the interaction seemed to have decreased with increasing δ, as the near-wall supersonic regions, indicated by the orange sonic line, continuously decreased in size and eventually were no longer present. This may have been due to the larger separation bubble, where the flow was not as compressed, thus allowing for lower-velocity expansions. Furthermore, the decreasing strength of the interaction as δ was increased was visible in the greater dissipation and curvature of the forward shock, as well as in the straightening of the trailing shock. It appears as though the trailing shock tended towards a normal shock for the highest δ/d, which was where h_{tp} was fully submersed within the boundary layer. A correlation still existed between the trailing shock foot and separation bubble height as δ was increased; however, as $\delta/d \geq 1.25$, the highest point in the separation bubble was no longer at the trailing shock foot.

A quantitative analysis of the parameters of interest is shown in Figure 4.7a-c, where the parameters were compared to the empirical values [11], including a ±10% error threshold. It can be seen in Figure 4.7b that B was nearly constant for any given value of δ. From Figure 4.7a it can be seen that λ did begin to increase as δ was increased; however, λ decreased for $\delta/d \geq 1.25$, which was contrary to what was observed in the numerical Schlieren contours from Figure 4.6e-j. This discrepancy factored into the calculation of h_{tp}, and therefore, Figure 4.7c includes both the values that were calculated using Equation (2-3), as well as those obtained via visual inspection of the numerical Schlieren contours.

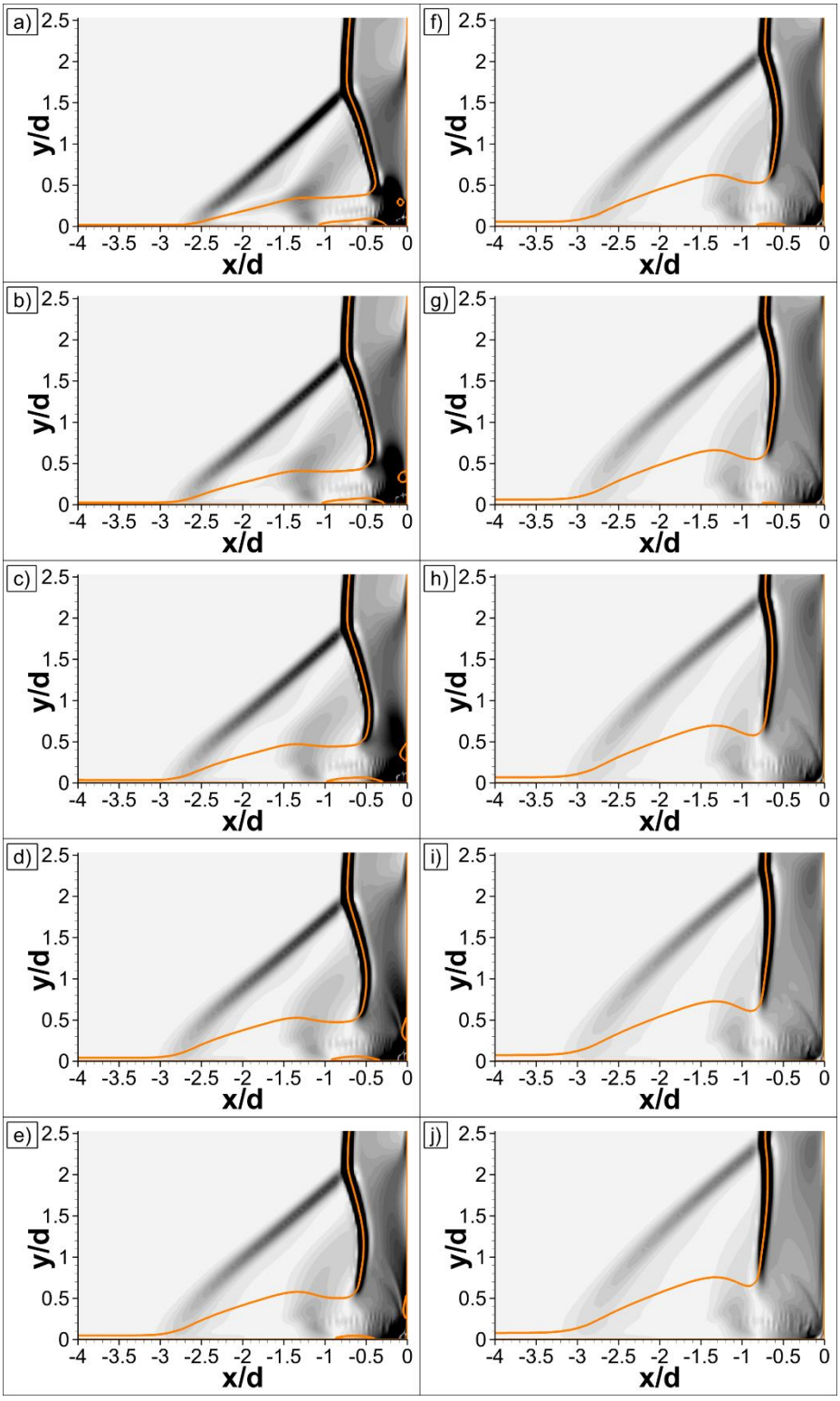


Figure 4.6. Medium mesh results with varied incoming boundary layer height δ/d for cylinder with height y/d = 4. a) - j) δ/d = 0.25 to δ/d = 2.50 with constant increment of 0.25. Orange line represents sonic line.

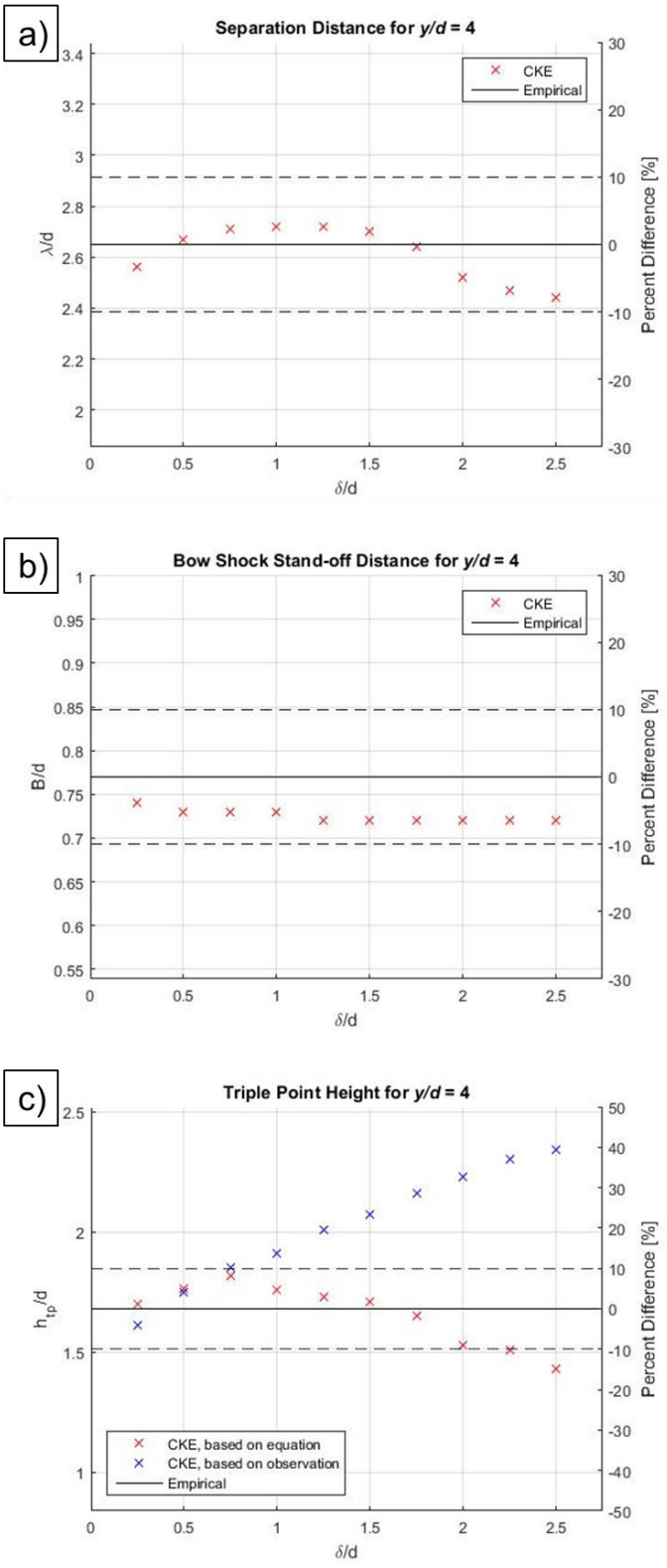


Figure 4.7. Comparison of parameters of interest between empirical values [11] and medium mesh results for varied δ/d with cylinder of height $y/d = 4$. a) λ/d, b) B/d, c) h_{tp}/d.

The visual inspection indicates an expected trend, where h_{tp} linearly increased as δ was increased. It can also be seen here that for $\delta/d \geq 1.25$, $h_{tp}/h < 2$, and the semi-infinite height consideration was no longer valid. This contributed to the decision to perform simulations with a cylinder of height $y/d = 10$.

For completeness, the pressure ratio on the flat plate surface is shown in Figure 4.8. The initial pressure rise that is known to induce flow separation consistently shifted further upstream with an increase in δ. This agrees well with the observations from numerical Schlieren contours in Figure 4.6a-j. Strangely, the actual separation length did not also increase for the values where $\delta/d \geq 1.25$, as shown in Figure 4.7a. In correlation with the upstream shift in the initial pressure rise, the magnitude of the pressure plateau region was reduced. In all cases, the pressure trough following the pressure plateau region gathered at around $x/d = -0.8$, which approximately coincided with the center of the supersonic region in the separation bubble. The peak pressure location for all cases was at the stagnation point where the primary and secondary vortices split, at an equivalent of *AL1* in Figure 2.7. The peak pressure magnitude decreased with increasing δ, which is a promising observation. Further study with a true semi-infinite cylinder is necessary to verify this observation, and so the cylinder with height $y/d = 10$ underwent a similar analysis.

Apart from the pressure ratio on the flat plate surface, the pressure ratio on the cylinder leading edge was also analyzed, as shown in Figure 4.9. The trend agrees well with both Westkaemper [11] and Hung and Buning [16]. First, an initial pressure decrease was observed along the height of the cylinder. This generated a trough pressure, followed by a pressure rise in a shear region that was induced by the primary vortex, until a peak pressure was observed. This was followed by a pressure decrease until the inviscid region, where $P/P_{0,2} = 1$ remained constant. As δ was increased, the magnitudes of both the trough and peak pressure decreased, similar to what Hung and Buning [16] reported. The peak pressure location here correlated well with the observed triple point height, as indicated by Figure 4.7c, and the differences between the two were consistently within 15%. The trough pressure location did not appear to have a similar correlation with any parameter of interest; however, this location was just upwards of the separation line of the secondary vortex,

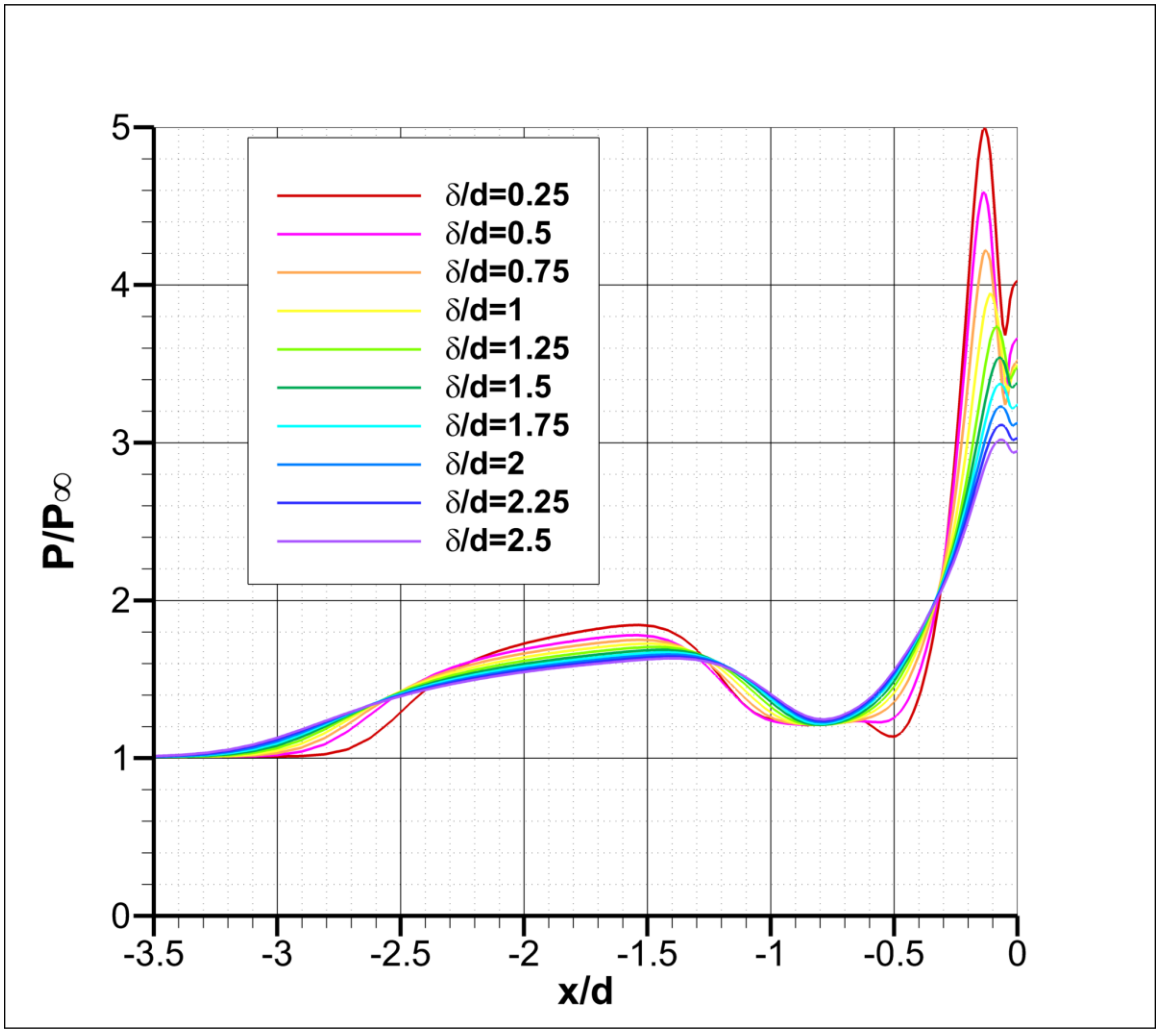


Figure 4.8. Medium mesh results with varied *δ/d*, showing normalized pressure on the flat plate surface, upstream of the cylinder with height *y/d* = 4.

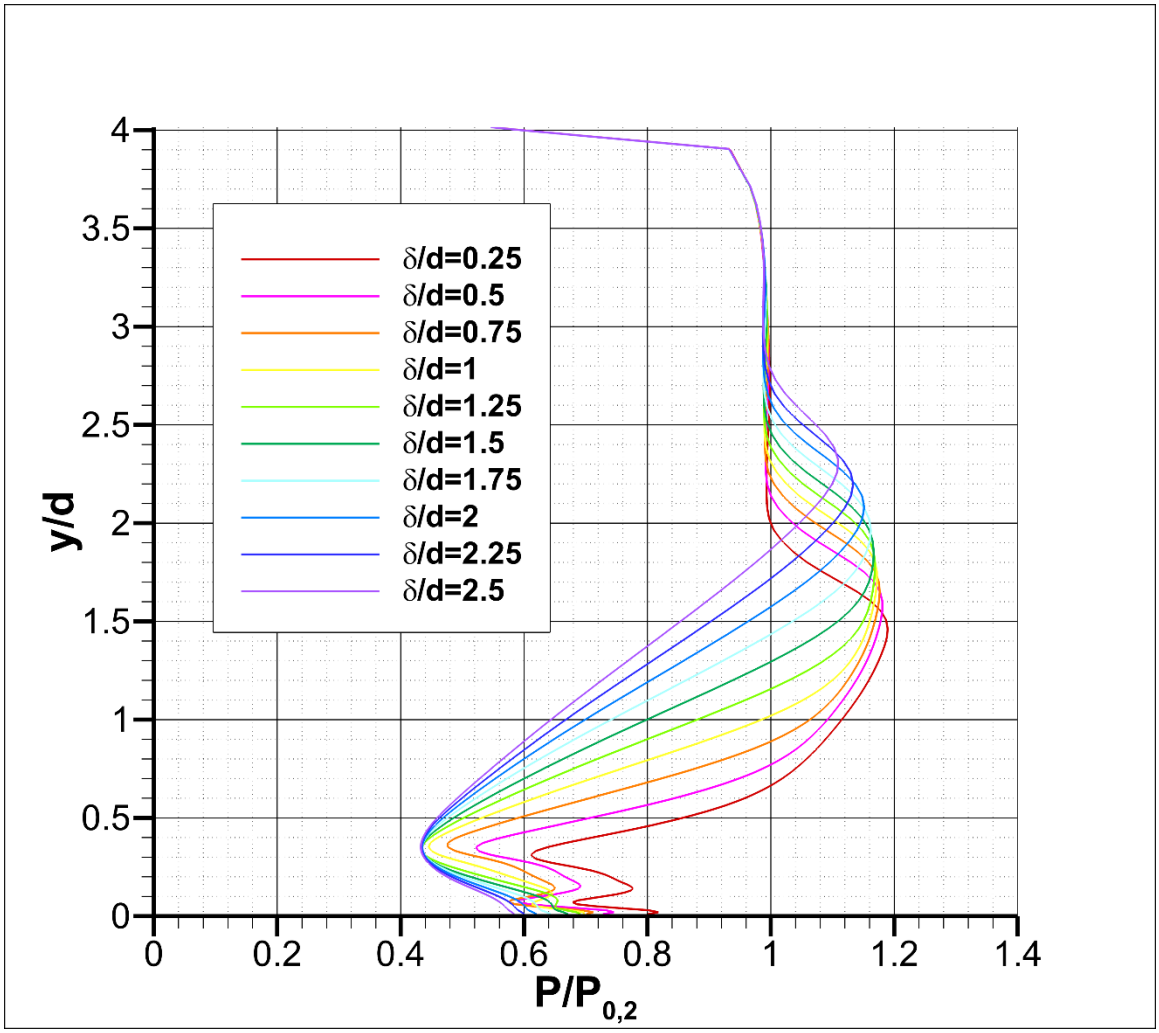


Figure 4.9. Medium mesh results with varied δ/d, showing normalized pressure on the cylinder leading edge of the cylinder with height y/d = 4.

corresponding to *SL1* in Figure 2.7. Furthermore, the trough pressure appeared to have settled to a minimum magnitude around $P/P_{0,2} \approx 0.43$ and location around $y/d \approx 0.35$. The pressure fluctuations downwards of this trough pressure were only observed for low δ/d. These straightened out for the cases where $\delta/d \geq 1.25$, so further investigation was required before drawing any conclusions.

4.1.2 Cylinder with Height y/d = 10

4.1.2.1 Grid Independence Study

As previously discussed, the results generated with a cylinder of height $y/d = 4$, although considered semi-infinite for the experimental conditions, could not be considered semi-infinite for large δ/d. Therefore, an analysis with a cylinder of height $y/d = 10$ was also performed. Furthermore, as this analysis was performed, increased insight into the requirements for simulations of this type of interaction allowed for a better numerical formulation, and thus convergence. In particular, the activation of time-step spatial-smoothing and the decrease of the temporal smoothing (under-relaxation) parameter from 0.75 to 0.5 significantly improved stability and convergence. As such, the grid independence study, outlined in Table 3.3, could be completed successfully, and results are shown in Figure 4.10a-c. It can be seen that B in Figure 4.10b was nearly constant for all turbulence models at all mesh sizes. Figure 4.10a shows that λ was nearly identical between the fine and extra fine meshes for all turbulence models, and similarly, h_{tp} was very similar between the fine and extra fine meshes. A small discrepancy exists here because of measurement error from the forward shock angle. However, as previously mentioned, h_{tp} was not as accurately determined as λ or B, and the consistency observed with the other parameters for the fine and extra fine meshes led to the conclusion that the fine mesh sufficed. Therefore, all successive simulations were performed with the fine mesh.

4.1.2.2 Turbulence Model Comparison

The entire domain with the SA-QCR turbulence model is shown in Figure 4.11a and b, where, similar to Figure 4.1a and b, Figure 4.11a shows the Mach number contours, and Figure 4.11b shows numerical Schlieren contours. For this, and the other simulations

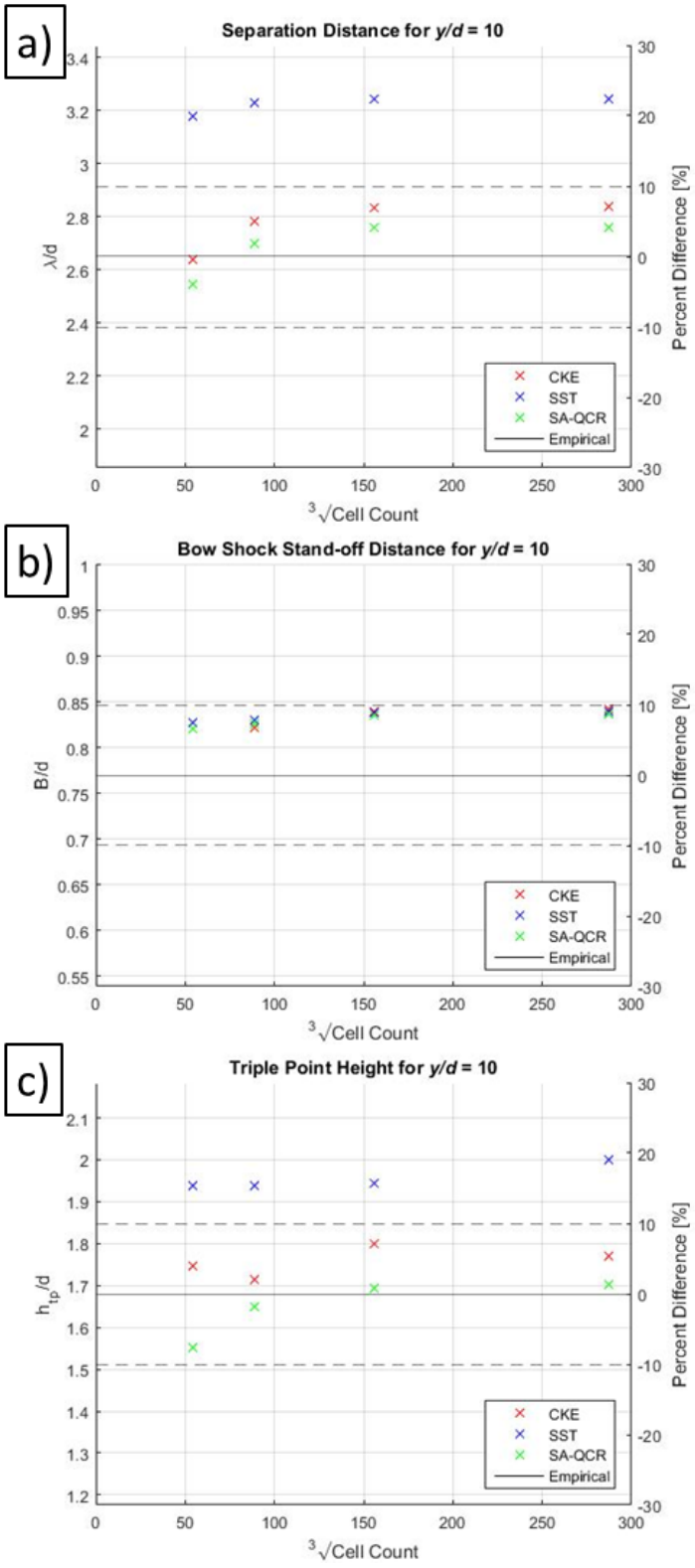


Figure 4.10. Grid independence study comparing the parameters of interest for various turbulence models with cylinder of height y/d = 10. a) λ/d, b) B/d, c) h_{tp}/d.

performed with the cylinder of height y/d = 10, the far-field absorbing layers were not active, as they did not impact the flow field. As a result, there was some shear stress at the upper boundary causing an extended wake. However, the area of interest was still near the flat plate surface, and this error was therefore not a concern. As before with the cylinder of height y/d = 4, the entire subsonic extent of the wake was captured.

A comparison between the three turbulence models, similar to that presented in Figure 4.2a-f, is shown in Figure 4.12a-f, again in the order of CKE, SST, and SA-QCR turbulence models, respectively. Figure 4.12a-c shows the Mach number contours and Figure 4.12d-f shows the numerical Schlieren contours. The sonic line is shown as the pink solid line in the Mach number contours, and as the orange solid line in the numerical Schlieren contours. Again, the empirical values for B and h_{tp} are superimposed in the black and pink dashed lines for the Mach number and numerical Schlieren contours, respectively.

Qualitatively, the results were very similar to those observed for the cylinder with height y/d = 4. There is, again, good agreement between the CKE and SA-QCR turbulence model results and the empirical values, although the bow shock was simulated further upstream than for the cases with the cylinder of height y/d = 4. The results with the SST turbulence model again seemed to have properly simulated the bow shock stand-off distance, but over-predicted the separation length, and therefore produced a higher triple point. The supersonic jet downstream of the triple point was again not visible for any of the turbulence model results. Instead, the supersonic region directly at the cylinder wall and downstream of the trailing shock foot was again present, and its size varied depending on the turbulence model selected. The largest extent of this was seen for the SA-QCR turbulence model in Figure 4.12c and f. Furthermore, the smallest supersonic region within the separation bubble at the flat plate surface was also observed with the SA-QCR turbulence model. However, a correlation still did not exist, as the results with the SST turbulence model indicated supersonic regions that were both larger in size than those for the results with the CKE turbulence model. Similar to the results with a cylinder of height y/d = 4, the results with the CKE and SST turbulence models reached a plateau for the height of the separation bubble that induced a Prandtl-Meyer expansion fan. A very weak expansion fan was visible for the results with the SA-QCR turbulence model.

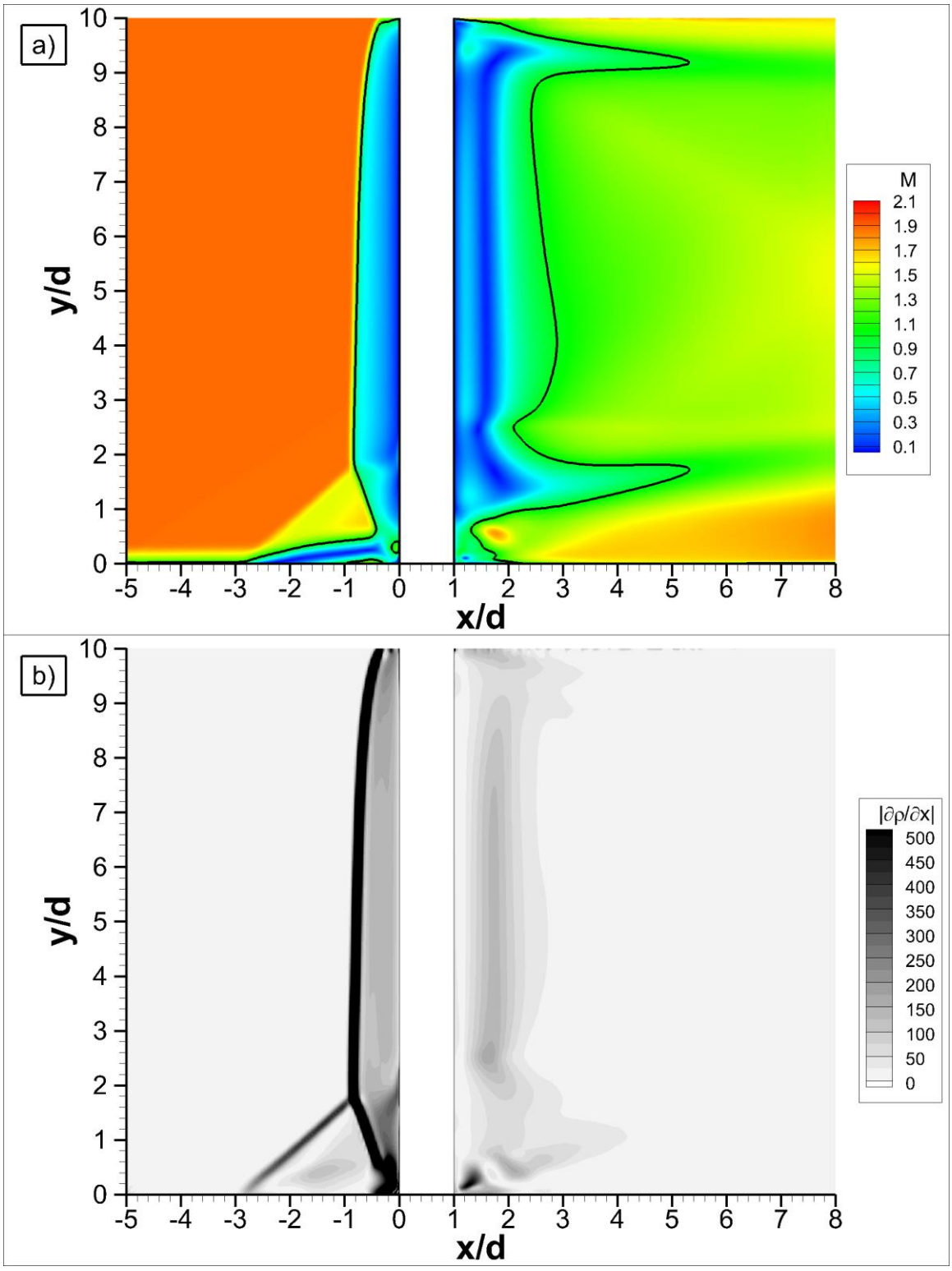


Figure 4.11. a) Mach number and b) numerical Schlieren contours of fine mesh result with cylinder of height *y/d* = 10 with SA-QCR turbulence model at *z/d* = 0. Black line in a) is sonic line.

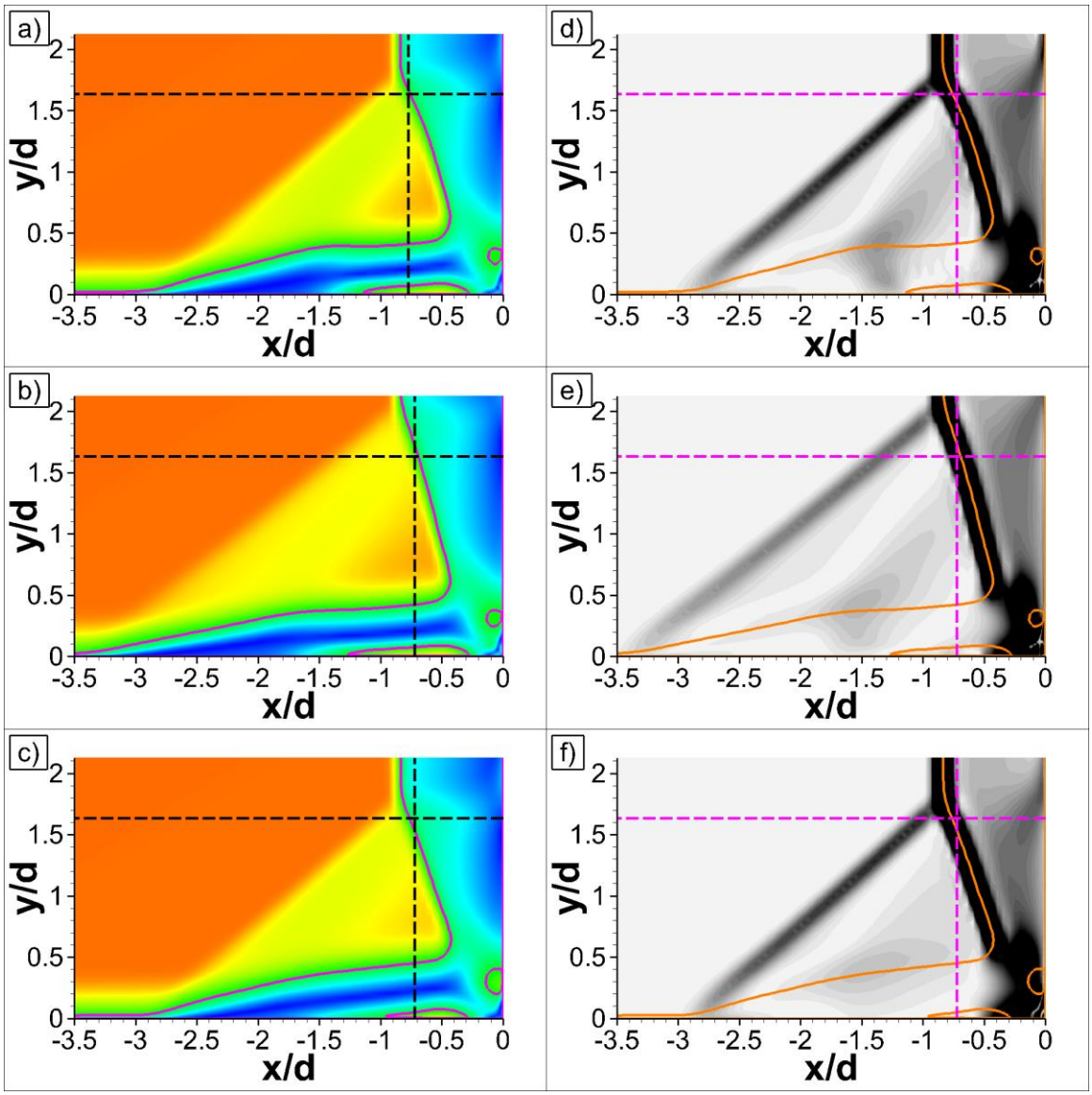


Figure 4.12. Fine mesh results for cylinder of height y/d = 10. a) - c) Mach number contours for CKE, SST, and SA-QCR turbulence models, respectively, where pink line represents sonic line, black lines represent empirical values for B and h_{tp}. d) - f) Numerical Schlieren contours for CKE, SST, and SA-QCR turbulence models, respectively, where orange line represents sonic line, pink lines represent empirical values for B and h_{tp}.

A quantitative analysis of the results is presented visually through the grid independence study in Figure 4.10a-c and numerically in Table 4.2. In all cases, *B/d* was calculated to be in the same location, although this was upstream of the expected value. Compared with the results from Table 4.1 for the cylinder with height $y/d = 4$, it can be seen that λ had shifted upstream and, as a result, h_{tp} shifted upwards for the CKE and SA-QCR turbulence model results. The SA-QCR turbulence model results were now in better agreement with the empirical values than the CKE turbulence model results were. The absolute relative difference of the empirical values and the SST turbulence model results for λ/d and h_{tp}/d still exceeded 15% in both instances. Based on these results and those with a cylinder of height $y/d = 4$, the SST turbulence model is not recommended for this type of flow, as flow separation is induced too far upstream.

A comparison with the in-house experimental work of Lash et al. [6] and Combs et al. [7] yielded a greater error than for the results with a cylinder of height $y/d = 4$ when compared to Schlieren data, but less error when compared to PIV data. The SA-QCR turbulence model results generated the closest values to the empirical values [11], with an absolute relative difference in 4.2% for λ/d. The absolute relative difference to the mean location from Schlieren data, with $\lambda/d = 2.15$ [6], was 29.8%; however, the absolute relative difference to the PIV data, with $\lambda/d = 2.79$ [7], was only 1.1%. In both cases the SA-QCR turbulence model results were greater in magnitude, and based on the results in

Table 4.2. Comparison of parameters of interest between empirical values [11] and fine mesh results for all turbulence models with cylinder of height $y/d = 10$.

		CKE		**SST**		**SA-QCR**	
	Empirical Value	**CFD Value**	**|Relative Difference|**	**CFD Value**	**|Relative Difference|**	**CFD Value**	**|Relative Difference|**
λ/d	2.65	2.83	6.8%	3.06	15.5%	2.76	4.2%
B/d	0.77	0.84	9.1%	0.84	9.1%	0.84	9.1%
h_{tp}/d	1.68	1.80	7.1%	1.94	15.5%	1.69	0.6%

Figure 4.10 and Table 4.2, this makes the case that all of the CFD predictions in this study for λ in a turbulent interaction were too far upstream. Overall, the differences in λ/d and h_{tp}/d, as parameter of interest between the cylinder of height y/d = 4 and y/d = 10, were within 10% of one another, as indicated by the differences between Table 4.1 and Table 4.2. Therefore, the discrepancies between experiments and CFD results are not severe, and the data are in good quantitative agreement.

The centerline streamlines were analyzed again using only *u* and *v*, and are shown in Figure 4.13a-f, with Figure 4.13a-c showing Mach number contours with the same contour levels as in Figure 4.11a, and Figure 4.13d-f only showing the streamlines with no contour. Many similarities were observed when compared to the results with a cylinder of height y/d = 4. The single, large, primary vortex was still present, with smaller-scale vortices located in the corner region. The flow separation and attachment lines, corresponding to *SL* and *AL* in Figure 2.7, respectively are also visible. The streamlines near the corner region, similar to those shown in Figure 4.4a-c, are provided in Figure 4.14a-c. Again, the Mach number contours were altered to show the subsonic portion of the flow. These contours indicate a lower-velocity flow in this region for all turbulence model results when compared to the results with the cylinder of height y/d = 4. Furthermore, the attachment line corresponding to *AL1* in Figure 2.7 had shifted downstream for all turbulence model results, with the smallest shift occurring for the SA-QCR turbulence model result. This shift decreased the size of both the secondary and tertiary vortices; therefore, it appears that the secondary and tertiary are correlated in size. All in all, the further separation is induced upstream, the larger the separation bubble becomes; a larger separation bubble induces a slower velocity about the secondary vortex and drives it further downstream, thus decreasing the size of this secondary vortex. It follows then that the size of the tertiary vortex is decreased, along with the sizes of any potential smaller vortices.

4.1.2.3 Surface Pressure Analysis

Similar to the analysis performed on the cylinder with height y/d = 4, the surface pressure ratio upstream of the cylinder was assessed. This normalized pressure ratio is shown in Figure 4.15 for all turbulence models, and is very similar in both shape and

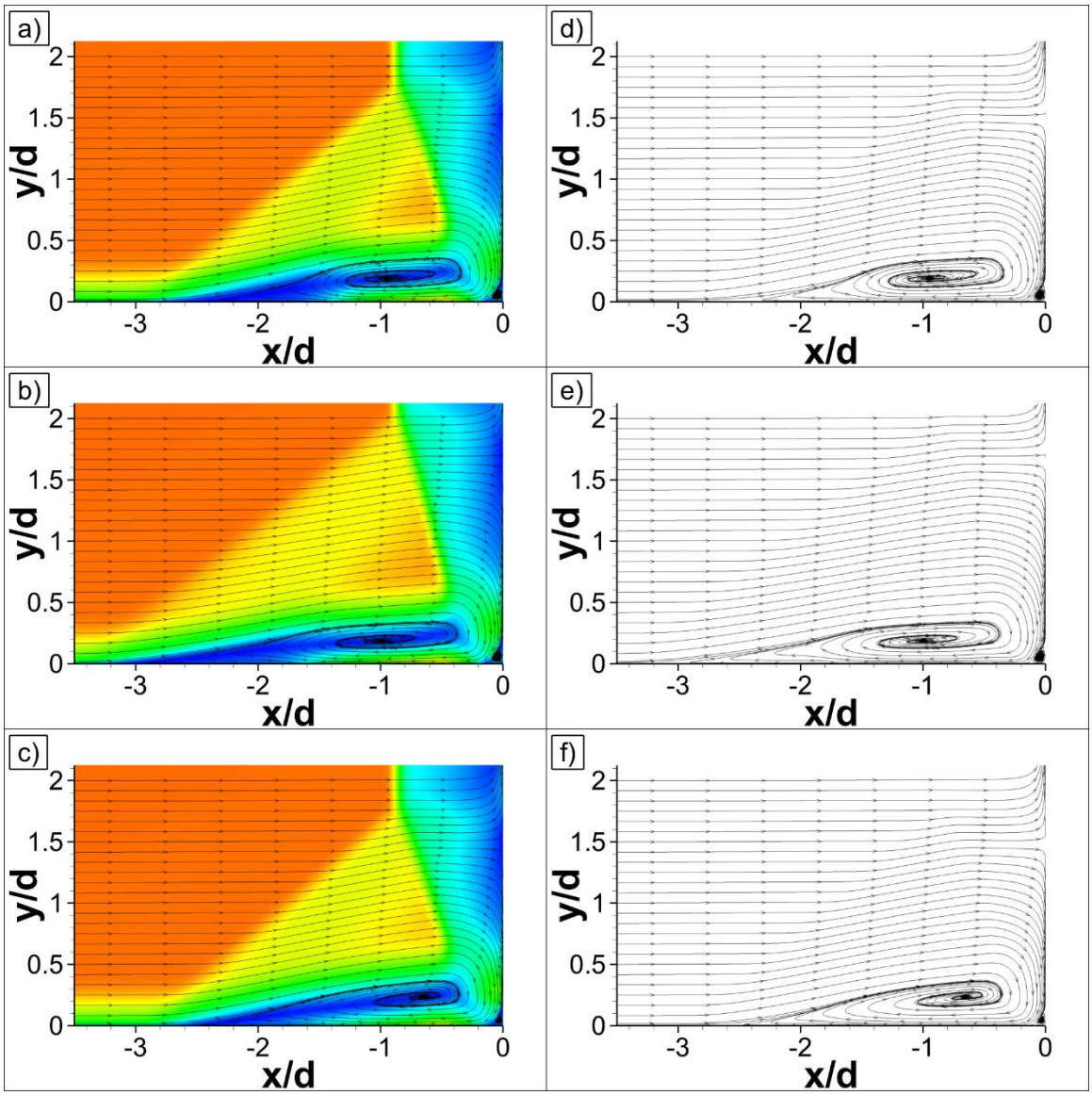


Figure 4.13. Streamlines on fine mesh results for cylinder of height *y/d* = 10. a) - c) With d) - f) and without Mach number contours, for CKE, SST, and SA-QCR turbulence models, respectively.

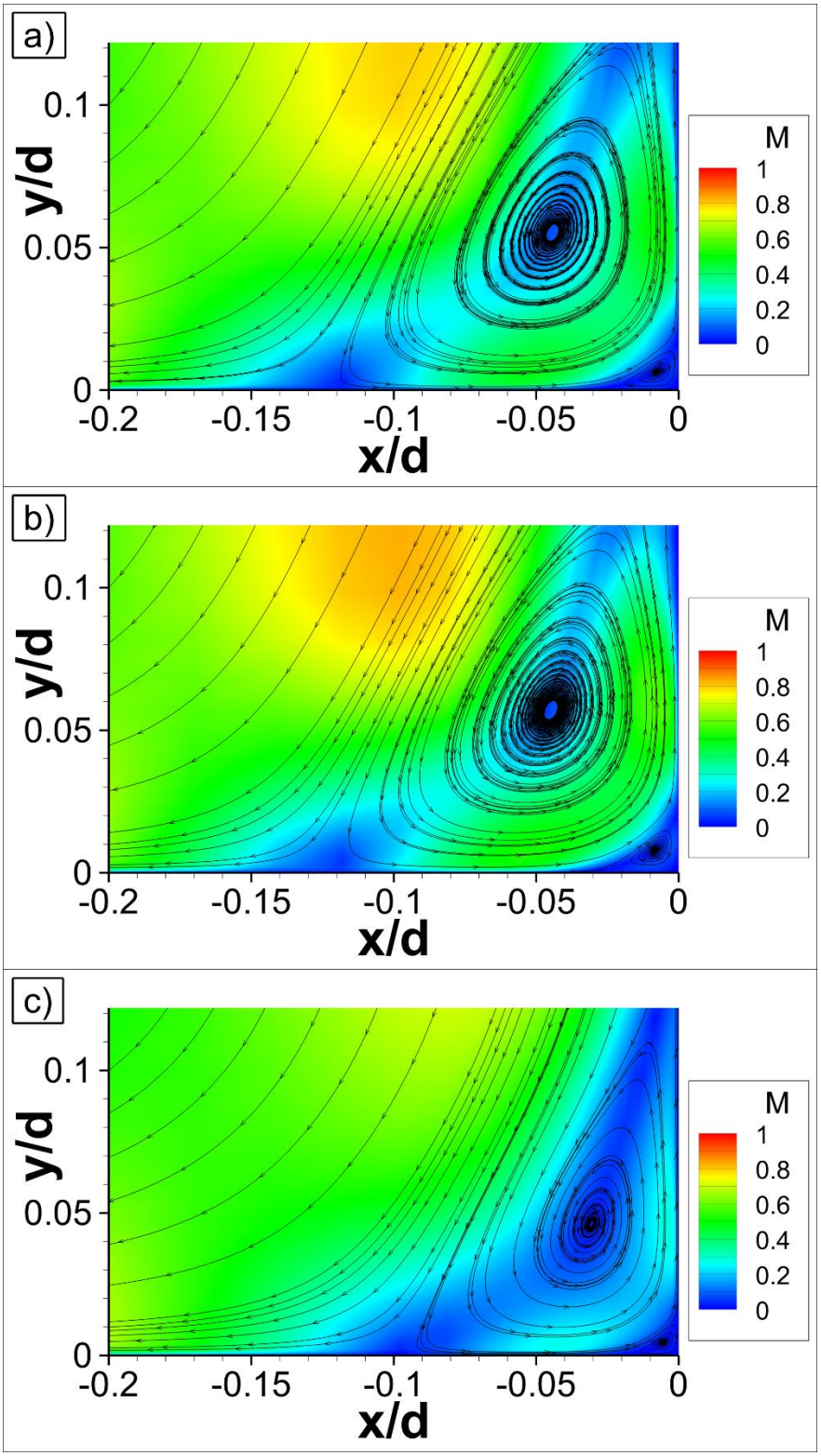


Figure 4.14. Streamlines on zoomed-in corner region of fine mesh results for cylinder of height *y/d* = 10. a) - c) Mach number contours for CKE, SST, and SA-QCR turbulence models, respectively.

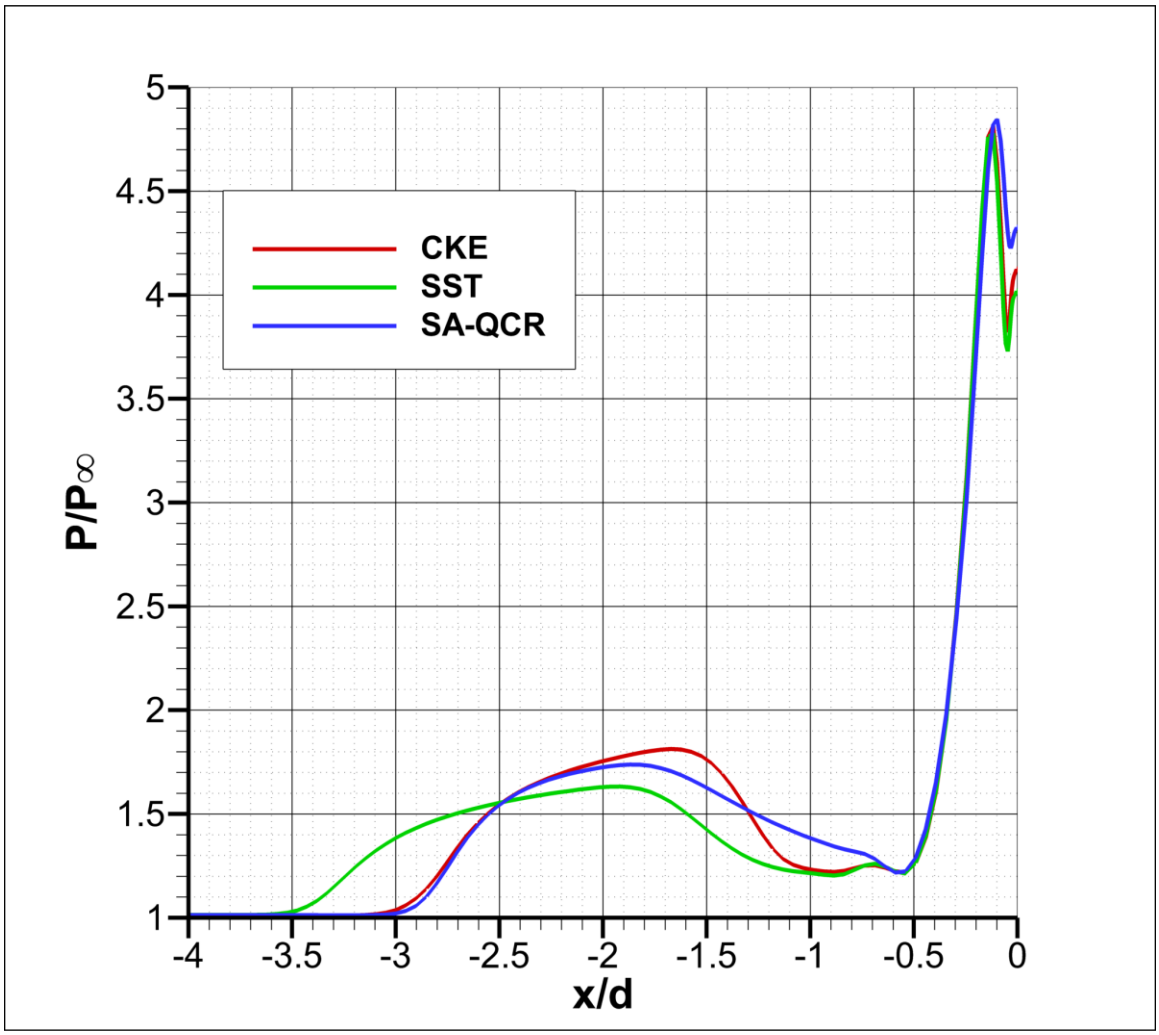


Figure 4.15. Fine mesh results with indicated turbulence models, showing normalized pressure on the flat plate surface, upstream of the cylinder with height y/d = 10.

magnitude as the results shown in Figure 4.5 for the cylinder with height y/d = 4. The largest differences between the two was that the initial pressure rise had shifted upstream by approximately 0.2d for the SST and SA-QCR turbulence model results, that the trough pressure had shifted upstream by approximately 0.05d for all turbulence model results, and that the surface pressure downstream of the peak pressure had increased from $P/P_\infty \approx 3.4$ for the cylinder with height y/d = 4 to $P/P_\infty \approx 3.8$. It is likely that this increase in pressure was in correlation with the reduced size of the secondary vortex, but further investigation is required to ascertain this.

The normalized surface pressure ratio on the cylinder leading edge is shown in Figure 4.16 for all turbulence models. Starting at the base of the cylinder and moving upwards, some initial fluctuations were observed for all turbulence model results, followed by a decrease that led to the trough pressure around y/d = 0.3. The lowest trough pressure was observed with the SA-QCR turbulence model at around $P/P_{0,2} \approx 0.5$. This was followed by a pressure rise until the peak pressure around y/d = 1.6 for the CKE and SA-QCR turbulence models, and y/d = 1.8 for the SST turbulence model, with $P/P_{0,2} \approx 1.2$. Upwards of this peak pressure, the triple point occurred, and above this, the inviscid bow shock was present, where $P/P_{0,2} = 1$.

Based on the quantitative and qualitative results gathered, either the CKE or SA-QCR turbulence models were deemed appropriate choices for this type of flow. However, comparisons with the in-house experiments [6, 7] and Yamamoto and Takasu [15] make it clear that an unsteady analysis must be performed to fully characterize the flow. As previously mentioned, an initial study was conducted using hybrid RANS/LES that used the CKE turbulence model in the near-wall region [47]. However, the results were not as promising as expected, and therefore, a future study will be conducted with an improved delayed detached eddy simulation (IDDES) that uses the SA turbulence model in the near-wall region [48]. In preparation for this, the results with the SA-QCR turbulence model were more closely analyzed, although the results with the CKE turbulence model provided equally feasible results.

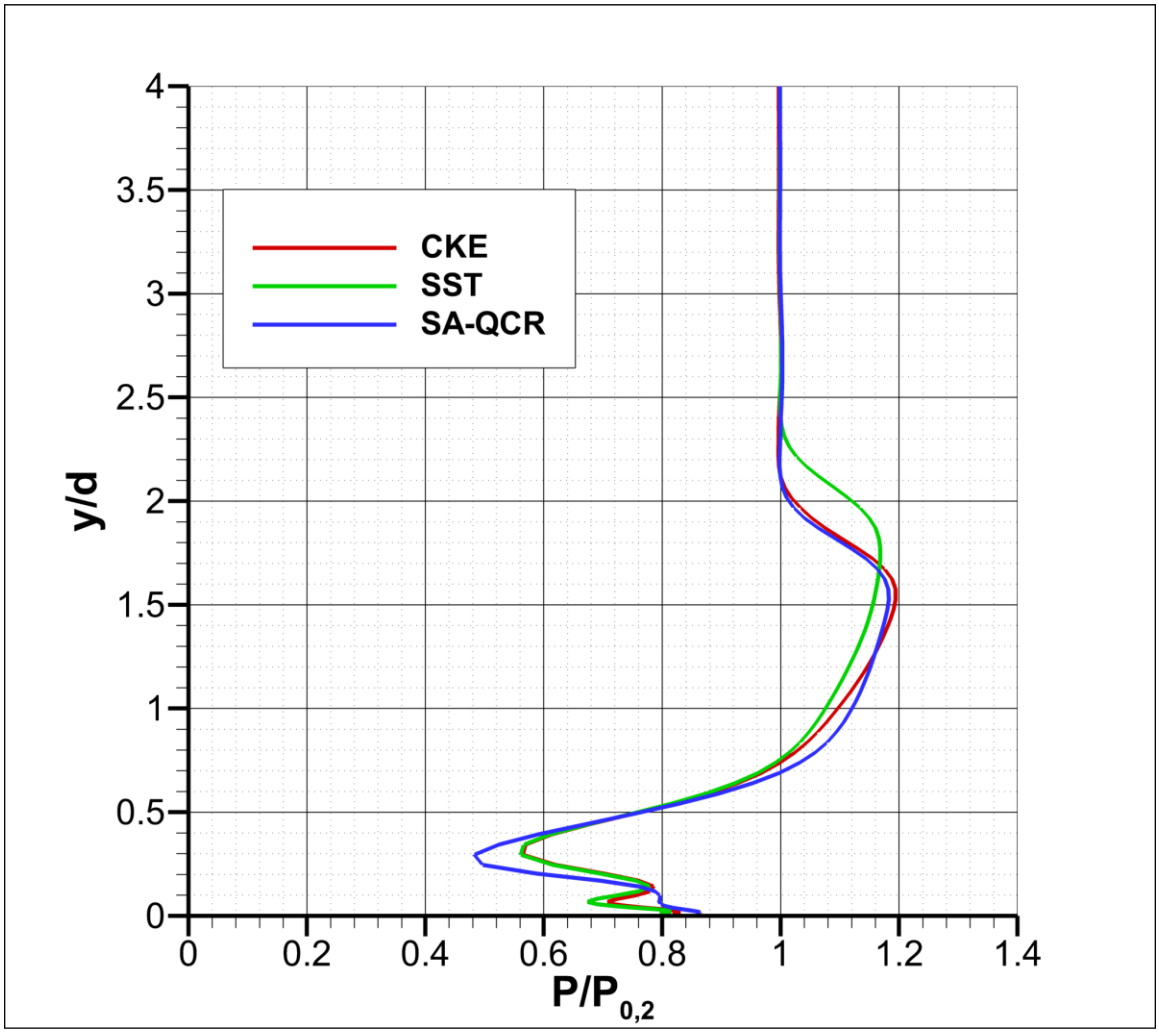


Figure 4.16. Fine mesh results with indicated turbulence models, showing normalized pressure on the leading edge of the cylinder with height *y/d* = 10.

Similar to the results shown by Özcan and Yüceil [14], Figure 4.17a and b presents a top view of the flat plate surface in the *x-z* plane, with flow moving from bottom to top. Here, Figure 4.17a shows the skin friction coefficient, C_f, multiplied by a factor of 1000, with the contour levels cut off below $C_f = 0.001$ and above $C_f = 0.01$. Figure 4.17b shows the normalized pressure ratio, and the contour levels were cut off below $P/P_\infty = 0.6$ and above $P/P_\infty = 2$. These cut-offs were done to provide clarity in the figures. It can be seen in both Figure 4.17a and b that the initial pressure rise was correlated with a friction value below the freestream condition. The pressure plateau, indicated by the contour line $P/P_\infty = 1.7$ in Figure 4.17b, decreased in magnitude as the flow moved outboard from the centerline. Similarly, the surface peak pressure also decreased in magnitude as the flow moved outboard, but at a steeper rate and sharper angle. It was discovered in Figure 4.17a that the lowest C_f upstream of the cylinder corresponded to the separation point between the secondary and tertiary vortices, as shown in Figure 4.14. Furthermore, the diverging streamlines of the primary and secondary vortices also corresponded to a region of low friction. These correlations are physical, as the low subsonic flow in these regions will generate less shear stress along the flat plate surface than a higher-speed flow would. From both Figure 4.17a and b it can be seen that the bulk of the interaction was within $z/d = \pm 2$ off the centerline, and although the effects of the protuberance were still visible further outboard, they were relatively weak in magnitude. This indicates that in addition to the interaction behaving in a closed sense, as described by Clemens and Narayanaswamy [10], it also behaves in an open sense away from the centerline, since the horseshoe vortices sweep outboard and continuously decrease the strength and scale of the interaction.

4.1.2.4 Effect of Incoming Boundary Layer Height

Because the SA-QCR turbulence model was selected as the most accurate, the effect of δ/d was studied using this turbulence model as well. The same variation of δ/d was imposed here as for the cylinder with height $y/d = 4$, such that the smallest boundary layer had $\delta/d = 0.25$ and the largest boundary layer had $\delta/d = 2.50$, and the increment remained at 0.25. As before, the result that compared to the experiment, where $\delta/d = 0.3622$, was excluded to allow for a constant increment analysis. In a similar manner to Figure 4.6a-j, numerical

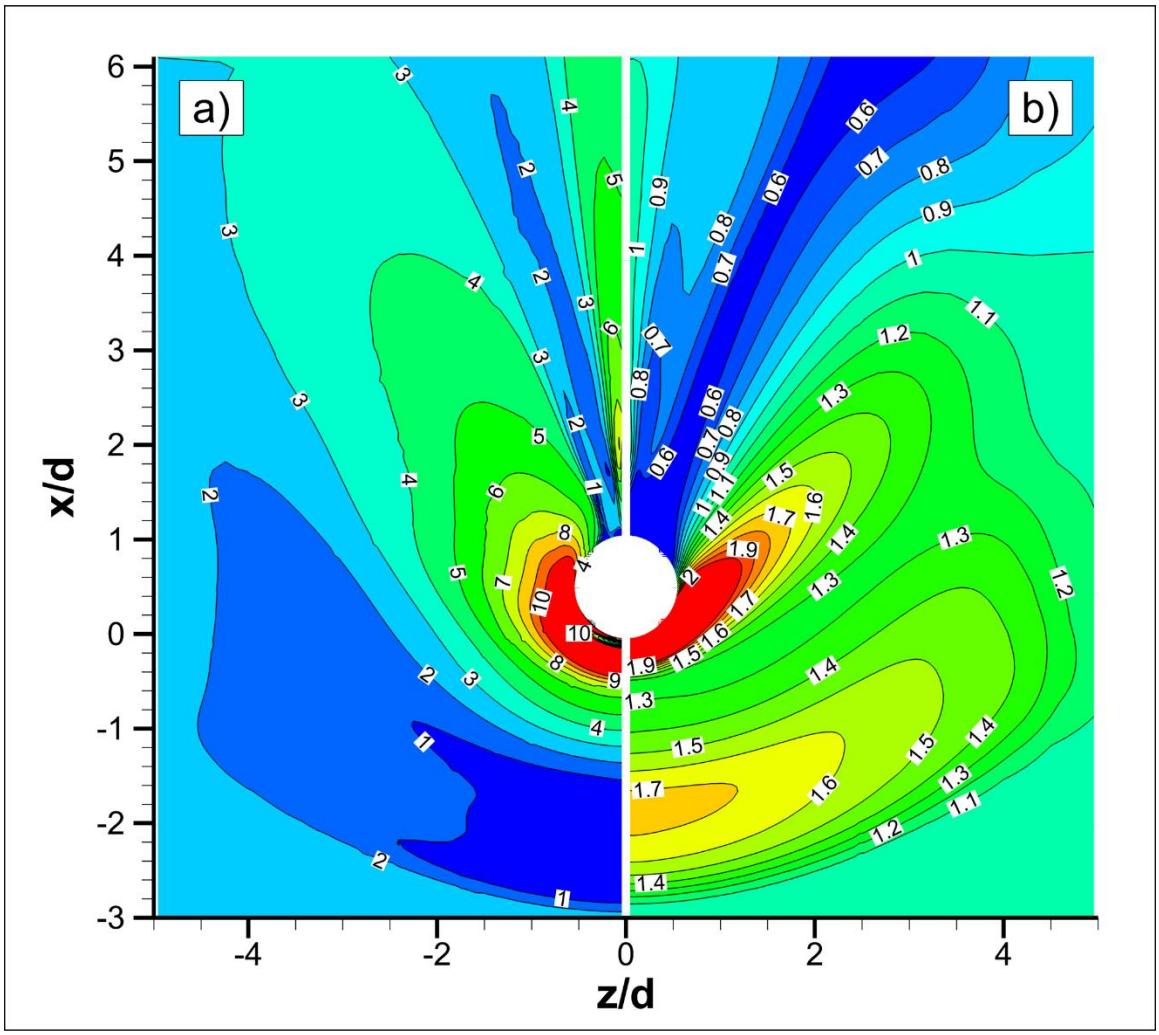


Figure 4.17. a) Skin friction coefficient × 10^3 and b) normalized surface pressure ratio lines and contours at y/d = 0 with SA-QCR turbulence model for cylinder of height y/d = 10. Flow from bottom to top.

Schlieren contours in the x-y plane are shown in Figure 4.18a-j, where Figure 4.18a represents δ/d = 0.25, each successive letter represents an increment by 0.25 from the previous letter, and the final value of δ/d = 2.50 is shown in Figure 4.18j. Similar qualitative trends as observed with the cylinder of height y/d = 4 are visible here for increasing δ: the forward shock shifted upstream, the triple point shifted upward, the separation bubble increased in size, and the supersonic regions at the wall near the corner decreased in size until they eventually disappeared. The strength of the interaction decreased with increasing δ, as did the strength of the forward shock. Furthermore, both the forward and trailing shocks curved more strongly inward. Visually, it appears as though the separation length remained at about λ/d = 3.0, while the onset of separation continued to shift upstream. The separation bubble plateaued in height for $\delta/d \geq 1.25$, and the trailing shock foot remained relatively constant at about y/d = 0.7 for these cases. Note that even for the largest value of δ/d, $h_{tp}/d \approx 2.5$, resulting in $h/h_{tp} \approx 4$, which ensured that the semi-infinite height condition of h/h_{tp} > 2-3 [12] was met.

A quantitative analysis of the parameters of interest is shown in Figure 4.19a-c, where, similar to Figure 4.7a-c for the cylinder of height y/d = 4, the parameters of interest were again compared to the empirical values [11], including a ±10% error threshold. From Figure 4.19a it can be seen that the separation length remained relatively constant at $\lambda/d \approx$ 2.84 for $\delta/d \geq 0.75$, with a slightly decreasing trend; the exact values for the δ/d = 0.75 and δ/d = 2.50 cases were λ/d = 2.85 and λ/d = 2.82, respectively. This relatively constant value for λ implies that the curvature of the forward shock becomes very strong in the near-wall region for $\delta/d \geq 0.75$, considering that the numerical Schlieren contours in Figure 4.18c-j indicate λ/d > 3. The bow shock stand-off distance in Figure 4.19b also remained relatively constant around B/d = 0.84, with a small increasing trend, such that B/d = 0.83 for δ/d = 0.25, and B/d = 0.85 for $\delta/d \geq 1.75$. The combination of a decreasing λ and increasing B further verified the observation that an increased δ resulted in a decreased streamwise distance between the forward and trailing shocks for the same y, and thus a decreased scale of the interaction. The curvature of the forward shock also impacted the calculated height of h_{tp}, as indicated by Figure 4.19c. Due to φ being measured near the triple point, this

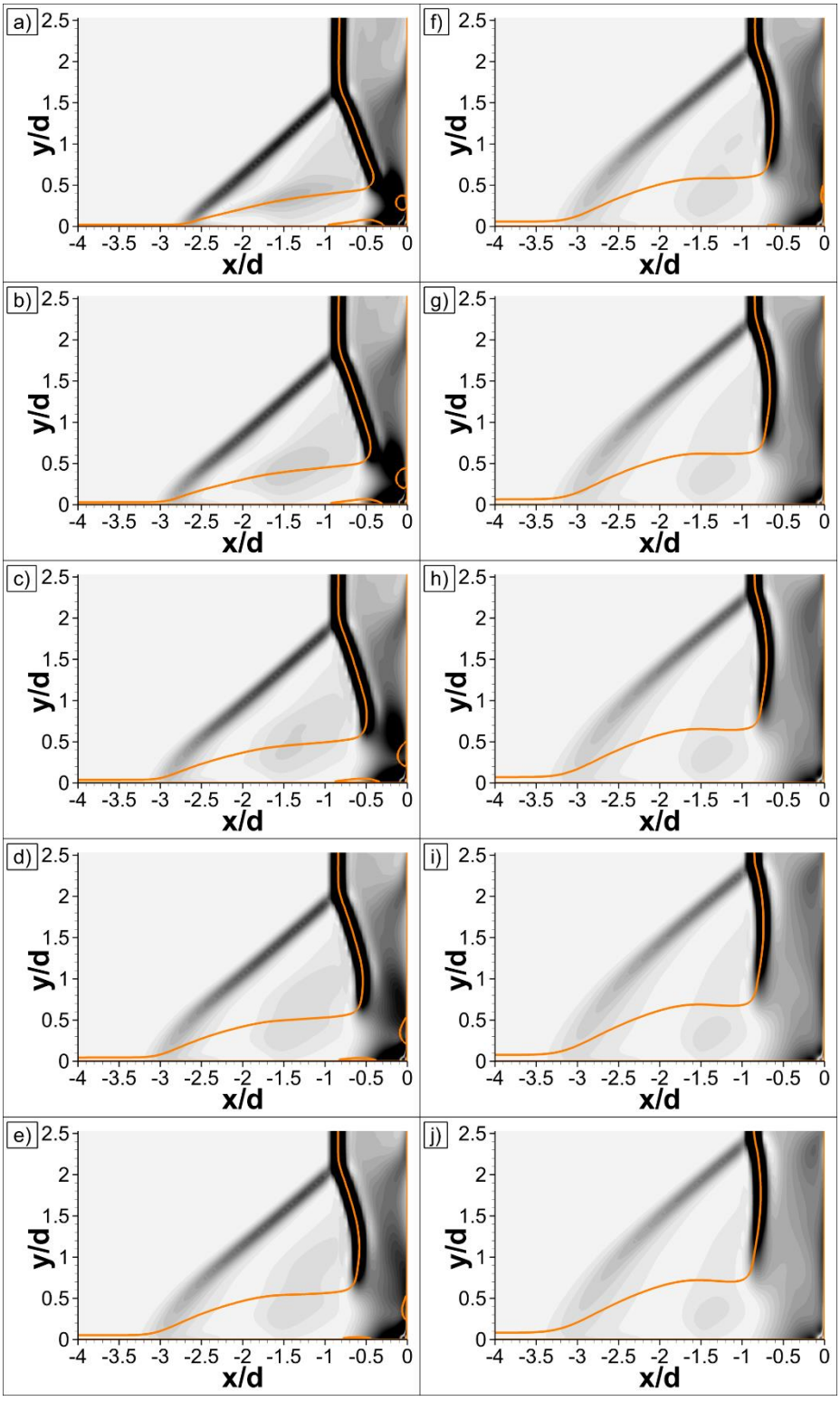


Figure 4.18. Fine mesh results with varied incoming boundary layer height δ/d for cylinder with height y/d = 10. a) - j) δ/d = 0.25 to δ/d = 2.50 with constant increment of 0.25. Orange line represents sonic line.

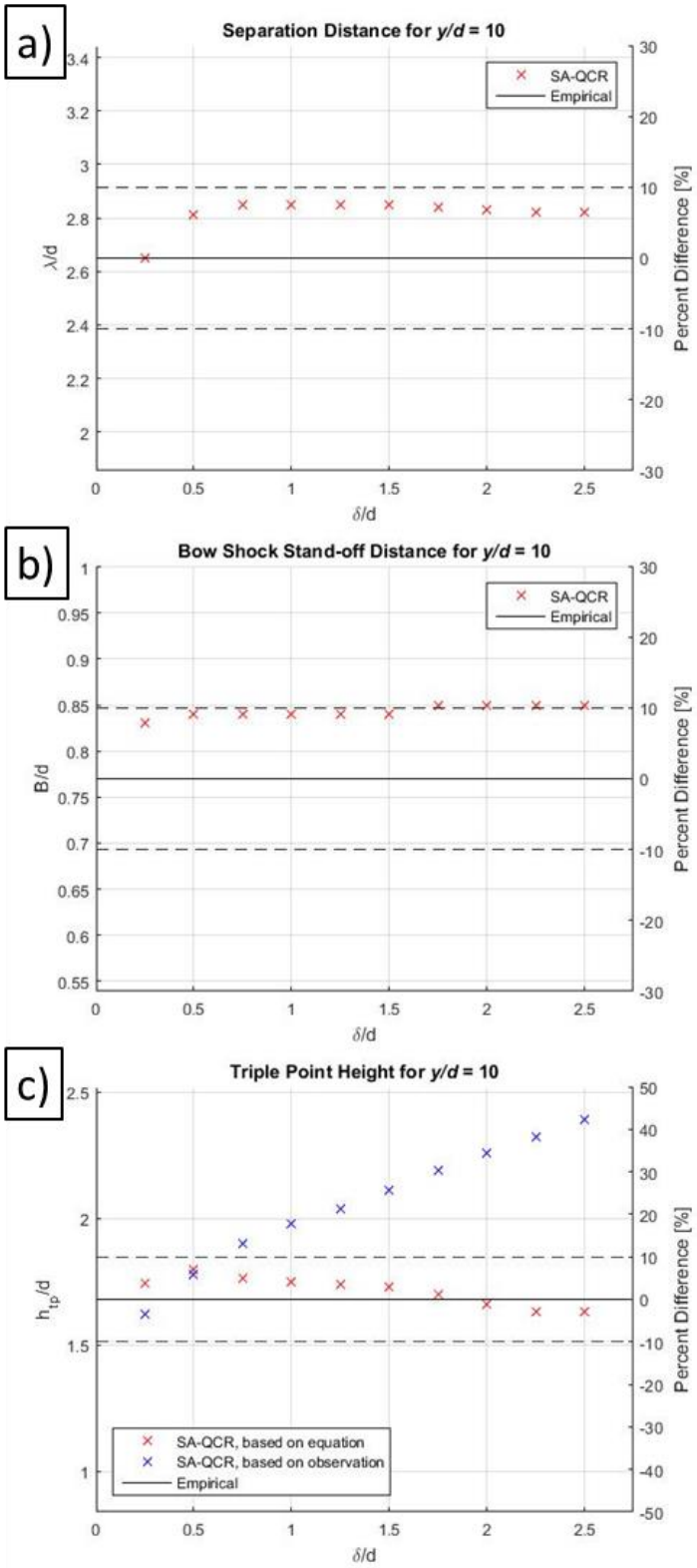


Figure 4.19. Comparison of parameters of interest between empirical values [11] and fine mesh results for varied δ/d with cylinder of height y/d = 10. a) λ/d, b) B/d, c) h_{tp}/d.

curvature was not accounted for. However, the values for h_{tp}/d obtained via Equation (2-3) provided a stronger argument for a decreased distance between the forward and trailing shock, as the equation takes into account the difference between the two. Nevertheless, this analysis showed that Equation (2-3) is only valid for small values of δ, where the forward shock foot is relatively straight; this occurred only for $\delta/d \leq 0.50$. The observed values for h_{tp}/d in Figure 4.19c were taken from the numerical Schlieren contours in Figure 4.18a-j, and indicated a positive linear trend with increasing δ.

The pressure ratio on the flat plate surface is shown in Figure 4.20. The initial pressure rise shifted further upstream with increasing δ, as expected. There was a larger jump in the shift from $\delta/d = 0.25$ to $\delta/d = 0.50$ than for any other adjacent pair. For the larger values, where $\delta/d \geq 2$, the shift became very small, such that this was within $0.01d$. The magnitude of the pressure plateau decreased with increasing δ. A uniform pressure decrease for all cases, except $\delta/d = 0.25$, occurred after the pressure plateau, until around $x/d = -0.9$. The trough pressure here varied in both magnitude and location, with a lower magnitude and further downstream location occurring for smaller δ. An opposite trend was present for the peak pressure, where a smaller δ correlated with a higher peak pressure at a slightly further upstream location. These results are in good agreement with those for the cylinder of height $y/d = 4$, although there was an offset for the case where $\delta/d = 0.25$. Based on the results gathered, a conclusion drawn is that a larger δ/d, and thus a larger δ/h_{tp}, is desirable for a SWTBLI generated by a cylinder (or blunt fin), as this decreases the scale of the interaction and drives down the peak pressure that can cause excess aerothermal and structural loading. Therefore, a recommendation is to conduct a future study that identifies the effects of δ/h_{tp}.

The pressure ratio on the cylinder leading edge is shown in Figure 4.21. The general shape and trends were again in good agreement with literature [11, 16], but differed slightly from the results with a cylinder of height $y/d = 4$. The largest differences observed were at the base of the cylinder, where small values of δ induced seemingly large fluctuations for the cylinder of height $y/d = 4$. This was not the case for the cylinder of height $y/d = 10$, where only minor fluctuations were observed at the base for any δ, although the magnitude of these fluctuations was larger for smaller δ. The trough pressure also varied in both

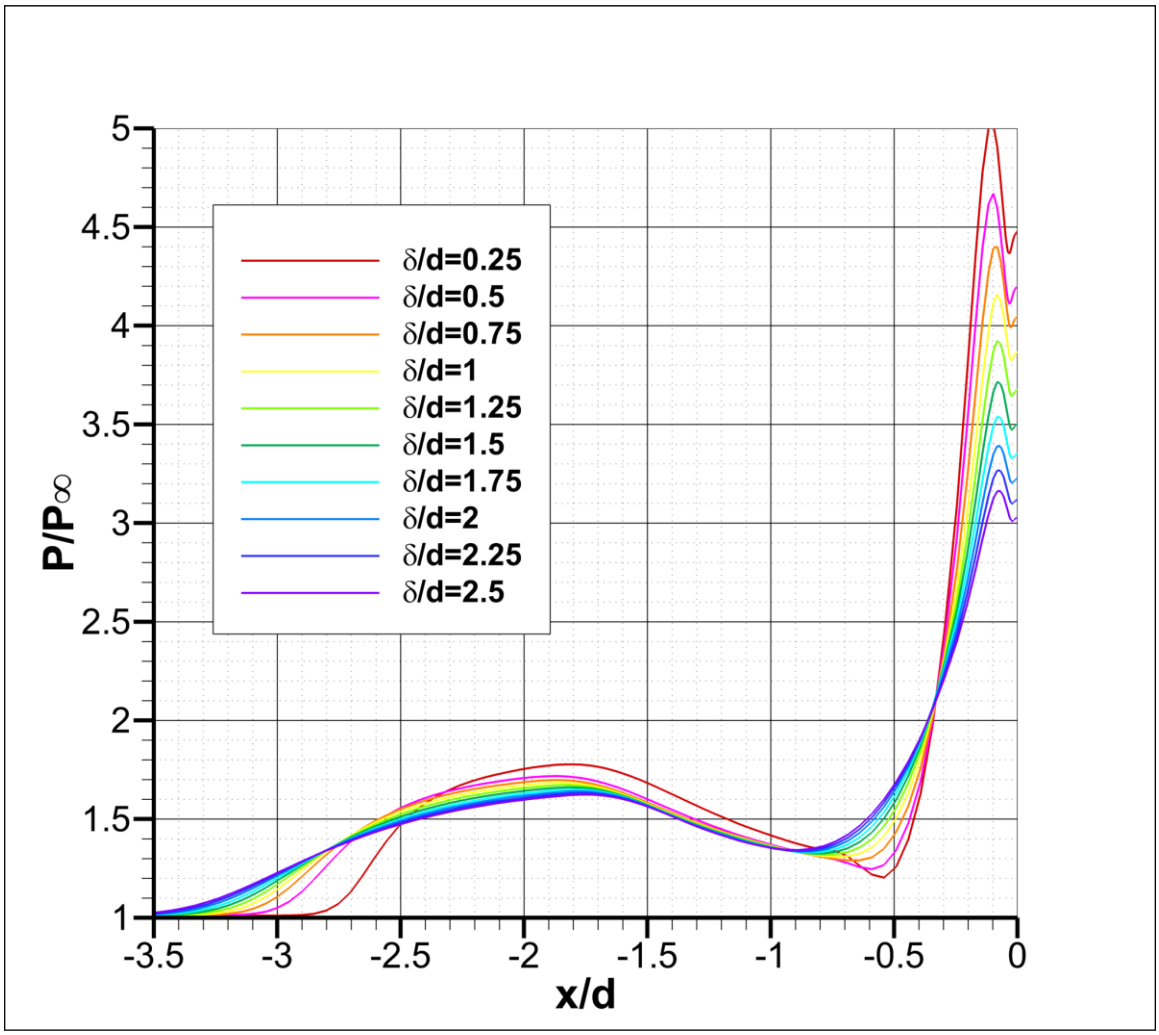


Figure 4.20. Fine mesh results with varied *δ/d*, showing normalized pressure on the flat plate surface, upstream of the cylinder with height *y/d* = 10.

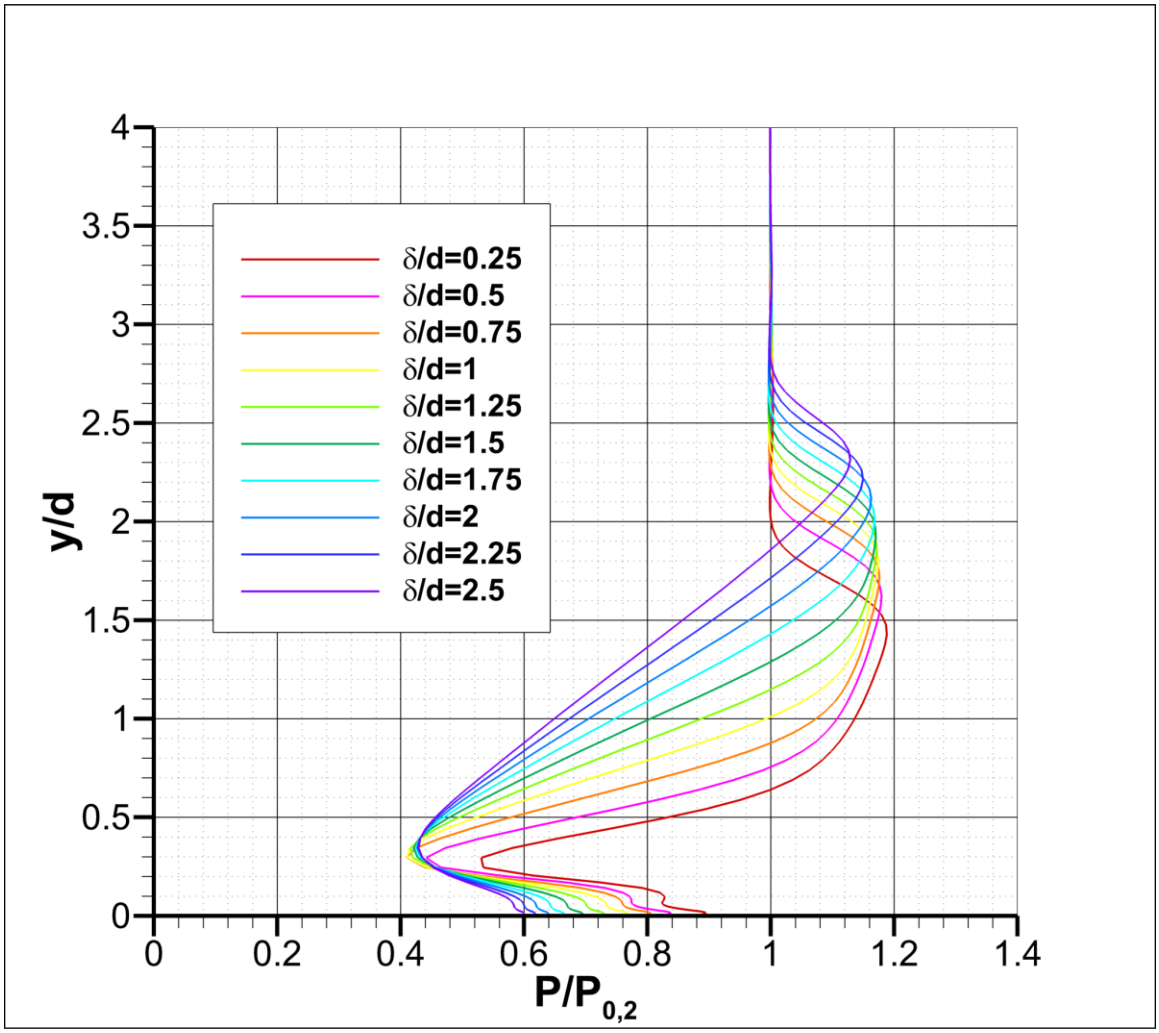


Figure 4.21. Fine mesh results with varied *δ/d*, showing normalized pressure on the cylinder leading edge of the cylinder with height *y/d* = 10.

magnitude and location. As for the location, the trough pressure was around $y/d = 0.3$ for $\delta/d = 0.25$ and monotonically increased to around $y/d = 0.35$ for $\delta/d = 2.50$. The magnitude was largest for $\delta/d = 0.25$, resulting in $P/P_{0,2} \approx 0.52$. The magnitude continued to decrease until $\delta/d = 1.00$, where $P/P_{0,2} \approx 0.42$. As δ/d was increased from 1.00 to 2.50, the magnitude increased again until about $P/P_{0,2} \approx 0.44$. This initial decrease and sudden increase in trough pressure magnitude with increased δ/d is unexpected, but it did not seem to have any effect on the remainder of the pressure distribution. The peak pressure for each case was located again just downwards of the triple point, and within the range of $P/P_{0,2} \approx 1.18$ for $\delta/d = 0.25$ to $P/P_{0,2} \approx 1.12$ for $\delta/d = 2.50$, with a seemingly linear decreasing trend. Upwards of this peak pressure location, all pressure ratios returned to the inviscid value of $P/P_{0,2} = 1$.

4.1.3 SWTBLI Topology Characterization with RANS

The streamlines for both cylinder heights, shown in Figure 4.3 for the cylinder of height $y/d = 4$ and in Figure 4.13 for the cylinder of height $y/d = 10$, were identical in both trend and behavior. Therefore, a graphic similar to that produced in Figure 2.7 was created using the method of Hunt et al. [49], and is shown in Figure 4.22 for the SA-QCR turbulence model result. The nodes and half-saddles were found using the Jacobian of the shear stress tensor τ. As required by Hunt et al. [49], the 2 nodes subtracted by the 4 half-saddles yielded 0, since each node was associated with 1 separation line and 1 attachment line. A few correlations were found: *SL1* corresponds to λ, *AL1* corresponds to the peak pressure location on the cylinder leading edge, *AL2* corresponds to the peak pressure location on the flat plate surface, and *SL2* is loosely correlated to the trough pressure on the cylinder leading edge. It can be seen in Figure 4.22 that the streamlines turn with the oblique forward shock, and again with the oblique trailing shock. Near *AL1*, the streamlines were almost tangential again to the flat plate surface. Note that *AL1* was at a slightly lower height than the triple point. Furthermore, *SL2* was located downwards of the trough pressure location on the cylinder leading edge. This topological characterization aligns with the experimental characterization of Sedney and Kitchens [20] and with the computational steady-state results reported by Hung and Buning [16], but not with the unsteady results from

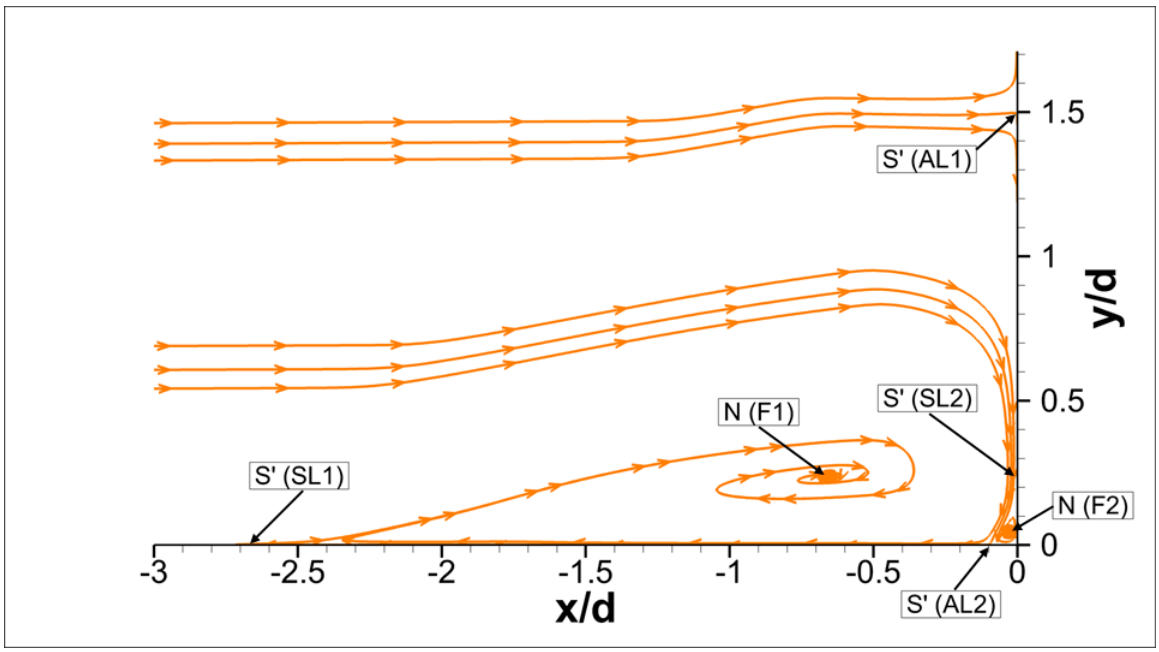


Figure 4.22. Topological model of SWTBLI using streamlines at z/d = 0 for SA-QCR turbulence model with fine mesh and cylinder of height y/d = 10.

Yamamoto and Takasu [15], and it must be noted that this characterization is thus only valid for steady-state RANS simulations of a semi-infinite-cylinder-induced SWTBLI. The dimensions and scales of the interactions will vary depending on the choice of turbulence model and flow conditions, but dimensions were still provided here for reference.

4.2 Laminar Interactions

As with the turbulent interaction cases, a grid independence study was performed first. Again, λ/d, B/d, and h_{tp}/d were selected as the parameters of interest, and were used to determine whether or not a mesh was well-converged. Furthermore, a mesh-converged result was compared with empirical/theoretical parameters from literature. Recall that for a laminar interaction, the experimental separation length was approximately λ/d = 5.5-6 [24]. As an estimate, a target value of λ/d = 5.75 was selected. The separation length was numerically determined in a similar manner as for the turbulent interaction results, that is, by analyzing the furthest upstream location where reversed flow was present. The empirical stand-off distance remained the same as for the turbulent interaction, such that B/d = 0.77,

and was numerically determined through the largest streamwise extent of the sonic line in the inviscid region. Using Equation (2-4), a wave angle of $\varphi = 35.4°$ was calculated, and this resulted in an empirical triple point height of $h_{tp}/d = 3.59$.

4.2.1 Grid Independence Study

The grid independence study for the laminar interaction, as outlined in Table 3.4, was completed successfully, and results are summarized in Figure 4.23a-c. It can be seen that for the medium through extra fine mesh results, little variation existed for all parameters of interest. The bow shock stand-off distance in Figure 4.23b was modeled closer to the empirical value than for the turbulent interaction, shown in Figure 4.10b. The separation length in Figure 4.23a was in good agreement with the λ/d = 5.5-6 range reported by Leidy et al. [24], but further downstream than the older reported values of λ/d = 6-9 by Kaufman et al. [8]. Leidy et al. [24] found that a higher Re_m decreased λ; the results here were obtained with $Re_m = 2.83 \times 10^6$ m^{-1}, which was close to, but lower than the $Re_m = 3.0 \times 10^6$ m^{-1} reported by Leidy et al. [24]. Therefore, values closer to, or exceeding $\lambda/d = 6$ were expected. Since the triple point height was determined with the same uncertainty as the separation length, the empirical value of h_{tp}/d in Figure 4.23c could be considered within the ±10% bounds. Despite the medium mesh producing parameters of interest that were sufficiently accurate and similar to those of the more resolved meshes, the results reported here will be for the extra fine mesh. Note that this is simply because the extra fine mesh provided cleaner shock resolution, and that the medium mesh results provide an equally valid analysis.

4.2.2 Comparison to Empirical Values

The centerline plane of the laminar interaction is shown in Figure 4.24a and b, where Figure 4.24a shows the Mach number contours, and Figure 4.24b shows the numerical Schlieren contours. The black solid line in the Mach number contour represents the sonic line. Note that the numerical Schlieren here is the summation of the density gradient in each of the 3 Cartesian coordinates, rather than a single vertical or horizontal knife edge representation; this was done to properly view the bow shock and separation bubble at the

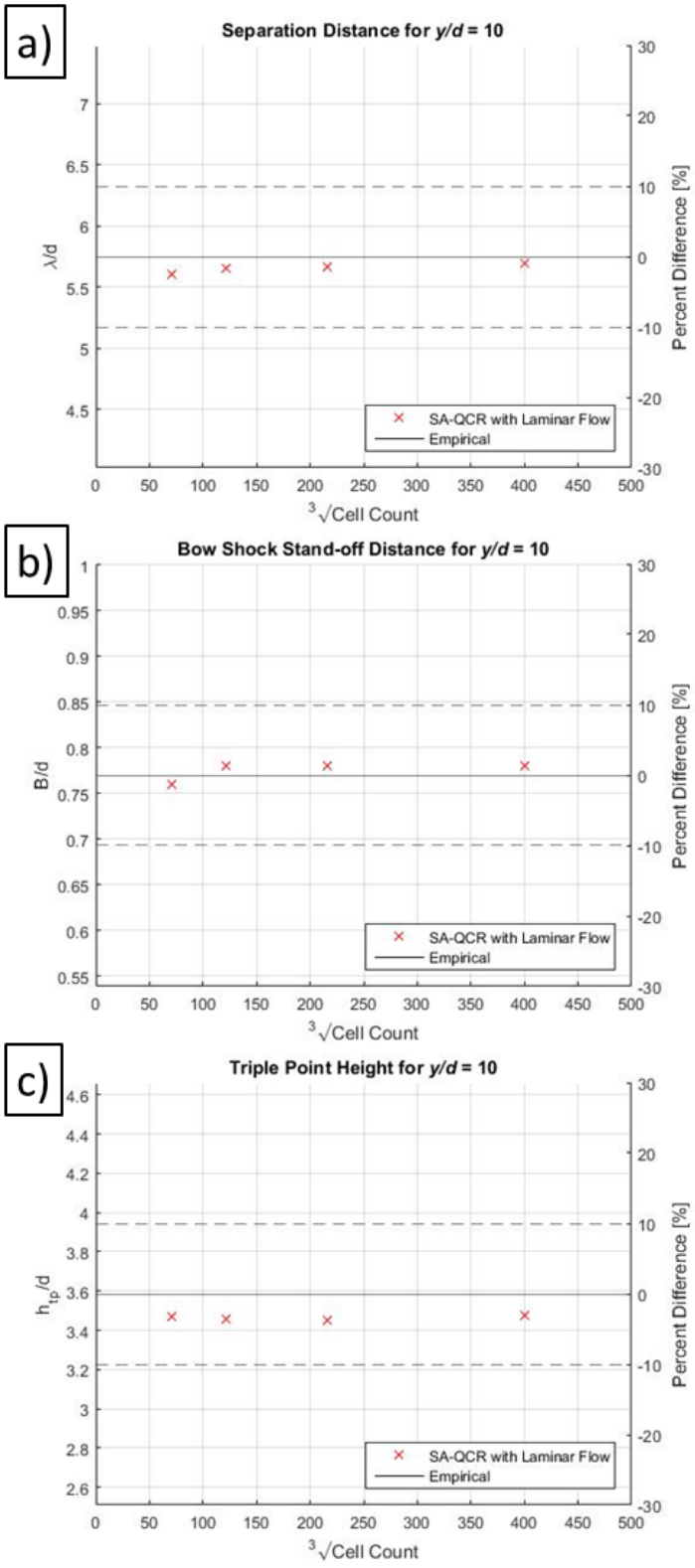


Figure 4.23. Grid independence study comparing the parameters of interest for laminar interaction. a) λ/d, b) B/d, c) h_{tp}/d.

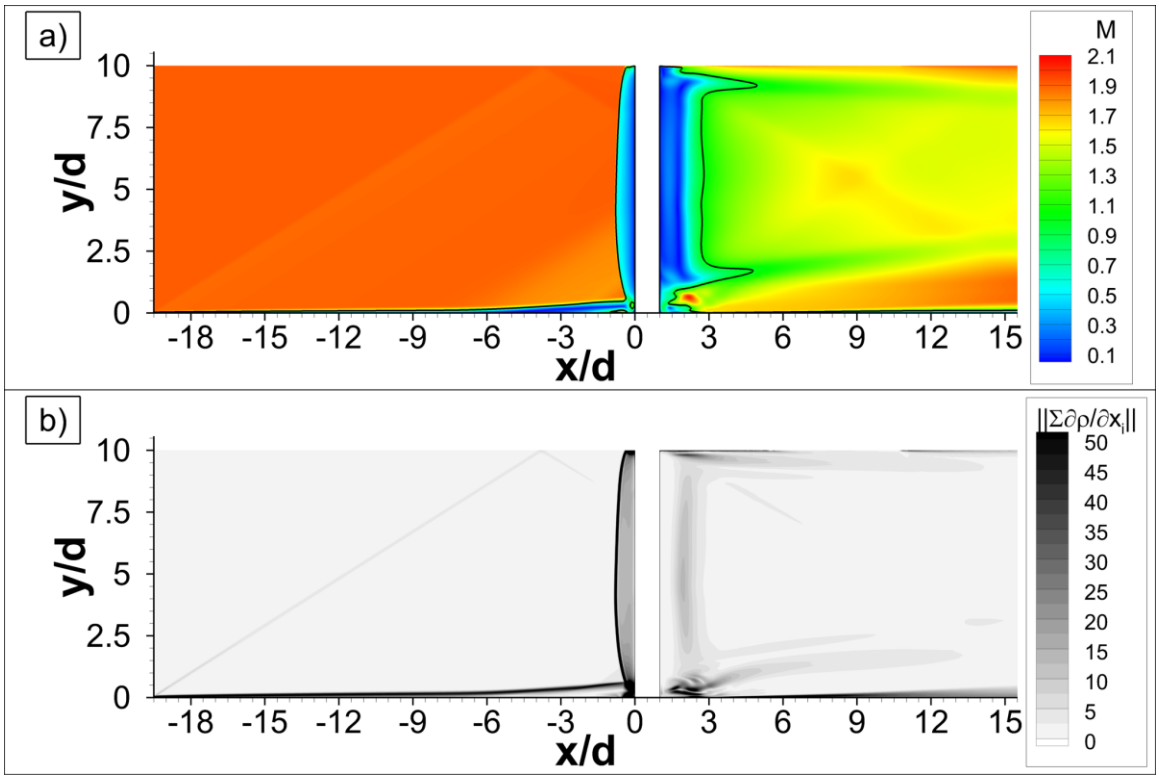


Figure 4.24. a) Mach number and b) numerical Schlieren contours of extra fine mesh result at $z/d = 0$. Black line in a) is sonic line.

same time, which were only clear with either a vertical or horizontal knife edge representation, respectively. Also note that the maximum contour level for the numerical Schlieren was an order of magnitude lower than for the turbulent interaction, indicating that the strength of the laminar interaction was much weaker than that of the turbulent interaction. It can be seen in both the Mach number contour of Figure 4.24a and the numerical Schlieren contour of Figure 4.24b that a Mach wave emanated from the surface, reflected off the upper boundary domain, and impinged upon the bow shock. The origin of this is likely due to a misalignment of the second coordinate in the Blasius laminar boundary layer profile and the y^+ cell height in the mesh, or due to a cell-centered versus node-centered misalignment. Nevertheless, the impingement of the Mach wave upon the bow shock occurred far away from the region of interest and did not affect the interaction. The wake extended only about 4*d* downstream of the cylinder for the extra fine mesh result; however, this extension was around 12*d* for the medium mesh result. A variation in the upstream interaction was not observed, and so this difference was not of any particular concern. The separation bubble grew at a much shallower slope than for the turbulent interaction, and this small deflection angle resulted in a very weak forward shock. This is slightly visible in the Mach number contour in Figure 4.24a, but not at the given contour levels for the numerical Schlieren in Figure 4.24b. In order to examine the overall flow structure while also observing the more subtle variations in the flow, Figure 4.25a-d shows a comparison between the full contour levels, as shown in Figure 4.25a and d, and reduced contour levels, as shown in Figure 4.25b and c. For the Mach number contours in Figure 4.25a and b, the pink solid line represents the sonic line. Similarly, for the numerical Schlieren contours in Figure 4.25c and d, the orange solid line represents the sonic line. The empirical values are superimposed as the dashed lines in black and pink for the Mach number and numerical Schlieren contours, respectively. A forward shock is more clearly visible in these reduced contour levels, as is the Prandtl-Meyer expansion fan near $x/d = -1$. Furthermore, a good qualitative agreement between the empirical values and the parameters of interest is visible.

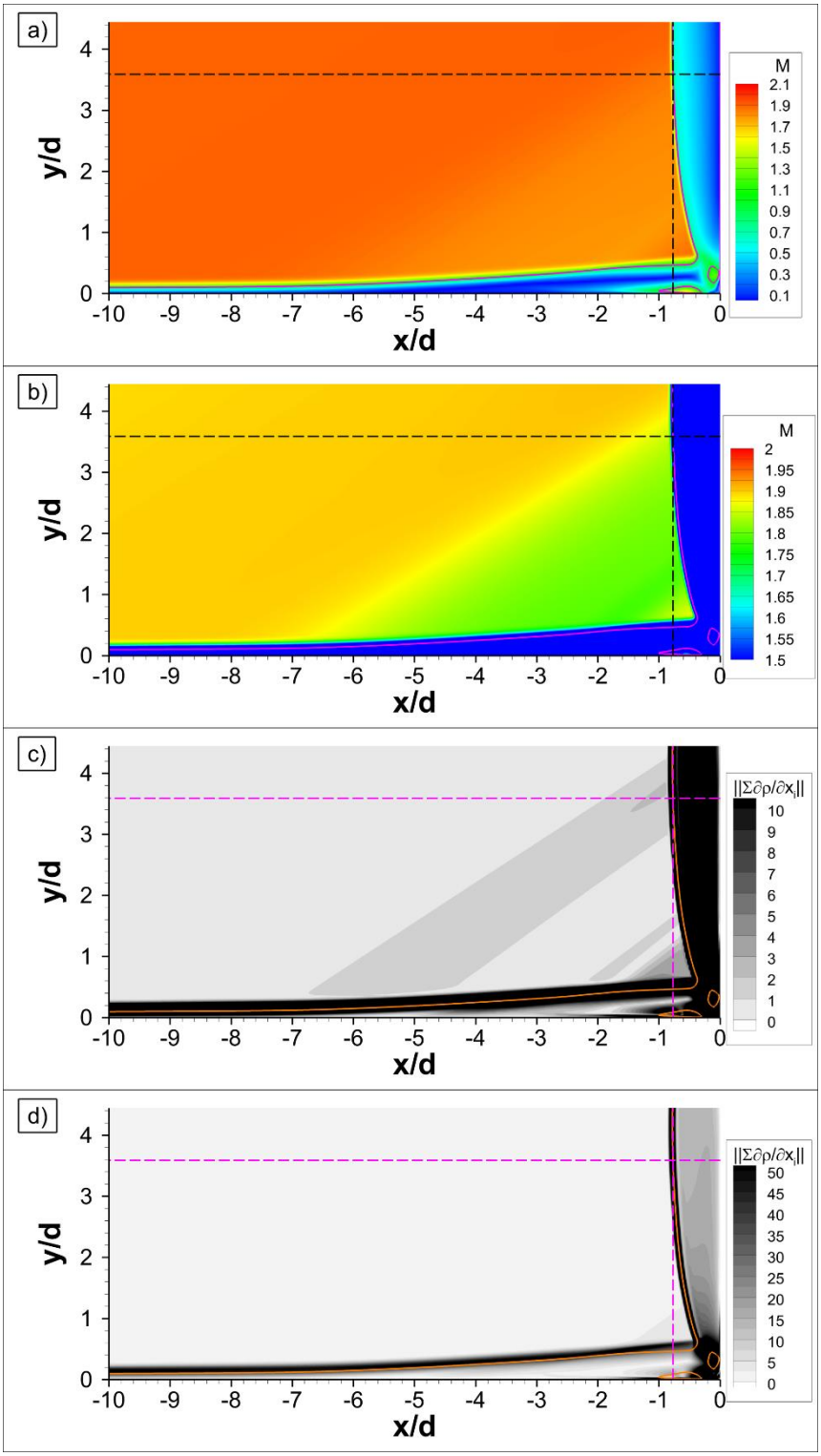


Figure 4.25. a) - b) Mach number contours where pink line represents sonic line, black lines represent empirical values for B and h_{tp}. c) - d) numerical Schlieren contours where orange line is sonic line and pink lines represent empirical values for B and h_{tp}. Reduced contour levels for b) and c).

At this point, it should be verified that the interaction was in fact laminar, considering that a turbulence model was used to simulate the flow; this was necessary to generate a converged solution. The ratio of turbulent-to-laminar viscosity is thus shown in Figure 4.26 for the region of interest, where the orange solid line represents a ratio of unity. The only space where turbulence was dominant was in the near-corner region. Throughout most of the remainder of the domain, the turbulent-to-laminar viscosity ratio was around 10^{-6}, except downstream of the bow shock, where it was around 10^{-4}. This verifies that the majority of the interaction (and freestream) space was in a laminar state, and that turbulence only began to affect the flow in the near-corner region.

A quantitative summary of the extra fine mesh results is visually shown through the grid independence study in Figure 4.23a-c and numerically in Table 4.3. Because there was no concrete empirical value for λ/d or h_{tp}/d in the literature, these were kept in parentheses for reference. Note again that the value of λ/d = 5.75 was selected as the median of the expected range. The CFD values were either within the anticipated range or within 5% of the empirical values, and thus indicated a good quantitative agreement as well.

The streamlines in the centerline plane were analyzed to provide further insight into the flow structure. As with the turbulent interaction cases, only *u* and *v* were used in the

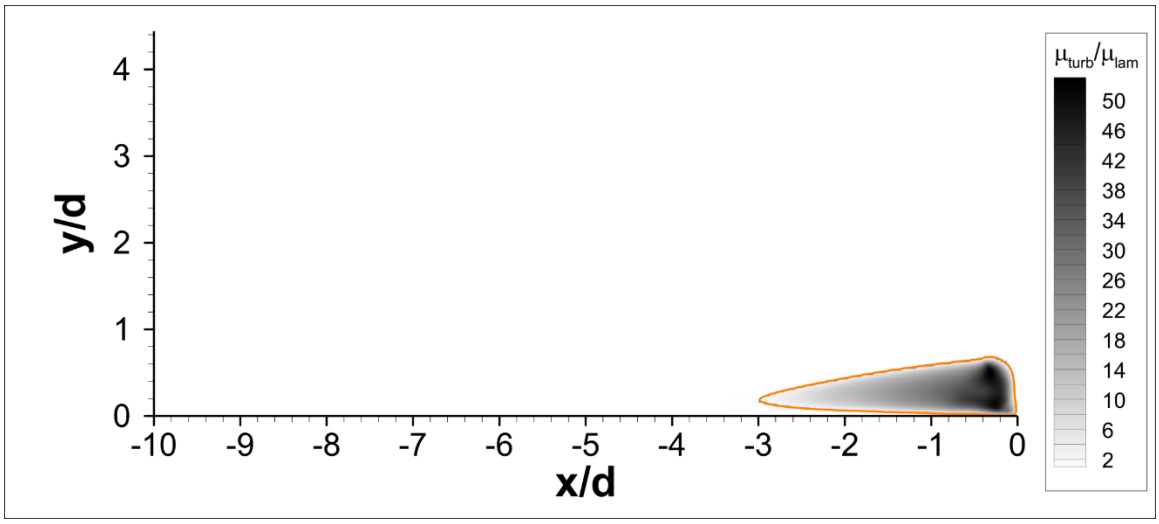


Figure 4.26. Turbulent-to-laminar viscosity for laminar interaction. Orange solid line is a ratio of unity.

Table 4.3. Comparison of parameters of interest between empirical values [11, 24] and extra fine mesh results for laminar interaction.

	Empirical Value	**CFD Value**	**|Relative Difference|**
$\boldsymbol{\lambda/d}$	(5.75)	5.69	(1.0%)
$\boldsymbol{B/d}$	0.77	0.78	1.3%
$\boldsymbol{h_{tp}/d}$	(3.59)	3.47	(3.3%)

analysis. The streamlines are shown in Figure 4.27a and b. The vortex structures show very primary vortex is visible in the separation bubble, and the smaller secondary and tertiary vortices are located in the near-corner region. The plateau of the separation bubble similar characteristics to those found in a turbulent interaction [8, 16], where a single, large, occurred at a similar height of $y/d = 0.6$ when compared to the turbulent interaction. At this location, just upstream of the trailing shock foot, a Prandtl-Meyer expansion fan was located, which turned the flow tangential to the flat plate surface.

A more detailed examination of the streamlines in the corner region was performed and is shown in Figure 4.28. This was done to assess the locations of the separation and attachment lines, and possibly determine peak and trough pressure locations. Again, the Mach number contours in Figure 4.28a were altered to view the subsonic portion of the flow, and it can be seen that the flow remained entirely subsonic in this portion of the domain. As with the laminar interaction characterization from Figure 2.7 and the turbulent interaction characterization from Figure 4.22, the flow separation and attachment lines corresponding to *SL1* and *AL1* of Figure 4.22 were visible in Figure 4.27a and b for the primary vortex, and *SL2* and *AL2* were visible in Figure 4.27a and b and Figure 4.28a and b, respectively. Compared to the SA-QCR turbulent interaction results with the cylinder of height $y/d = 10$, *SL1* for the laminar interaction increased by roughly a factor of 2, *AL1* shifted upstream from $y/d = 1.5$ to $y/d = 2.3$, and *SL2* shifted upstream from $x/d = -0.1$ to $x/d = -0.15$. Surprisingly, however, *AL2* remained nearly constant, with a small shift downwards from $y/d = 0.21$ for the turbulent interaction to $y/d = 0.20$ for the laminar interaction.

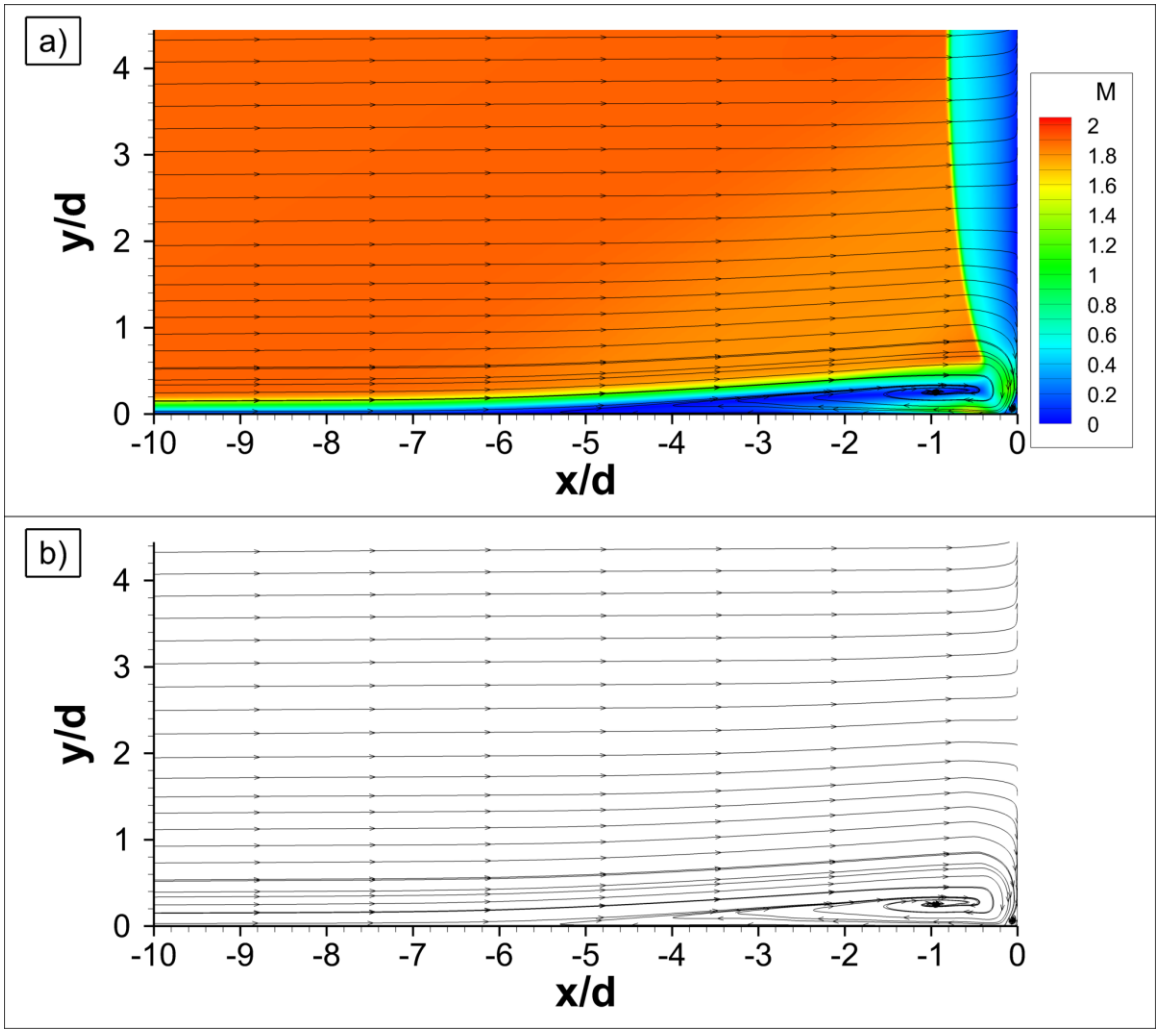


Figure 4.27. Streamlines for laminar interaction, a) with and b) without Mach number contours.

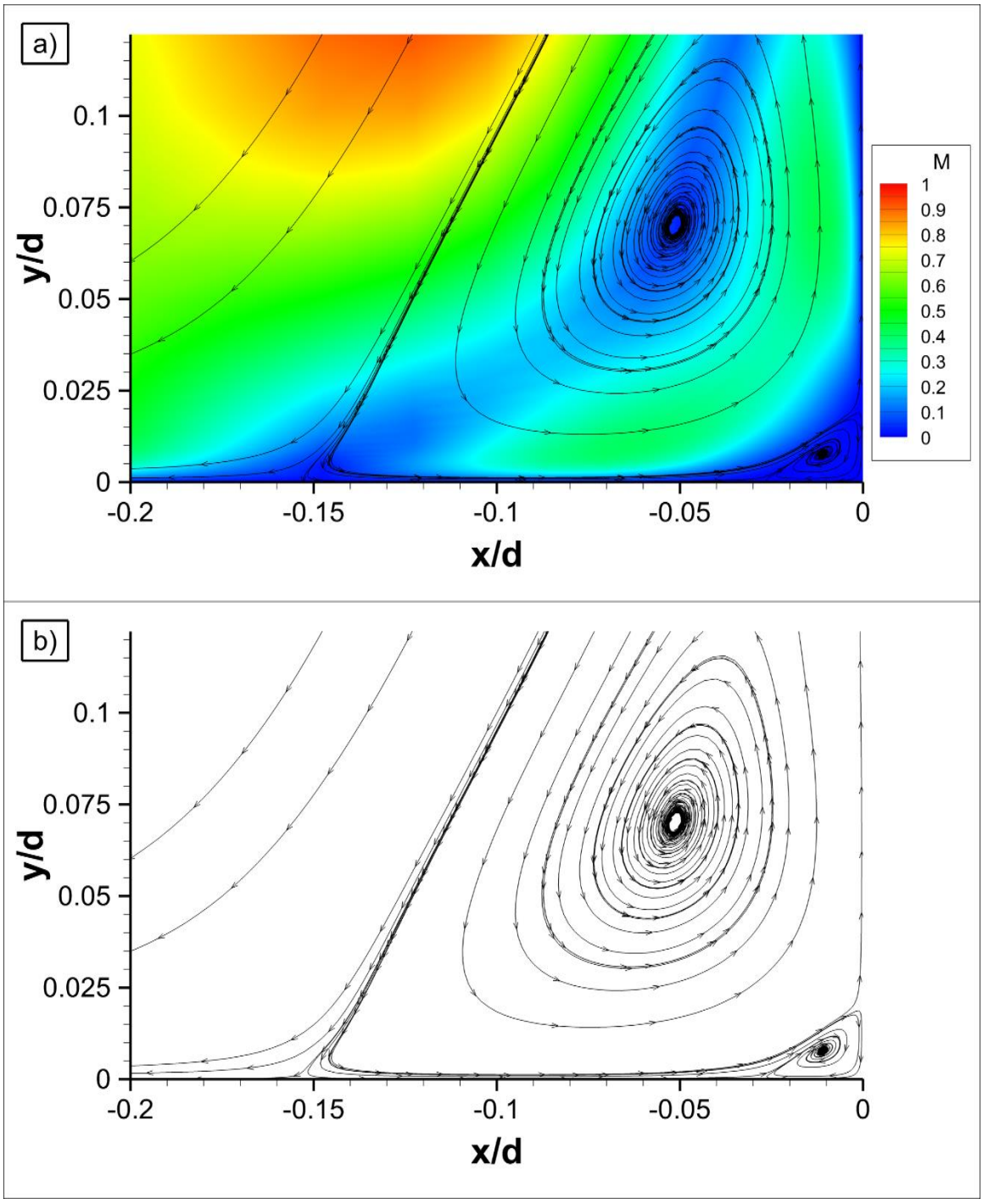


Figure 4.28. Streamlines on zoomed-in corner region for laminar interaction, a) with and b) without Mach number contour.

4.2.3 Surface Pressure Analysis

In order to complete the present analysis of the laminar interaction, the surface pressure upstream of the cylinder was assessed. The normalized pressure ratio on the flat plate surface is shown in Figure 4.29, and exhibited a similar trend as compared to the turbulent interaction. The initial pressure rise occurred at around $x/d = -8$, followed by a very shallow pressure rise that remained below $P/P_\infty < 1.2$. Around $x/d = -2$, the pressure drop occurred, which led to the trough pressure at $x/d = -0.6$; this trough pressure was also at the same location for all turbulent simulations. Note also that the trough pressure was below the freestream pressure around $P/P_\infty \approx 0.9$. The trough pressure was followed by the steep pressure rise, until the peak pressure of around $P/P_\infty \approx 4.6$ occurred at $x/d = -0.16$. This location correlated again with the attachment line *AL2* in Figure 4.22. The peak pressure was slightly lower than the $P/P_\infty \approx 4.8$ for the turbulent interaction. The pressure downstream of the peak pressure was around $P/P_\infty \approx 3.6$, which was similar to the $P/P_\infty \approx 3.8$ for the turbulent interaction with a cylinder of height $y/d = 10$.

The pressure ratio on the cylinder leading edge is shown in Figure 4.30, and had similar trends as for a turbulent interaction. Starting at the base of the cylinder and moving upwards, some initial fluctuations were observed, followed by a decrease that led to the trough pressure of $P/P_{0,2} \approx 0.55$ at $y/d = 0.3$. This was also observed for a turbulent interaction with the SA-QCR turbulence model and a cylinder of height $y/d = 10$, which yielded $P/P_{0,2} \approx 0.5$ at the same location of $y/d = 0.3$. The pressure rise for the laminar interaction remained below $P/P_{0,2} < 1.1$ with a peak pressure of $P/P_{0,2} \approx 1.07$ around $y/d \approx 1.4$, followed by a gradual decrease to the inviscid bow shock region with $y/d > 4.6$, where $P/P_{0,2} = 1$. This last trend was inverted when compared to the turbulent interaction, where a steep pressure rise from the trough pressure occurred, followed by a shallower rise after crossing $P/P_{0,2} = 1$, until the peak pressure value occurred in the vicinity of the triple point. This was then followed by a steeper decrease to the inviscid value of $P/P_{0,2} = 1$ in the turbulent interaction. No correlation was found when trying to determine what caused this discrepancy, or what the reason for the lower location of the peak pressure was in the laminar interaction, but it is suspected that the weaker interaction caused this.

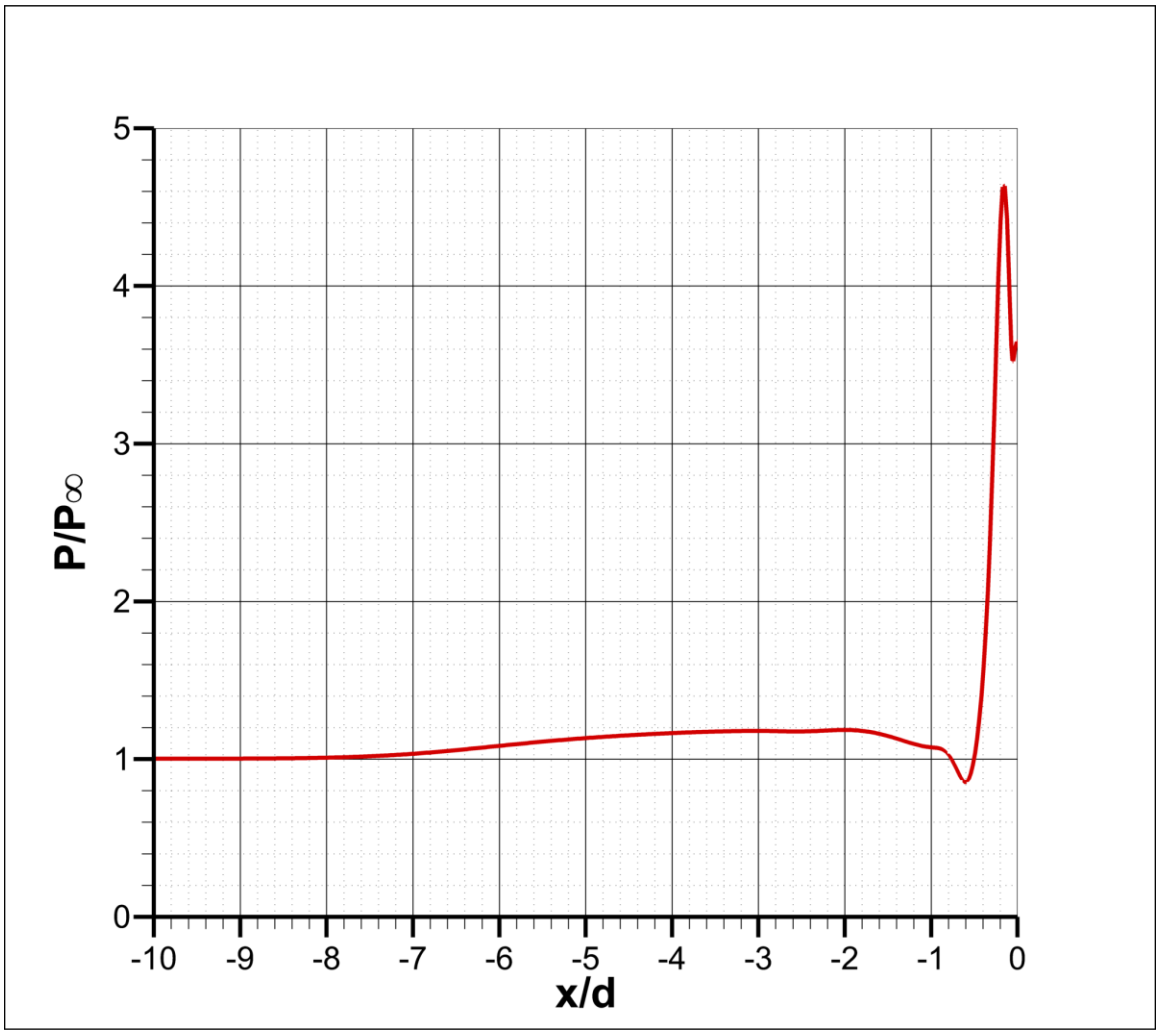


Figure 4.29. Normalized pressure ratio on the flat plate surface for laminar interaction.

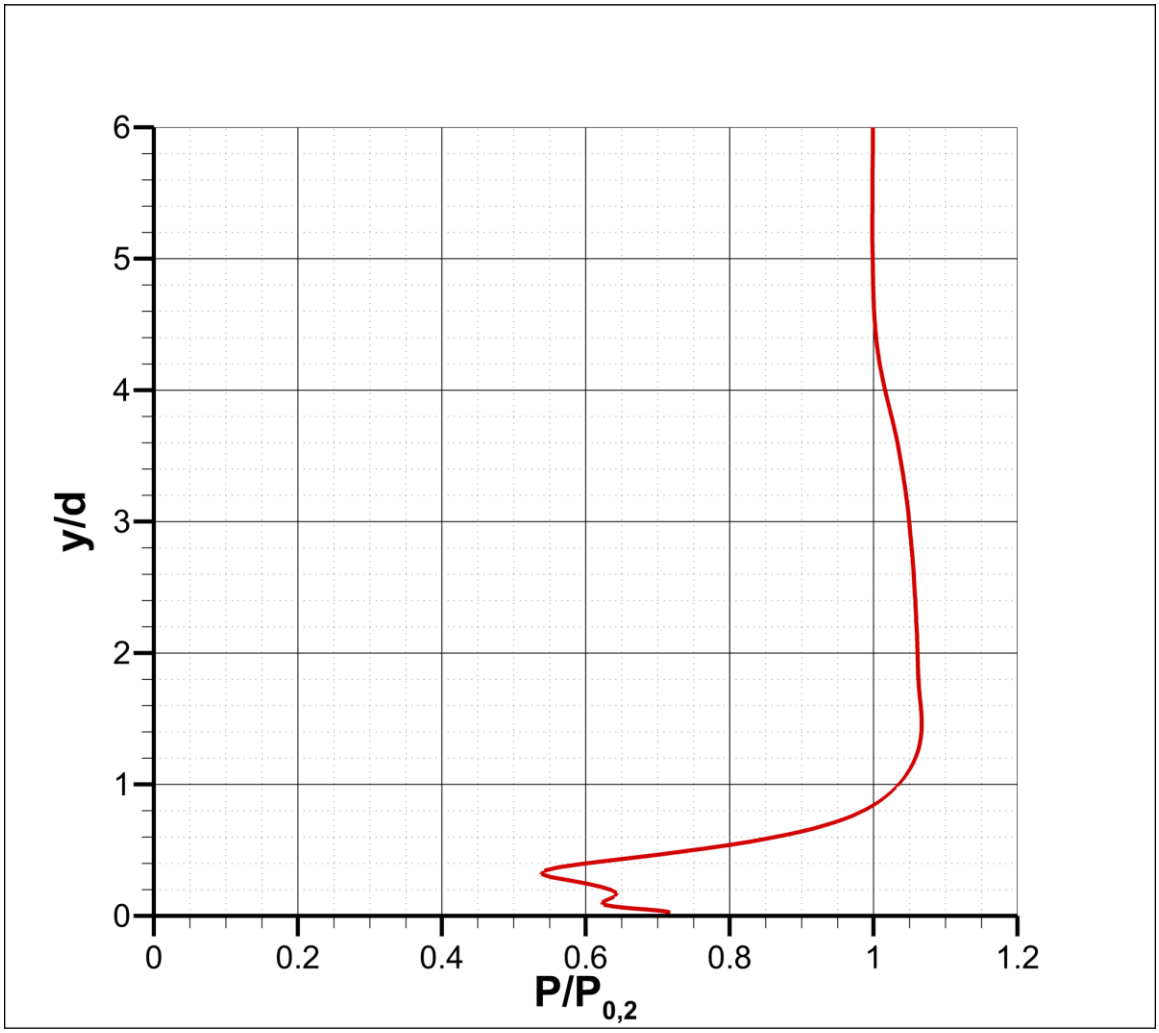


Figure 4.30. Normalized pressure on the leading edge of the cylinder for laminar interaction

Lastly, Figure 4.31a and b shows the skin friction coefficient, multiplied by 1000, and the normalized pressure ratio on the flat plate surface, respectively. Similar to the turbulent interaction, the contour levels were cut off below $C_f = 0.001$ and above $C_f = 0.02$, as well as below $P/P_\infty = 0.6$ and above $P/P_\infty = 2$, in order to provide clarity in the figures. The initial disturbance can be seen in Figure 4.31a around $x/d = -9$, but this is not visible in the pressure contour of Figure 4.31b due to the gradual pressure rise. The upstream pressure plateau can be seen in Figure 4.31b where $P/P_\infty < 1.2$. An area of low $C_f \approx 0.004$ was observed around $x/d = -0.16$, coinciding with the peak pressure. However, the lowest C_f in the upstream region was still near the leading edge where the tertiary vortex was formed. At this location, $C_f \approx 0.0003$. Since the laminar interaction has greater length-scales associated with it compared to a turbulent interaction, the outboard extent was also expected to be greater. It can be seen in Figure 4.31a and b that the bulk of the interaction was within $z/d = \pm 3$. The effects that were further outboard than this were relatively weak in magnitude. This further indicates that the interaction behaves in a closed sense at the centerline, and in an open sense away from the centerline, since the horseshoe vortices sweep outboard and continuously decrease the strength and scale of the interaction.

4.2.4 SWLBLI Topology Characterization with RANS

The streamlines for the laminar interaction in Figure 4.27 were similar in both trend and behavior to those of the turbulent interactions in Figure 4.3 and Figure 4.13. Therefore, the method of Hunt et al. [49] was employed again to generate a topological model similar to that of Figure 4.22, and is shown in Figure 4.32 As required, the 2 nodes subtracted by the 4 half-saddles yielded 0, since each node was again associated with 1 separation line and 1 attachment line. Similar correlations exist as for the turbulent interaction: *SL1* corresponds to λ, *AL2* corresponds to the peak pressure location on the flat plate surface, and *SL2* is loosely correlated to the trough pressure on the cylinder leading edge, although *SL2* was again located downwards of the trough pressure on the cylinder leading edge. A correlation between *AL1* and other parameters was not found. Note, though, that *AL1* was much lower than h_{tp}. This topological characterization does not agree with the experimental

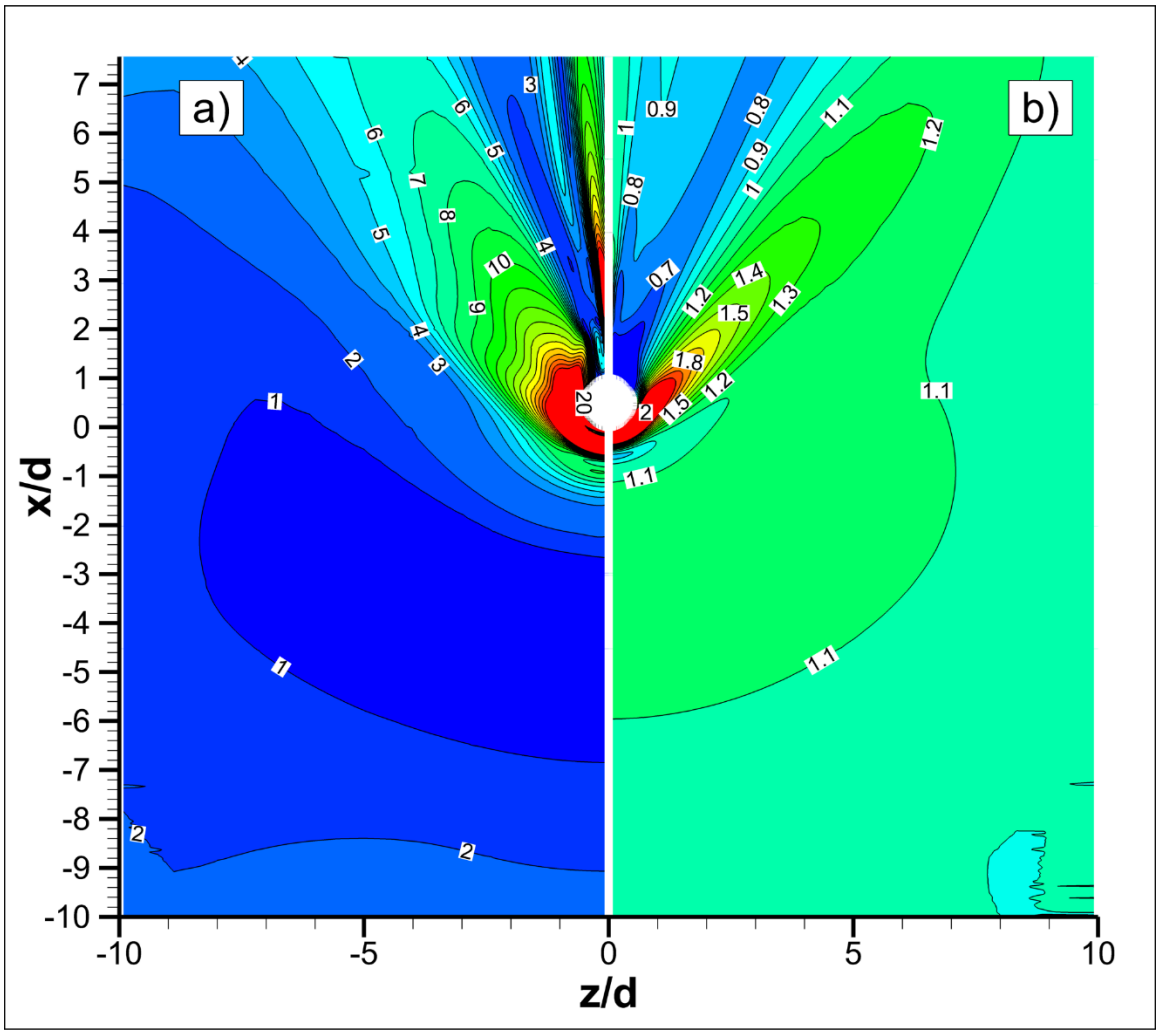


Figure 4.31. a) Skin friction coefficient × 10^3 and b) normalized surface pressure ratio lines and contours at y/d = 0 for laminar interaction. Flow from bottom to top.

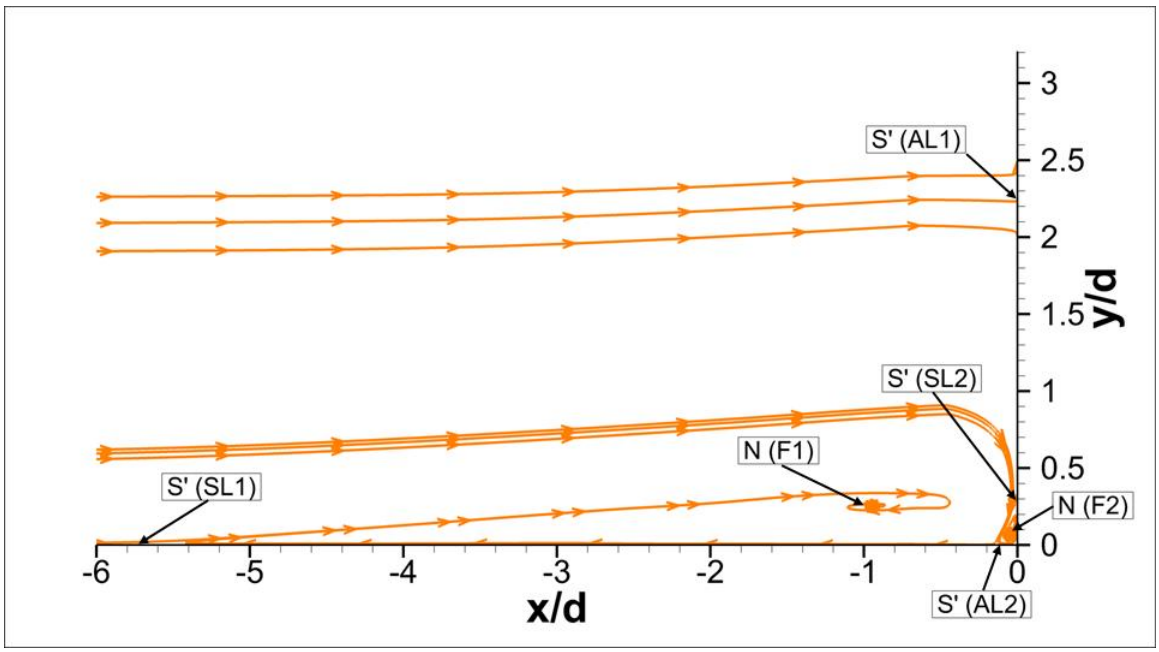


Figure 4.32. Topological model of SWLBLI using streamlines at z/d = 0 for SA-QCR turbulence model with laminar inputs.

characterization obtained by Itoh and Mizoguchi [25], because, as seen in Figure 2.7, Itoh and Mizoguchi [25] derived 4 nodes with 2 larger counter-rotating vortices in the separation bubble, as opposed to 1 primary vortex. Based on the similar discrepancy that arose for a turbulent interaction, it must be noted that this characterization is thus also only valid for steady-state RANS simulations of a semi-infinite-cylinder-induced SWLBLI. As with the turbulent interaction, the dimensions and scales of the laminar interactions will vary depending on the choice of turbulence model and flow conditions, and dimensions were provided simply for reference.

CHAPTER 5
CONCLUSIONS

To establish the bounds of a cylinder-induced shock wave/boundary layer interaction in a transitional boundary layer, a numerical study was performed of the limiting laminar and turbulent cases at M_∞ = 1.88. In the process, a goal was to provide a better understanding of the laminar and turbulent interactions. The parameters of interest were the separation length, λ, the bow shock stand-off distance, B, and the lambda shock triple point height, h_{tp}. Steady-state RANS simulations were carried out to analyze the limiting states of the flow, although these interactions are known to be inherently unsteady.

For the turbulent interaction, two cylinder heights were simulated; both were considered "semi-infinite" based on correlations from prior reported experimental data. Initially, convergence issues led to the selection of a taller cylinder, but these were mitigated by decreasing the time-step temporal smoothing factor (under-relaxation) from 0.75 to 0.5 and activating time-step spatial smoothing in the solver. A comparison was made with in-house experiments and literature regarding the shock structures, parameters of interest (as noted above), and surface pressures. Furthermore, three turbulence models, namely Menter's shear-stress transport (SST), the Spalart-Allmaras (SA) with quadratic constitutive relations (QCR), collectively SA-QCR, and the cubic k-ε (CKE) were evaluated. It was determined that the CKE and SA-QCR turbulence model results aligned within 10% of reported empirical data and thus indicated good agreement, but the SST turbulence model over-predicted separation, and the difference exceeded 15% from empirical values.

For the laminar interaction, the SA-QCR turbulence model was used after imposing a Blasius laminar boundary layer profile as an inflow boundary condition, and it was verified that this generated laminar flow throughout the vast majority of the domain and the interaction. A comparison with the parameters of interest reported in literature yielded agreement within 5%.

By analyzing the vortex structures for both the laminar and turbulent interactions, it was determined that steady-state RANS results only produced one large, primary vortex

upstream of the cylinder. For turbulent interactions, Hung and Buning [16] achieved a similar result with steady-state computational results, but Yamamoto and Takasu [15] found a pair of counter-rotating primary vortices in their unsteady numerical work. Sedney and Kitchens [20] experimentally observed variations in the number of primary vortices, such that the single primary vortex remains a valid solution, in addition to being a numerical steady-state artifact.

Combining the vortex structure analyses with pressure data on the flat plate surface and cylinder leading edge yielded an identification of the peak pressure location on the flat plate surface and a loose correlation of the trough pressure location on the cylinder leading edge. The two locations corresponded to attachment and separation lines, respectively, of the secondary vortex in the near-corner region. A topological model was established for both the laminar and turbulent interactions describing the nodes and half-saddles in the flow, and how the half-saddles correlated to the flow phenomena. Although this analysis characterized the flow for a laminar and turbulent interaction, it should be noted that it is only valid in cases where a single, large, primary vortex occurs. Future work should focus on generating a characterization with unsteady numerical methods, and identifying if the number of vortices can be controlled, and what their impact is on the dynamic flow field.

A study analyzing the effect of the incoming boundary layer height on the scale of the interaction was performed for the turbulent case. By keeping all values constant and only varying δ/d, this was a simply change to the boundary conditions. It was found that as δ was increased, so was h_{tp} and the height of the separation bubble. This allowed for less shear to occur on the flat plate surface and cylinder leading edge, thus reducing the peak pressure magnitude. As δ was increased beyond $\delta/d \geq 1$, λ remained constant despite the initial pressure rise shifting upstream, suggesting that the forward shock foot curved significantly. Furthermore, the trailing shock curved more with increased δ, such that the horizontal extent of the lambda shock continuously decreased. Based on these effects, future work should study the effects of δ/h_{tp} in order to reduce the peak pressures of the interaction.

Lastly, the extent of the laminar and turbulent interactions at the given flow conditions was established. The upstream streamwise extent should be within λ/d = 2.2-6.8,

considering a 20% safety margin, and the spanwise extent should be within $z/d = \pm(4\text{-}8.4)$, considering the same 20% safety margin. The bow shock stand-off distance was calculated consistently for both the laminar and turbulent interaction, and was found to be within $B/d = 0.7\text{-}0.92$, considering a 10% safety margin. These limits will guide on-going and future in-house experiments concerning a transitional interaction, including the design of experimental models, and the selection and location of instrumentation.

LIST OF REFERENCES

[1] Holden, H. A., and Babinsky, H., "Separated Shock-Boundary Layer Interaction Control Using Streamwise Slots," *Journal of Aircraft*, Vol. 42, No. 1, Feb. 2005, pp. 166-171.

[2] Bisek, N. J., "High-Fidelity Simulations of the HIFire-6 Flow Path," AIAA Paper 2016-1115, Jan. 2016.

[3] Gaitonde, D. V., "Progress in Shock Wave/Boundary Layer Interactions," *Progress in Aerospace Sciences*, Vol. 72, 2015, pp. 80-99.

[4] Dolling, D. S., "Fifty Years of Shock-Wave/Boundary-Layer Interaction Research: What Next?," *AIAA Journal*, Vol. 39, No. 8, Aug. 2001, pp. 1517-1531.

[5] Knight, D. D., and Degrez, G., "Shock Wave Boundary Layer Interactions in High Mach Number Flows. A Critical Survey of Current Numerical Prediction Capabilities," Advisory Report 319, AGARD, Vol. 2, Dec. 1998, pp. 1.1-1.35.

[6] Lash, E. L., Combs, C. S., Kreth, P. A., Beckman, E. A., and Schmisseur, J. D. "Developing an Image-Based Analysis of the Dynamics of Transitional Shock Wave-Boundary Layer Interactions," AIAA Paper 2016-4320, Jun. 2016.

[7] Combs, C. S., Lash, E. L., and Schmisseur, J. D., "Investigation of a Cylinder-Induced Transitional Shock Wave-Boundary Layer Interaction using Laser Diagnostics," AIAA Paper 2016-4321, Jun. 2016.

[8] Kaufmann, L. G., II, Korkegi, R. H., and Morton, L. C., "Shock Impingement Caused by Boundary Layer Separation Ahead of Blunt Fins," ARL 72-0118, Aug. 1972.

[9] Settles, G. S., and Dodson, L. J., "Hypersonic Shock/Boundary-Layer Interaction Database," *AIAA Journal*, Vol. 32, No. 7, Jul. 1994, pp. 1377-1383.

[10] Clemens, N. T., and Narayanaswamy, V., "Low-Frequency Unsteadiness of Shock Wave/Boundary Layer Interactions," *Annual Review of Fluid Mechanics*, Vol. 46, Jan. 2014, pp. 469-492.

[11] Westkaemper, J. C., "Turbulent Boundary-Layer Separation ahead of Cylinders," *AIAA Journal*, Vol. 6, No. 7, Jul. 1968, pp. 1352-1355.

[12] Dolling, D. S., and Bogdonoff, S. M., "Scaling of Interactions of Cylinders with Supersonic Turbulent Boundary Layers," *AIAA Journal*, Vol. 19, No. 5, May. 1981, pp. 655-657.

[13] Brusniak, L., and Dolling, D. S., "Physics of Unsteady Blunt-Fin-Induced Shock Wave/Turbulent Boundary Layer Interactions," *Journal of Fluid Mechanics*, Vol. 273, Aug. 1994, pp. 375-409.

[14] Özcan, O., and Yüceil, B. K., "Cylinder-Induced Shock-Wave Boundary-Layer Interaction," *AIAA Journal*, Vol. 30, No. 4, Apr. 1992, pp. 1130-1132.

[15] Yamamoto, S., and Takasu, N., "Numerical Study of Unsteady Shock/Boundary-Layer Interaction Induced by a Blunt Fin," AIAA Paper 1998-2815, Jun. 1998.

[16] Hung, C. M., and Buning, P. G., "Simulation of Blunt-Fin-Induced Shock-Wave and Turbulent Boundary-Layer Interaction," *Journal of Fluid Mechanics*, Vol. 154, Mar. 1985, pp. 163-185.

[17] Truitt, R. W., "Hypersonic Turbulent Boundary-Layer Interference Heat Transfer in Vicinity of Protuberances," *AIAA Journal*, Vol. 3, No. 9, Sep. 1965, pp. 1754-1755.

[18] Anderson, J. D., Jr., "Modern Compressible Flow: with Historical Perspective," 3rd ed., McGraw-Hill, 2003.

[19] Dolling, D. S., and Bogdonoff, S. M., "Blunt Fin-Induced Shock Wave/Turbulent Boundary Layer Interaction," *AIAA Journal*, Vol. 20, No. 12, Dec. 1982, pp. 1674-1680.

[20] Sedney, R., and Kitchens, C. W., Jr., "The Structure of Three-Dimensional Separated Flows in Obstacle-Boundary Layer Interactions," BRL-R-1791, Jun. 1975.

[21] Dolling, D. S., and Brusniak, L., "Separation Shock Motion in Fin, Cylinder, and Compression Ramp-Induced Turbulent Interactions," *AIAA Journal*, Vol. 27, No. 6, Jun. 1989, pp. 734-742.

[22] Korkegi, R. H., "Survey of Viscous Interactions Associated with High Mach Number Flight," *AIAA Journal*, Vol. 9, No. 5, May 1971, pp. 771-784.

[23] Murphree, Z. R., "Physics of Unsteady Cylinder-Induced Transitional Shock Wave Boundary Layer Interactions," Ph.D. Dissertation, The University of Texas at Austin, 2009.

[24] Leidy, A. N., Neel, I. T., Bowersox, R. D. W., and Schmisseur, J. D., "Influence of Perturbations on 3-D Hypersonic Shock / Laminar Boundary Interactions," AIAA Paper 2017-1685, Jan 2017.

[25] Itoh, H., and Mizoguchi, M., "Experiments on Unsteadiness Associated with Cylinder-Induced Shock-Laminar Boundary Layer Interaction in Hypersonic Flow," AIAA Paper 2016-3648, Jun. 2016.

[26] Mortazavi, M., and Knight, D., "Shock Wave Laminar Boundary Layer Interaction at a Hypersonic Flow Over a Blunt Fin-Plate Junction," AIAA Paper 2017-0536, Jan. 2017.

[27] Lash, E. L., Combs, C. S., Kreth, P. A., and Schmisseur, J. D., "Experimental Investigation of a Cylinder-Induced Transitional Shock-Wave Boundary Layer Interaction," AIAA Paper 2017-0760.

[28] Holden, M., S., "Historical Review of Experimental Studies and Prediction Methods to Describe Laminar and Turbulent Shock Wave/Boundary Layer Interactions in Hypersonic Flows," AIAA Paper 2016-0494, Jan. 2006.

[29] Murphree, Z. R., Jagodzinski, J., Hood, E. S., Jr., Clemens, N. T., and Dolling, D. S., "Experimental Studies of Transitional Boundary Layer Shock Wave Interactions," AIAA Paper 2016-0326, Jan. 2006.

[30] Anderson, J. D., Jr., "Fundamentals of Aerodynamics," 5th ed., McGraw-Hill, 2010.

[31] Schlichting, H., "Boundary Layer Theory," 4th ed., McGraw-Hill, 1960.

[32] Deem, R. E., and Murphy, J. S., "Flat Plate Boundary Layer Transition at Hypersonic Speeds," AIAA Paper 65-128, Jan. 1965.

[33] Metacomp Technologies, Inc., "CFD++ User Manual," Aguora Hills, CA, 2013.

[34] Menter, F. R., "Two-Equation Eddy-Viscosity Turbulence Model for Engineering Applications," *AIAA Journal*, Vol. 32, No. 8, Aug. 1994, pp. 1598-1605.

[35] Spalart, P. R., and Allmaras, S. R., "A One-Equation Turbulence Model for Aerodynamic Flows," AIAA Paper 92-0439, Jan. 1992.

[36] Mani, M., Babcock, D. A., Winkler, C. M., and Spalart, P. R., "Predictions of a Supersonic Turbulent Flow in a Square Duct," AIAA Paper 2013-0860, Jan. 2013.

[37] Palaniswamy, S., Goldberg, U., Peroomian, O., and Chakravarthy, S., "Predictions of Axial and Transverse Injection into Supersonic Flow," *Flow, Turbulence and Combustion*, Vol. 66, Is. 1, Jan. 2001, pp. 37-55.

[38] Versteeg, H. K., and Malalasekera, W., "An Introduction to Computational Fluid Dynamics: The Finite Volume Method," 2nd ed., Pearson, 2007.

[39] Dobeš, J., Fořt, J., and Příhoda, J., "Implementation of an Algebraic Bypass Transition Model into Two-Equation Turbulence Model for a Finite Volume Method Solver," *Colloquium Fluid Dynamics 2007*, Institute of Thermomechanics AS CR, v. v. i., Prague, Oct. 2007.

[40] Chaudhry, R. S., Subbareddy, P. K., Nompelis, I., Candler, G. V., "Direct Numerical Simulation of Roughness-Induced Transition in the VKI Mach 6 Tunnel," AIAA Paper 2015-0274, Jan. 2015.

[41] Musker, A. J., "Explicit Expression for the Smooth Wall Velocity Distribution in a Turbulent Boundary Layer," *AIAA Journal*, Vol. 17, No. 6, Jun. 1979, pp. 655-657.

[42] Blasius, H., "Grenzschichten in Flüssigkeiten mit kleiner Reibung," *Zeitschrift für Mathematik und Physik*, Band 56, Heft 1, 1908.

[43] Friedlander, D. J., Georgiadis, N. J., Turner, M. G., and Orkwis, P. D., "Numerical Simulations of the University of Michigan Shock Boundary-Layer Interaction Experiments," *AIAA Journal*, Vol. 53, No. 5, May. 2015, pp. 1134-1145.

[44] Vieira, R. F., and Azevedo, J. L. F., "RANS Simulations of Flows with Shock Wave-Boundary Layer Interaction," AIAA Paper 2013-0985, Jan. 2013.

[45] Kalitzin, G., Medic, G., and Xia, G., "Improvements to SST Turbulence Model for Free Shear layers, Turbulent Separation and Stagnation Point Anomaly," AIAA Paper 2016-1601, Jan. 2016.

[46] Murphree, Z. R., Yüceil, K. B., Clemens, N. T., and Dolling, D. S., "Experimental Studies of Transitional Boundary Layer Shock Wave Interactions," AIAA Paper 2007-1139, Jan. 2007.

[47] Lindörfer, S. A., Combs, C. S., Kreth, P. A., and Schmisseur, J. D., "Numerical Simulations of a Cylinder-Induced Shock Wave/Boundary Layer Interaction," AIAA Paper 2017-0534.

[48] Shur, M. L., Spalart, P. R., Strelets, M. H., and Travin, A. K., "A Hybrid RANS-LES Approach with Delayed-DES and Wall-Modelled LES Capabilities," *International Journal of Heat and Fluid Flow*, Vol. 29, Sep. 2008, pp. 1638-1649.

[49] Hunt, J. C. R., Abell, C. J., Peterka, J. A., and Woo. H., “Kinematical Studies of the Flows around Free or Surface-Mounted Obstacles; Applying Topology to Flow Visualization,” *Journal of Fluid Mechanics*, Vol. 86, No. 1, pp. 179-200.

VITA

Stefen A. Lindörfer was born in El Paso, TX, to the parents of Dr. med. Hans W. Lindörfer and Maria D. Dellaplain. He was raised in Gütersloh, Germany, where he attended the Evangelisch Stiftisches Gymnasium Gütersloh. During high school, he moved to Plano, TX, where he attended and graduated from Plano East Senior High School. Seeking out a challenging and inspiring field, Stefen went on to study Aeronautical and Astronautical Engineering at Purdue University. After four long years, he obtained his Bachelor of Science degree in May 2014 from Purdue. He accepted a graduate research assistant position at the University of Tennessee Space Institute in Aerospace Engineering, providing computational support to the group of Dr. John D. Schmisseur. After two years of living in the woods, Stefen graduated with his Master of Science degree in May 2017.

Permanent e-mail: s.lindorfer@yahoo.com